TECHNICAL UNIVERSITY OF LIBEREC
FACULTY OF MECHANICAL ENGINEERING
Department of Power Engineering Equipment

DISSERTATION

Experimental and Numerical Investigation of Backward-Facing Step Flow

Pages:	147
Figures:	105
Tables:	7
Appendices:	2

Author:	Ing. David Albrecht
Supervisor:	RNDr. Pavel Jonáš, DrSc.
Study programm:	P2301 Mechanical engineering
Study branch:	3901V003 Applied mechanics
Study direction:	Fluid mechanics and thermodynamics

Liberec 2010

Abstract

Separated flow accompanied with vortex formation occurs in many engineering applications such are: air-conditioning systems, heat-exchangers, inside gas turbines or can occur in flows over automotive vehicles, where it is responsible for drastic losses in aerodynamic performances. The knowledge of this phenomenon is very important during device development, optimalization and improvement of their performance as well as it is of fundamental importance during development and benchmark testing of numerical models of turbulence. Simple test cases are being studied, in order to better understand the processes foregoing to the separation; one of this test cases is represented by a channel with a backward-facing step geometry.

The aim of this work is to contribute to the current knowledge of the flow in channels with backward-facing step geometry, especially to provide deep information about the effect of sidewalls on the flow inside the channel. Four channels with different aspect ratios were build and instaled as a part of experimental framework including the preasure air source, flow regulation and metering instrumentation. The flow inside the channels was investigated by means of Particle Image Velocimetry (PIV) in wide range of Reynolds numbers covering the laminar and the begining of the transitional regime of the flow.

Contemporary to the experimental investiagion, a numerical models of the same geometry were prepared and the flow was simulated by Large Eddy Simulation (LES), which promises increased accuracy compared to the conventional Reynolds averaging (RANS) approach, but much less expensive than Direct Numerical Simulation (DNS). Finaly, the results of the numerical simulation were compared with the experiment.

Keywords: backward-facing step, channel flow, experimental, large eddy simulation, LES, numerical simulation, particle image velocimetry, PIV.

Abstrakt

Odtržení proudění s následným výskytem vírových struktur je běžným jěvem v mnoha technických aplikacích jako například: klimatizace, výměníky, turbíny nebo může nastat u prodění kolem automobilů, kde má vliv na značný pokles aerodynamických vlastností. Znalost tohoto jevu je velmi důležitá při vývoji a optimalizaci zařízení, při zlepšování jejich účinnosti, stejně tak její znalost je nezbitná pri vývoji a benchmarkových testech numerických modelů turbulence. Případy proudění kolem jednoduchých geometrií jsou studováný pro lepší porozumění procesů odtržení; jedním z těchto testovacích případů je proudění v kanále s geometrií zpětného schodu.

Cílem této práce je rozšířit současné poznatky o proudění v kanále s geometrií zpětného schodu, obzvláště rozšírit znalosti týkající se vlivu bočních stěn na proudění uvnitč kanálu. K tomuto účelu byly postaveny čtyři kanály s různým poměrem stran, včetně zdroje tlakového vzduchu, regulace a měření průtoku kanály. Proudění uvnitř kanálů bylo vyšetřováno pomocí Particle Image Velocimetry (PIV) v širokém rozsahu Reynoldsových čísel zahrnujících laminární a přechodový režim proudění.

Současně s experimentálním výzkumem probíhalo numerická simulace proudění metodou Large Eddy Simulation (LES), u které lze předpokládat vyšší přesnost výsledků v porovnání s modely založenými na Reynoldsově průměrování (RANS modely), nicméně mnohem ekonomičtější nez přímá numerická simulace - Direct Numerical Simulation (DNS). Výsledky numerické simulace jsou v konečné fázy porovnány s experimentem.

Klíčová slova: zpětný schod, experiment, large eddy simulation, LES, numerická simulace, particle image velocimetry, PIV.

Acknowledgements

I wish to express my depest gratitude to my supervisor, RNDr. Pavel Jonáš, DrSc., for his guidance, patience, constructive criticism and valuable suggestions that I have been constantly receiving from him. The same I wish to exprest to Assoc. Prof. Pentti Saarenrinne, Ph.D., who gave me increadible support during my intership at Tampere University of Technology.

I would like to thank Assoc. Prof., M.Sc. Jiří Unger, Ph.D., not only for his patience and constructive criticism, but first of all for the funding he was able to find, without which this reasearch wouldn't be realized. My thanks belongs to Prof. Ing. Kopecký Václav, CSc., that he allowed me to utilize equipment of their laboratory, especially the Particle Image Velocimeter.

I would like to tkank Petr Jerje and Jaroslav Kneř, for their technical support, constructive criticism and humor that have been invaluable. Thanks also to my colleagues at Tampere University of Technology, as well as, my colleagues at Technical University of Liberec for many fruitful discussions and support during the course of this thesis. My thanks also go to faculty administrative staff Daniela Stejskalová and Jaroslava Krejčová, as well as, to secretary of our department, Drahomíra Stejskalová, for their patience with my administrative messiness.

This work was supported by Institutional research plan MSM4674788501 - Optimization of machine properties in interaction with working processes and human aspects. The access to the MetaCentrum supercomputing facilities provided under the research intent MSM6383917201 is appreciated.

Finaly, I would like to thank to my parents and my friends for their increadible patience and unfailing support during the research.

David Albrecht

September 2010

Confirmation of Authorship

I hereby confirm that the submitted work is entirely my own and was written only with the help of the referenced literature.

Liberec, 16. September 2010 David Albrecht

…….

Contents

List of Figures

List of Tables

[1]The Reynolds numbers in the first column represent intended Reynolds numbers of particular measurements, see Table 4.1.

[2]The Reynolds numbers in the first columnt represent intended Reynolds numbers of particular measurements, see Table 4.1.

[1]The Reynolds numbers in the first columnt represent intended Reynolds numbers of particular measurements, see Table 4.1.

[3]The Reynolds numbers in the first columnt represent intended Reynolds numbers of particular measurements, see Table 4.1.

List of Frequently Used Symbols

A	$h\,b$	$[m^2]$	cross sectional area
b		$[m]$	channel width
C_{ij}		$[m^2 s^{-2}]$	cross-stress tensor
C_S		[-]	Smagorinsky constant
d_h	$\frac{4\,h\,b}{2(h+b)}$	$[m]$	hydraulic diameter
d_x, d_y		$[m]$	dimensions in the object plane
D_x, D_y		$[m]$	dimensions in the image plane
f		$[Hz]$	frequency
$f^{\#}$		$[-]$	f-number
$G(\mathbf{x}, x, \triangle)$		$[-]$	filter function
h		$[m]$	upstream (inlet, inflow) section height
h		$[J]$	entalpy
H		$[m]$	downstream (exit, outflow) section height
I, I_{tresh}		$[-]$	intensity of recorded on the media, tresh-old intensity
k		$[W\,m^{-1}K^{-1}]$	thermal conductivity
k		$[m^{-1}]$	wave number
K		$[m^2 s^{-2}]$	turbulent kinetic energy
l_x, l_y		$[m]$	length of field of view
L_{ij}		$[kg\,m^{-1}s^{-2}]$	Leonard term/Leonard stress tensor
L_d, L_u		$[m]$	length of the downstream/upstream section
M		$[-]$	magnification
N_f, N		$[-]$	number of obserfations of downstream flow, total number of realizations
N_x, N_y		$[-]$	number of pixels in x/y direction

p		$[Pa]$	pressure
P	$2(h+b)$	$[m]$	wetted perimeter of the cross-section
P_{2D}		$[m^2 s^{-3}]$	turbulence production
q_j		$[W\ s^{-1}]$	heat flux
q^2_{sgs}		$[m^2 s^{-3}]$	kinetic energy of subgrid-scales
$\dot{Q}$		$[m^3\ s^{-1}]$	flow rate
R_{ij}		$[m^2 s^{-2}]$	Reynolds subgrid scale tensor
Re	$\frac{U_b\,\rho\,d_h}{\mu}$	[-]	Reynolds number based on hydraulic diameter
Re_c		[-]	critical Reynolds number
Re_h	$\frac{U_b\,\rho\,h}{\mu}$	[-]	Reynolds number based on heigth of the upstream section
Re_H	$\frac{U_b\,\rho\,H}{\mu}$	[-]	Reynolds number based on heigth of the downstream section
Re_S	$\frac{U_b\,\rho\,S}{\mu}$	[-]	Reynolds number based on heigth of the step
S		$[m]$	step height
S_{ij}, $\mathbf{S}$		$[s^{-1}]$	rate of strain tensor
t		$[s]$	time
T		$[K]$	absolute temperature
T_{ij}		$[m^2 s^{-2}]$	subgrid stress tensor
T_f, T		$[s]$	aditive time of forward flow, total time
Tu		$[\%]$	turbulence intensity
u, v, w, U, V, W		$[m\ s^{-1}]$	velocity components
U_b		$[m\ s^{-1}]$	bulk (mean) velocity
U_0		$[m\ s^{-1}]$	free stream velocity
u_τ	$\sqrt{\frac{\tau_w}{\rho}}$	$[m\ s^{-1}]$	wall friction velocity
$\mathbf{x}$, $\mathbf{x}'$		$[m]$	general spatial coordinate

x, y, z		$[m]$	coordinate components
x_1, x_r		$[m]$	reattachment length
x_4		$[m]$	location of separation point of upper recirculation region
x_5		$[m]$	location of reattachment point of upper recirculation region
y^+	$y\frac{u_\tau}{\nu}$	[-]	wall coordinate

Greek letter symbols

β	[-]	spanwise wavenumber
δ_0	$[m]$	thickness of boundary layer
δ_{ij}	[-]	Kronecker delta
δ_{sw}	$[m]$	distance from the sidewall
ε	$[m^2 s^{-3}]$	dissipation rate
η	$[m]$	Kolmogorov scale
γ_p	[-]	forward flow fraction
$\phi, \overline{\phi}, \phi'$		generic flow variable
$\triangle, \overline{\triangle}, \widetilde{\overline{\triangle}}$	$[m]$	filter width
λ	[m]	wavelength
$\lambda_1, \lambda_2, \lambda_3$	[-]	eigenvalues
λ_c	[-]	spanwise wavelength
μ	$[Pa\ s]$	dynamic viscosity
ν	$[m^2 s^{-1}]$	kinematic viscosity
ν_{sgs}	$[m^2 s^{-1}]$	subgrid-scale viscosity
Ω_{ij}	$[s^{-1}]$	rate of rotation tensor
ρ	$[kg\ m^{-3}]$	density
τ_{ij}	$[Pa]$	stress tensor
τ'_{ij}	$[m^2 s^{-2}]$	subgrid stress tensor

τ_w, τ'_w	$[Pa]$	wall shear streas, fluctulating part of wall shear stress

Used Abbreviations

AR	b/h	aspect ratio
CFL		Courant number
CTA		Constant Temperature Anemometry
DNS		Direct Numerical Simulation
DSR		dynamic spatial range
DVR		dynamic velocity range
ER	H/h	expansion ratio
GPL		General Public License
LDA		Laser Doppler Anemometry
LDV		Laser Doppler Velocimetry
LES		Large Eddy Simulation
PIV		Particle Image Velocimetry
RANS		Reynolds Averaged Navier-Stokes
SGS		Subgrid-scale
SR		sampling rate

Subscripts

1, 2, 3	direction or position indices
b	bulk, mean
i, j, k	spatial or summation index
rms	root of the mean squares
x, y, z	direction indicators
w	wall or wall derived

Superscripts

$+$	wall units
$.'$	fluctuating component
$.^{d}$	deviatoric component
T	transpose

Oversymbols

$-$	filtered
$\wedge$	fourier space
$\sim$	test filter

Chapter 1. Introduction

The phenomenon of separated flow accompanied with vortex formation belongs between fundamental problems of fluid mechanics, since it is of great importance in many engineering applications. Some examples of these applications are sudden changes in channel area; such are in air-conditionning system or heat exchangers, inside gas turbines or can occur in flows over automotive vehicles, where it is responsible for drastic losses in aerodynamic performances. The knowledge of this phenomenon is very important during device development, optimalization and improvement of their performance. Although this phenomena has been stressed in many publications and numerous investigations, a complete understanding of physical origin of the flow separation and vortex formation hasn't been fully elucidated yet.

Channel flow with sudden expansion in one direction, so called backward-facing step geometry, was for decades used as a suitable geometry for study of separated flows. The major reason to use this geometry configuration is the fact, that even though it is very simple, it generates complex flow structure behind the step, since the flow firstly separates at the step edge and continues as a free shear layer localized between bulk flow and primary recirculation flow region up to the impingement on the bottom wall and following with boundary layer relaxation and redevelopment of the flow in the duct of increased section area. Sometimes it is also accompanied with the formation of secondary recirculation flow regions, where separation and reattachment occurs. Together with the similarity with some real flow cases, above mentioned properties predetermine this geometry also as a simple, yet complex flow case for benchmark tests of numerical turbulence models. There has been presented many experimental and theoretical investigations on this topic with stress on a limited number of relevant parameters affecting the flow structure behind the step, such as Reynolds number, expansion ration $ER = H/h$ and aspect ratio $AR = b/S$, where h is the inlet channel height, H the extended channel height after the step of height S and channel width b. Many of these works were dealing with the simplification to purely two-

dimensional flow structure. Lately, it has been shown that this simplification is reasonable only in the case of high aspect ratio channels at the channel symmetry plane but becomes flawed in the vicinity of sidewalls or when the aspect ratio is small enough that these disturbances extend up to the symmetry plane, since in this case the numerical models predict shorter reattachment length than the real case. Recent experimental and theoretical results show complex flow structure that forms adjacent to the sidewalls with recirculation flow region that forms adjacent to top wall and originates from the sidewall. Furthermore, the present investigations provide only particular set of results with respect to the some of the parameters.

The following section tries to make short overview of the recent publications and elucidate flow structure behind the step.

1.1. Recherche

Fundamental contribution to the knowledge of a backward-facing step flow was made by Armaly et al. [5]. They conducted experimental investigation using Laser Doppler Anemometry in channel of expansion ration $ER = 1.9423$, the aspect ration was $AR = 34.61$, in range of Reynolds number $68 < Re < 7775$ (Fig. 1.1). Thanks to this aspect ratio a two-dimensional like flow near the channel symmetry plane was ensured. Based on the analysis of the reattachment length development versus Reynolds number, they described laminar flow regime as smooth increase of reattachment length up to $Re < 1166$. Maximum reattachment length occurs at $Re = 1166$. Transition flow regime in Reynolds number range of $1166 < Re < 6415$ was typical by primary abrupt drop of reattachment length x_1/S followed by stepwise decrease of reattachment length down to minimum that occures around $Re = 5346$ and followed by slight increase of reattachment length x_1/S. In transitional flow regime they revealed additional recirculating flow region downstream of the primary region of separation. Turbulent flow regime was characterised by constant reattachment length with stable value around $x_1/S = 8$. Already in laminar flow regime an existence of recirculation zone was identified adjacent to the upper wall appearing around $Re = 389$ and disappearing around $Re > 6415$. Its appearance was attributed to the adverse pressure gradient effect past the sudden expansion. Transitional regime was typical by

three dimensional character of the flow. The two-dimensional numerical simulation well agree with the experimental results up to Reynolds number $Re = 389$, by higher Reynolds number a discrepancy in the numerical results is observed, showing shorter reattachment length x_1 than in experiments. This is probably result of the loss of two-dimensionality of the flow and origin of recirculation bubble adjacent to the top wall with detachment and reattachment of bulk flow.

Bradshaw and Wong [12] compared they own experiments results with the data of other experimentators (see. [12]) conducted in flows of various geometries, where the bulk flow was forced to separate and reattach. They concluded, that any attempts to correlate properties of the relaxation regions downstream past different obstacles, in order to describe the perturbation in terms of a few parameters are no likely to succeed and that the relaxation of shear layer proceeds very slowly, much slower than was expected. The Clausers parameter G [17] in they experiment did not decrease monotonically, but reached minimum value in the distance of $x/x_r \approx 60$ with subsequent return to equilibrium state. Similar length was necessary to reach equilibrium value of shear friction coefficient. Comparing results of preceding experimentators, they came to conclusion, that 'overwhelming perturbation' caused by the step geometry, whose dimension is much higher than order of boundary layer thickness at the separation point $s/\delta_0 >> 1$, causes less severe disturbance to the relaxing boundary layer than does 'strong perturbation' caused by step geometry, whose dimension is of order of the separating boundary layer $s/\delta_0 \sim O(1)$.

Ötügen [52] focused on the effect of expansion ratio on the reattachment length in a turbulent flow regime of constant Reynolds number $Re_h = 16600$ in channel with constant dimensions of inlet section and variable step height so, that $ER = 1.5; 2$ and 3.13. The reattachment length decreased for larger expansion ratios, however, the variation in the reattachment length was fairly small, about $4,5\%$ of the average reattachment length. They found rapid growth of the turbulence intensity for all three cases of expansion ratio, however, this growth was much more pronounced for the larger expansion ratios. It should be noticed that simultaneously with the change of the expansion ratio also the aspect ratio changed considerably, from value $AR = 31.17$ ensuring fully two dimensional flow

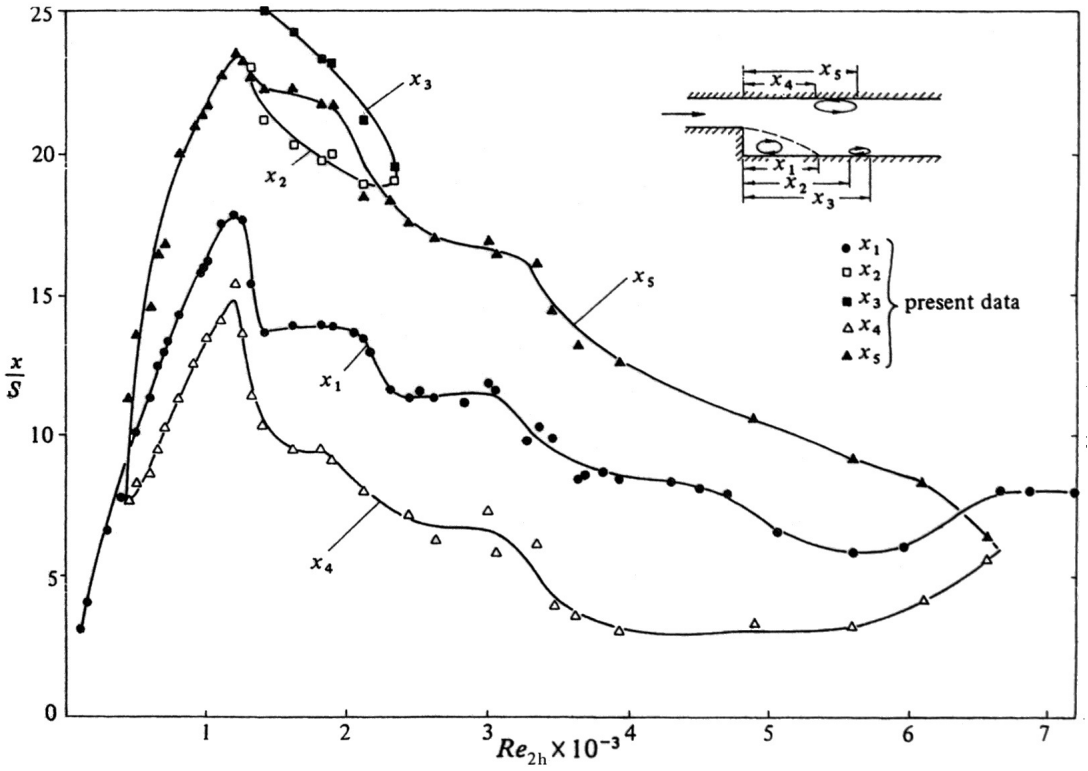

Figure 1.1. Reattachment length, detachment and reattachment length of top recirculation bubble at the symetry plane versus Reynolds number. Experiment: Armaly 1983 - AR = 34.61, ER = 1.9423. Source: Armaly et al. [5].

character adjacent to the symmetry plane in this regime of Reynolds number to the value $AR = 7.36$ for $ER = 3.13$, where the influence of sidewalls begins to be considerable.

Biswas et al. [10] conducted numerical simulation in channel with the expansion ratios $ER = 1.9423; 2.5$ and 3.0 and aspect ratio $AR = 35$. The Reynolds numbers were between $10^{-4} \leq Re \leq 778$. They used as a boundary condition at the inlet parabolic velocity profile for the two-dimensional case and velocity profiles provided by experiments of Armaly et al. [5] for the three-dimensional study. According the set of numerical simulation they confirmed that the length of the inlet part longer than five times the step height $L_u \geq 5\,S$ does no longer influence the results of numerical simulation behind the step and hence this length is sufficient for numerical investigation. They made the conclusion that for Reynolds number around one, a short length of outflow section is sufficient, while in case of higher Reynolds numbers it is necessary to extend the outflow section length up to $L_d = 32\,S$. For very low Reynolds numbers they tried to confirm the existence of a set of Moffat vortices [46] adjacent to the corners. Adjacent to the bottom concave corner

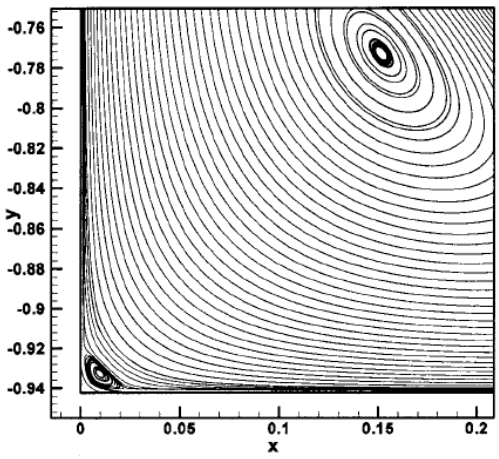

Figure 1.2. Detail of concave conner showing first and second Moffat vortex. Source: Biswas et al. [10].

of $2\alpha = 90°$ that satisfies the Moffat condition, an existence of the set of Moffat vortices was confirmed (Fig. 1.2). According Moffat theory it should be possible to observe infinite set of vortices in the concave corner, but regarding the possible computational resources it was not possible to observe the third and following vortices. Experimental study of the secondary (Moffat) vortex was conducted by Hall et al. [27]. For Reynolds numbers $Re < 1$ there is a vortex of constant size in the concave corner, its size increases with increasing Reynolds number and approximately at $Re = 10$ it reaches the step height and transforms to the recirculation flow region. Their numerical results agree well with experimental data of Armaly et al. [5] up to $Re < 389$ but for higher Reynolds numbers there is remarkable discrepancy between numerical and experimental results, probably because of the commencing three dimensionality. Besides primary recirculation flow region there is also secondary recirculation flow region adjacent to the upper wall that is caused by adverse pressure gradient induced by the sudden expansion at the step edge. They results show that reattachment length x_1/S rises as the expansion ratio increases (Fig. 1.3), what is in a conflict with the experiment by Ötügen [52] and numerical simulations by Kitoh et al. [37]. The reattachment length varies at Reynolds number $Re = 389$ in range $x/s = 7.708$; 10.214 and 12.409 for expansion ratios $ER = 1.9423$; 2.5 and 3.0. At Reynolds number smaller than $Re < 389$ the flow was predominantly two-dimensional, however, as the Reynolds number gets over this value the three-dimensionality effects reveal and a secondary recirculation zone near the upper wall appears. The two dimensional flow behind a backward-facing step becomes unstable with increasing Reynolds numbers. The steady character of the two-dimensional

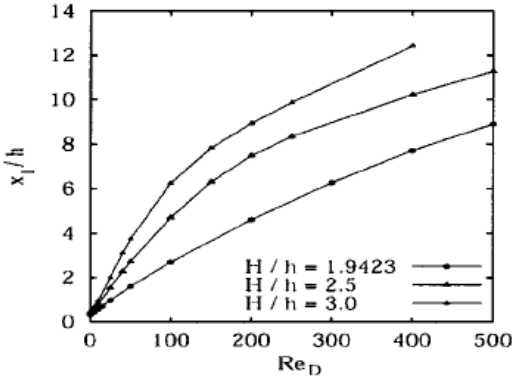

Figure 1.3. Reattachment length of primary recirculation flow region for different expansion ratio $ER = 1.9423$; 2.5 *and* 3.0. Source: Biswas et al. [10].

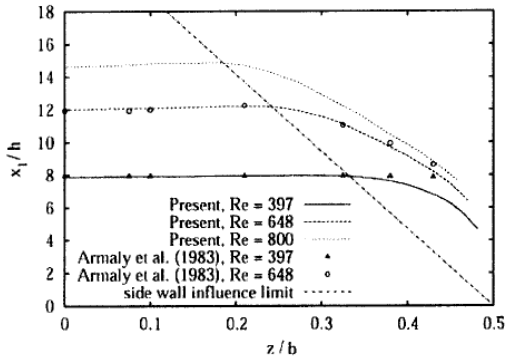

Figure 1.4. Spanwise location of reattachment points for different Reynolds numbers $Re = 386$; 630 and 778, $ER = 1.9423$ and $AR = 35$. The results of numerical simulation of Biswas [10] and experimental data of Armaly [5]. Source: Biswas et al. [10].

backward-facing step flow was revealed over entire Reynolds number range $Re \leq 778$ for an expansion ratio $ER = 1.9423$. On the contrary, for expansion ratio $ER = 3$ they observed instabilities already at a Reynolds number 486. In Fig. 1.4 there is depicted comparison of the numerical simulation results of Biswas et al. [10] and the experimental data of Armaly et al. [5]. At Reynolds numbers $Re = 386$ and 630 there is remarkable good conformity between experimental and numerical data. There are no experimental data for $Re = 778$. (Fig. 1.4) also demonstrates increasing influence of sidewalls as the Reynolds number increases. At $Re = 386$ the influence of sidewalls could be observed up to 36% of the half of channel width $b/2$, while at $Re = 630$ and 778 it is 54% and 66% respectively. This is in good agreement with results of Williamse and Barkera [67] and Chiang and Sheu [16].

Forced convection was simulated by Armaly et al. [6] in the channel of aspect ratio $AR = 8$, expansion ratio $ER = 2$ and heated bottom wall past the step. They conducted simulation for Reynolds number ranging between 100 and 600. They found position of maximum Nusselt number, thereby the maximum heat transfer coefficient, adjacent to the sidewalls downstream to the location where a jet-like flow impinges on the bottom wall. The location of minimum friction coefficient on stepped wall was slightly upstream to the location of maximum Nusselt number. As the Reynolds number increases, the location of

maximum Nusselt number and location of minimum friction coefficient moves further downstream and towards the sidewalls.

Chiang and Sheu [15] and [16] conducted numerical simulation of the flow behind a backward facing step of the same geometry as the experiment of Armaly et al. [5], when the simulated domain was chosen symmetrical to the middle plane. They focused on the influence of sidewalls on the flow development in the channel. They found that the similarity of the velocity profiles at the symmetry plane in three-dimensional simulation domain are getting better compared with the velocity profiles of purely two-dimensional simulation as the width of the channel is increased. In the case with channel width of 100 times the step height the similarity was perfect. They confirmed good compliance between two- and three-dimensional numerical results in a channel with aspect ratio $AR = 35$, except the zone between $10 \leq x/S \leq 20$ and pronounced hypothesis that the influence of sidewalls on the development of primary recirculation flow region $x < 10$ is negligible for channels where width $b > 35h$. On the contrary to the experiments of Armaly et al. [5] they did not observe any existence of secondary recirculation flow region adjacent to the upper wall around the symmetry plane at Reynolds number $Re = 778$ and in channel with aspect ratio $AR = 35$ (see Fig. 1.5), what is supported by numerical results of Williams and Barker [67] and Tylli et al. [65]. But in the channel with aspect ratio $AR = 35$ they observed vortex adjacent to the upper wall only in span wise range $0, 3b \leq z \leq 0.5b$, i.e., adjacent to the sidewalls. However, this vortex spreads across entire span width of the channel as the aspect ratio is over $AR > 50$ and for the case of $AR = 100$ there develops two-dimensional like velocity profile near the symmetry plane. Location of maximum reattachment length $x_1 = x_1(z/S)$ was not found at the symmetry plane, but was found in the xy plane (Fig. 1.5), where the distance between detachment point x_4 and reattachment point x_5 of upper recirculation bubble has its minimum (Fig. 1.6). They found that the character of flow near the symmetry plane at low Reynolds numbers Re < 378 is predominantly two-dimensional (see Fig. 1.7). As the Reynolds number increases, the influence of sidewalls becomes predominant and the two-dimensional like streak near the symmetry plane is getting narrower, what is in agreement with results of Biswas et al. [10]. In the case of higher Reynolds numbers, the effect of three dimensionality indicates increasing discrepancy between two- and three-dimensional simulation, as was already shown in work of Armaly et al. [5].

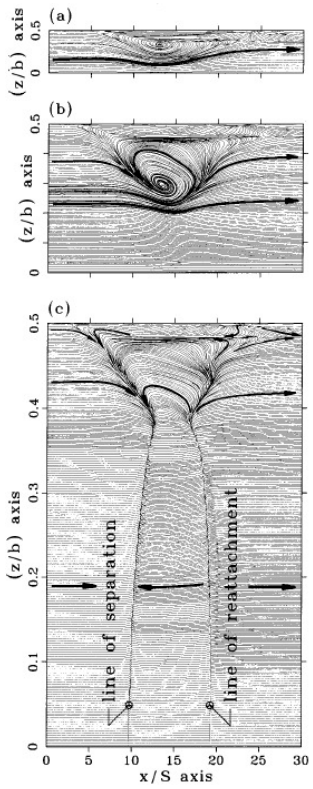

Figure 1.5. Streamlines adjacent to the upper channel wall. a) $AR = 10$ at $Re = 727$, b) $AR = 35$ at $Re = 778$, c) $AR = 100$ at $Re = 792$. Source: Chiang and Sheu [16].

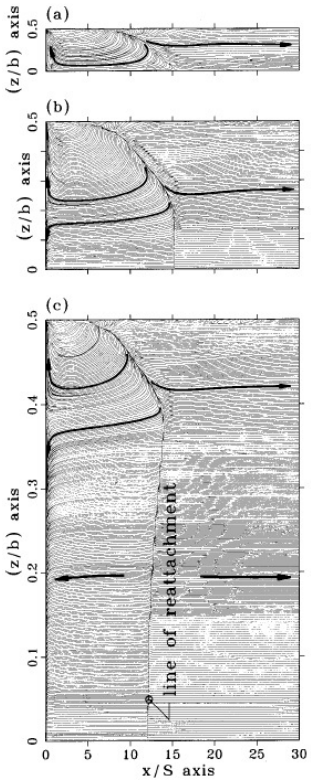

Figure 1.6. Streamlines adjacent to the bottom channel wall. a) $AR = 10$ at $Re = 727$, b) $AR = 35$ at $Re = 778$, c) $AR = 100$ at $Re = 792$. Source: Chiang and Sheu [16].

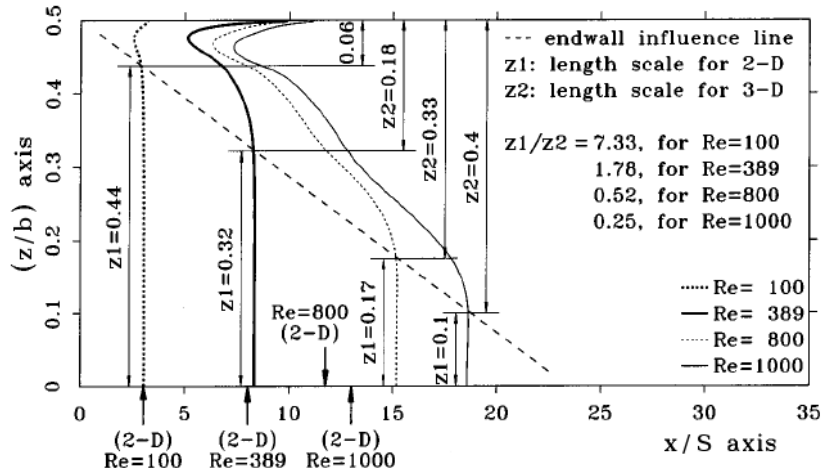

Figure 1.7. Spanwise reattachment profiles at bottom wall in channel of aspect ratio $AR = 35$ at different Reynolds numbers. Source: Chiang and Sheu [16].

Iwai et al. [31] came to similar conclusion, that channel of aspect ratio at least $AR = 16$ is necessary to obtain fully two dimensional flow near the symmetry plane for channel with

expansion ratio $ER = 2$ and t $Re = 471$. In this case the two dimensional recirculation flow region near the symmetry plane spreads over 30% and 50% in channel with aspect ratio $AR = 16$ and $AR = 24$, respectively.

Nie and Armaly [48] performed numerical simulation at constant Reynolds number $Re_H = 343$ (based on the downstream section height) with variable step height. They focused on the influence of heated bottom wall on the flow development behind a backward-facing step. They changed the step height, while the height of the outflow section as well as the channel width was kept constant, thus the expansion ratios were $ER = 1.67;\ 2.00$ and 2.50 and the aspect ratios $AR = 10;\ 8$ and 6.667. They assumed that as the step height increases, the reattachment length elongates and the reverse flow region adjacent to the sidewalls enlarges. This is in direct contrary with the results of DNS simulation conducted by Kitoh et al. [37], what could be probably due to the fact that the Nie and Armaly [48] did not keep constant aspect ratio as Kitoh et al. [37] did. However it is hard to claim this as the rule because the experiment performed by Ötügen [52] shows the same tendency of reattachment length contraction as the numerical simulation by Kitoh et al. [37], who in his work changed the aspect ratio the same way as did Nie and Armaly [48] in their study. They refered the existence of jet-like flow behind a backward-facing step adjacent to the sidewalls (see streamline 3 in Fig. 1.8) and source point (see Fig. 1.9). Streamline 3 in Fig. 1.8 represents the flow path along which a jet-like flow develops in the separating shear layer, impinges on the stepped wall and continues its flow downstream into the developing flow

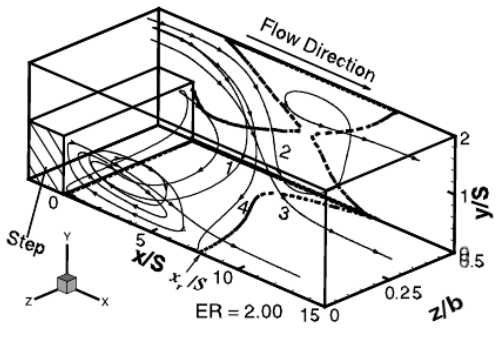

Figure 1.8. Streamlines illustrating the flow character behind a backward-facing step and lines of zero streamwise velocity adjacent to the stepped wall and sidewall. Source: Nie and Armaly [48].

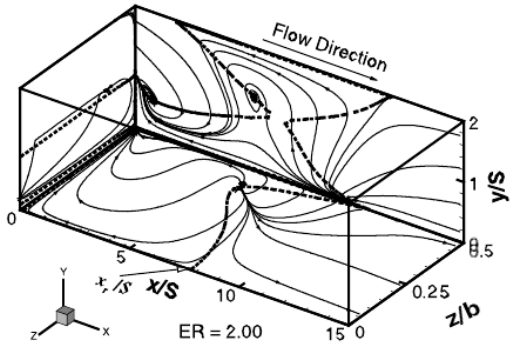

Figure 1.9. Streamlines adjacent to the stepped wall and sidewall and lines of zero streamwise velocity adjacent to stepped wall and sidewall. Source: Nie and Armaly [48].

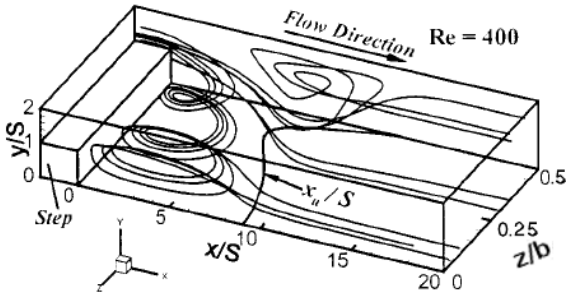

Figure 1.10. Overview on the entire flow behind a backward-facing step. Source: Nie and Armaly [49].

region. This jet-like flow is responsible for the minimum and for the maximum that develop near the sidewall in the spanwise distributions of the primary reattachment length and of the Nusselt number, respectively. As the step height is increased to value higher than 0.008 *m*, a development of a secondary recirculation flow region adjacent to the bottom corner of the step (between the primary recirculation flow region and the step) was detected.

They conducted detailed numerical study of the flow at Reynolds number 400 [49], where they used a symmetry boundary condition at the centerline. According their results, a downwash flow develops adjacent to the sidewalls with a vortex flow and moves in the spanwise direction within the primary recirculating flow region towards the center plane (see Fig. 1.10) and (Fig. 1.11). Fluid originating at the inlet plane of the duct in the region between $0.5 > z/b > 0.485$ follows this spanwise movement inside the primary recirculation flow region (Fig. 1.11). Fraction of the incoming fluid originating in the region between $0,485 > z/b > 0,25$ forms jet-like flow that moves toward the stepped wall and re-

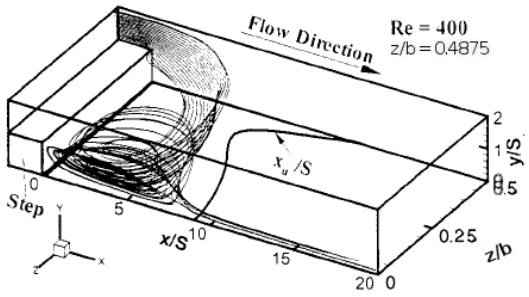

Figure 1.11. Streamlines starting from the spanwise plane of $z/b = 0.4875$. Source: Nie and Armaly [49].

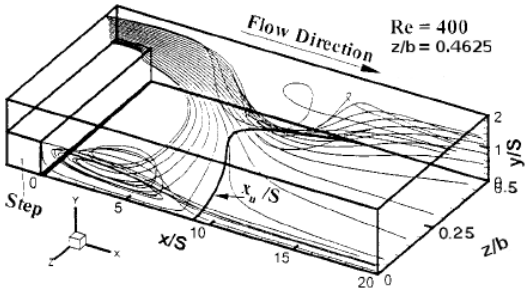

Figure 1.12. Streamlines starting from the spanwise plane of $z/b = 0.4625$. Source: Nie and Armaly [49].

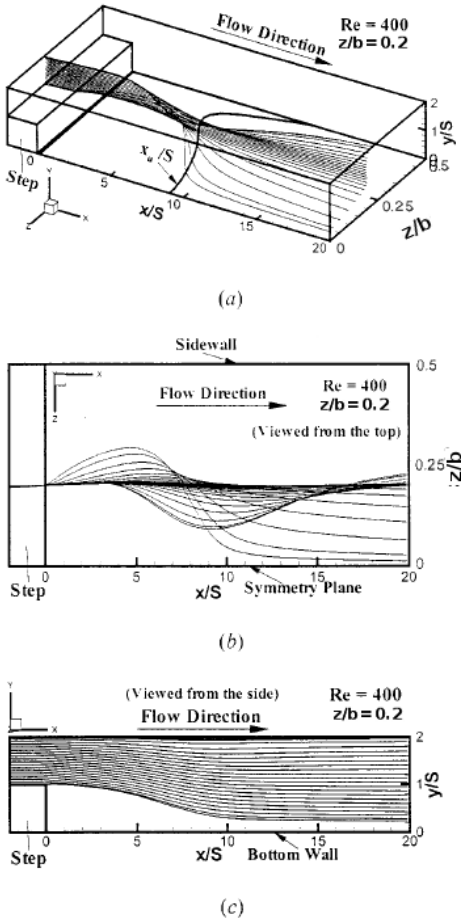

Figure 1.13. Streamlines starting from spanwise plane of $z/b = 0.2$. Source: Nie and Armaly [49].

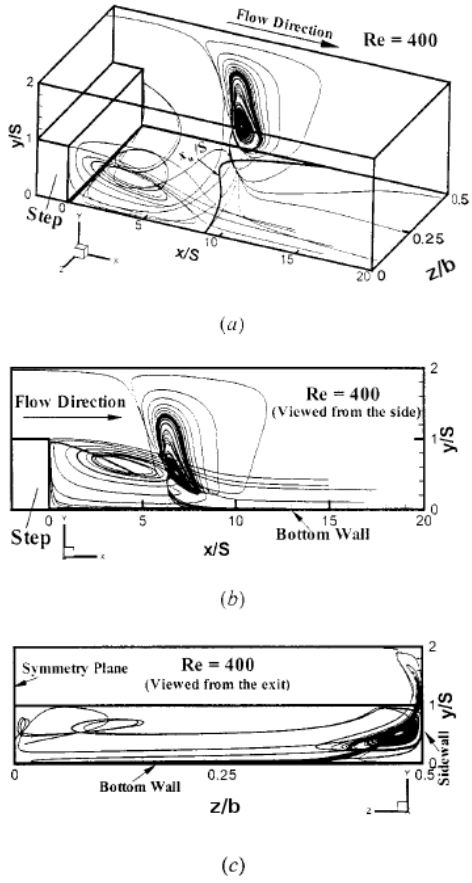

Figure 1.14. Jet-like flow and the recirculation region that develops adjacent to the sidewall. Source: Nie and Armaly [49].

bounds toward the sidewall (see Fig. 1.10 and Fig. 1.12). Another fraction of the incoming fluid from that region flows directly into the primary recirculation flow region and the remaining portion flows towards what appears to be a reattachment on the stepped wall. A fraction of that fluid rebounds and moves sharply toward the upper region of the sidewall and splits with a portion flowing upstream toward the step and another portion flows directly downstream. Fluid origination at the inlet plane of the duct in the region between $0,25 > z/b > 0$ flows directly downstream after approaching the stepped wall and does not appear to contribute to the primary recirculation flow region (see Fig. 1.13). Adjacent to the sidewall there develops a recirculation flow region producing jet-like flow that has shape of a teardrop with thin upper section and realatively thick lower section (see Fig. 1.14). Fluid from that jet-like flow flows partially upstream into the primary recirculation flow region

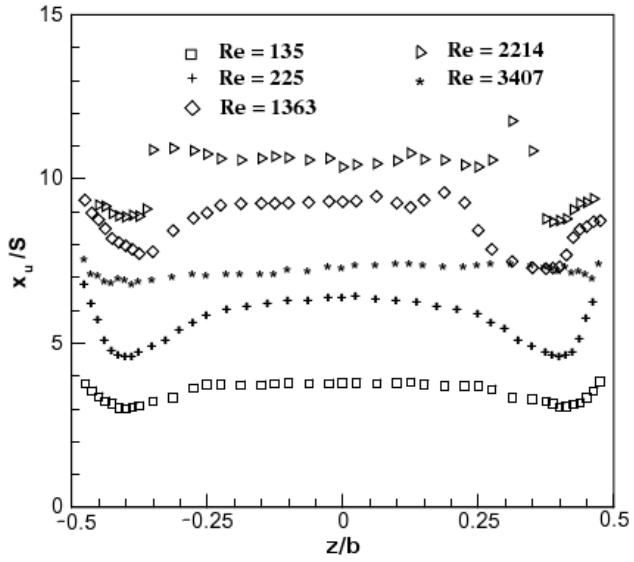

Figure 1.15. Spanwise distribution of reattachment length at the stepped wall. Source: Nie and Armaly [50].

and partially downstream (see Fig. 1.14). The impingement of jet-like flow on the stepped wall was responsible for the maximum in heat transfer coefficient at this point.

Armaly et al. [7] experimentally confirmed complex character of the flow adjacent to the sidewalls that is responsible for the three-dimensionality of the flow, which is impossible to describe by simple two-dimensional study. Same authors conducted experimental measurement in duct of $ER = 2.02$ and $AR = 8$ [50] that showed similar development of reattachment length versus Reynolds number at low $Re < 400$ as in measurements conducted by Armaly [5]. The spanwise profile of reattachment lenght was symmetrical at low Reynolds numbers, see the profiles at $Re = 135$ and 225 (Fig. 1.15). The symmetry was lost in the transition flow region as for the case of $Re = 1363$ and 2214, but in fully developed turbulent flow region the symmetry is recovered $Re \geq 3406$.

Kitoh et al. [37] conducted direct numerical study of the expansion ratio affect on the reattachment process behind a backward-facing step. On the contrary to the results of Nie et al. [48], they varied the height of the inlet part and kept constant aspect ratio $AR = 36$. They come to the conclusion that the reattachment length at the symmetry plane decreases as the expansion ratio is increased (see Fig. 1.16) what is in agreement to the previous result of Ötügen [52]. Together with the increased expansion ratio, the critical Reynolds number of the transition origin decreases from $Re = 681$ to 486 for $ER = 1.5$ and $ER = 2$, respectively.

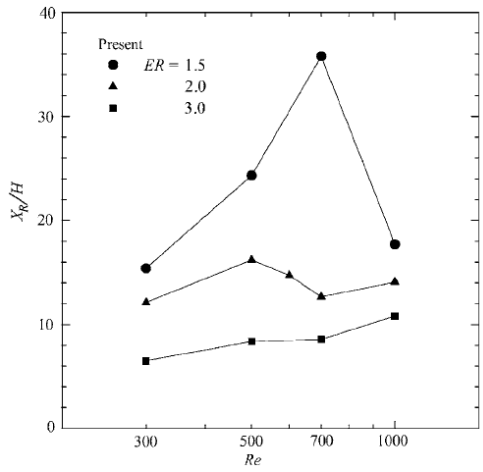

Figure 1.16. The effect of the expansion ratio on the reattachment length at the symmetry plane. Source: Kitoh et al. [37].

In the case of $ER = 3$ they have not observed any sudden variation of x_1/S. In the case of the duct with expansion ratio of a value $ER = 1.5$ there was no prove of an existence of the secondary recirculation flow region adjacent to the upper wall near the symmetry plane, but they found it adjacent to the sidewalls. The streamlines of virtual particles starting from the spanwise plane of $z/b = 0,4722$ bend quickly into the primary recirculation flow region, where they spirally move towards the duct middle plane and follow in the downstream direction. However, the spanwise location downstream the step which the particles move to, depends strongly upon both Reynolds number and expansion ratio. Where in the case of $ER = 2$, the fluid particles move almost to the channel middle plane at $Re = 291$ (Fig. 1.17), but in the case of Re = 700 this movement reaches only up to the spanwise plane of $z/b = 0.305$ (see. 1.18). The spanwise location up to which the particles spirally move becomes wider when the expansion ratio was decreased, what demonstrates strong sidewall effect for low expansion ratios. Figure 1.19 represents instantaneous isosurfaces of the ensotrophy $\omega = 2$ for $ER = 2$ and Reynolds number $Re = 681$ in order to clarify the three-dimensional vortical structure in the flow. The small scale vortices are radially shed from the two spanwise locations of about $z/b = \pm 0,278$ in the reattachment region. Some vortices are also shed from the longitudal vortices, which locate steadily in the neighbourhood of the sidewalls. Similarly, the vortices of various scales are detected in the entire field in region x/S from 20 to 30.

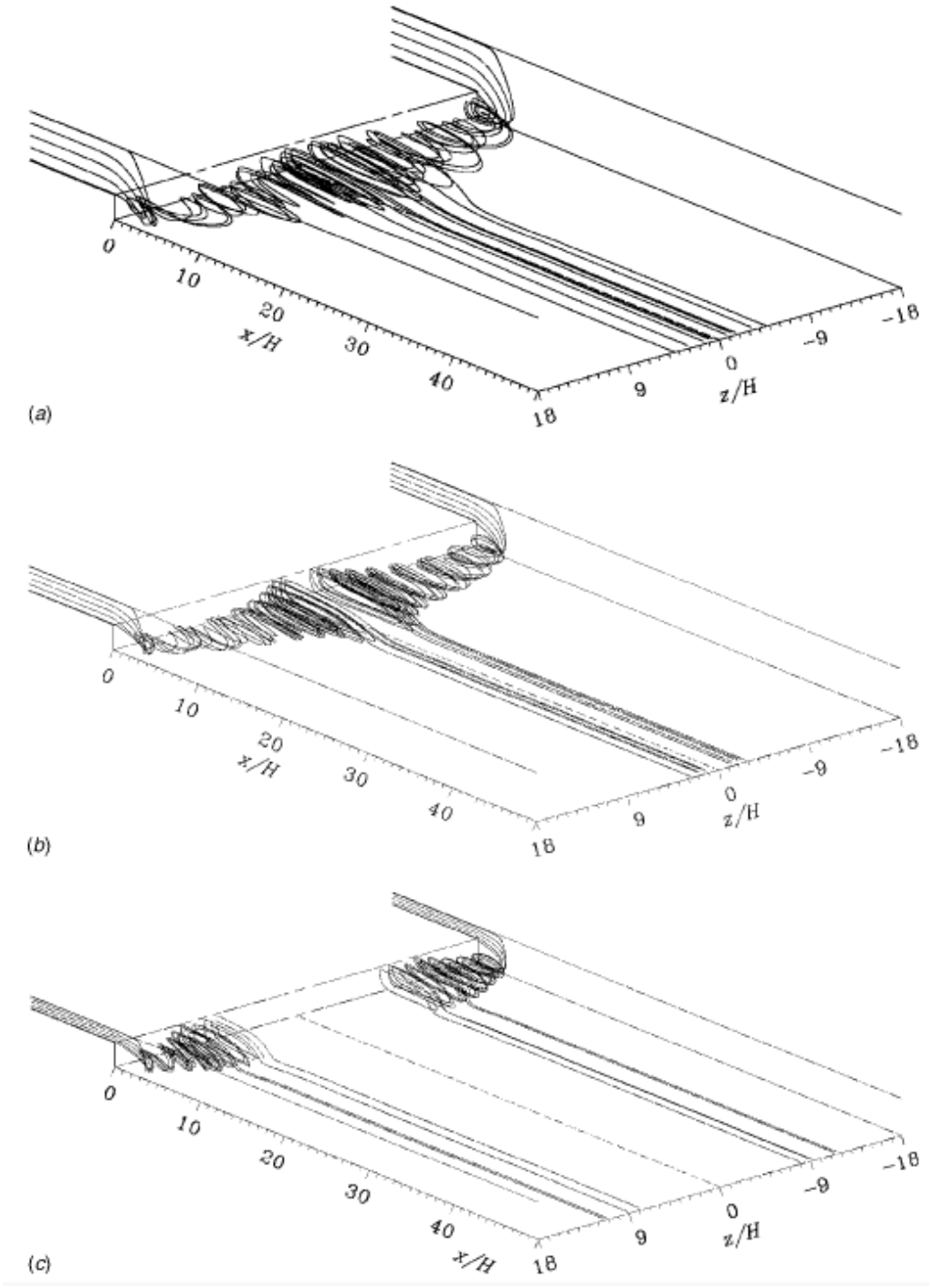

Figure 1.17. Streamlines at $Re = 291$, a) $ER = 1.5$, b) $ER = 2$, c) $ER = 3$. Source: Kitoh et al. [37].

Isomoto and Honami [30] observed the effect of inlet turbulence intensity on the reattachment process. They installed various grids at the beginning of the inlet part in order to change the free stream turbulence. They obtained values free stream turbulence intensity ranging from 0.25% in the case without grid up to 7.4% at the reference point located

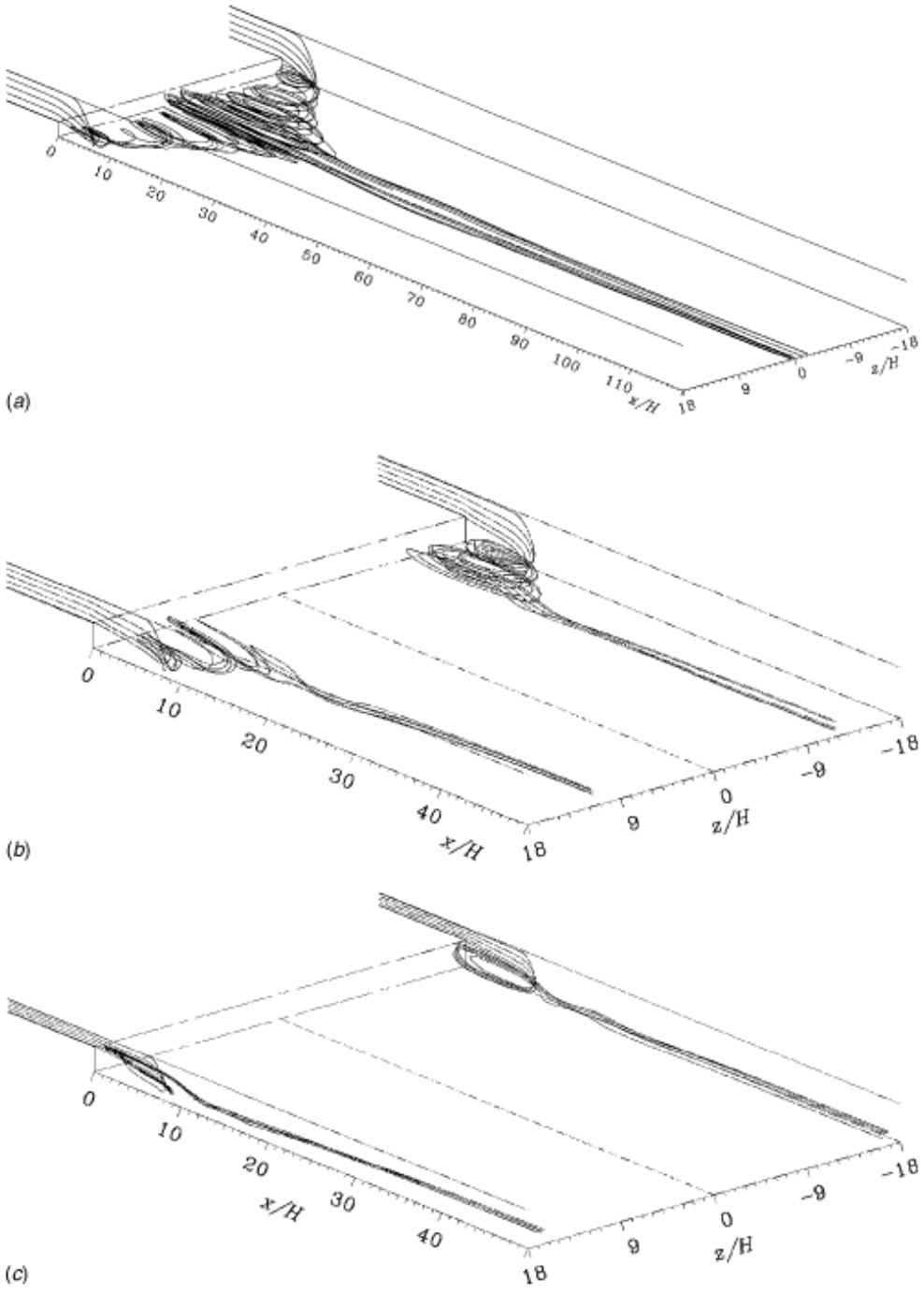

Figure 1.18. Streamlines at $Re = 681$, a) $ER = 1.5$, b) $ER = 2$, c) $ER = 3$. Source: Kitoh et al. [37].

160 *mm* upstream from the step edge. As the turbulence intensity in the free stream increases due to the inserted grids, the reattachment length shortens from initial value $x_1/S = 8.21$ in the case without a grid to value 6.28 in case with grid with highest increment of free stream turbulence intensity. However, they were not able to find out if the reattachment length is more dependent on the free stream turbulence intensity or on the turbulence inten-

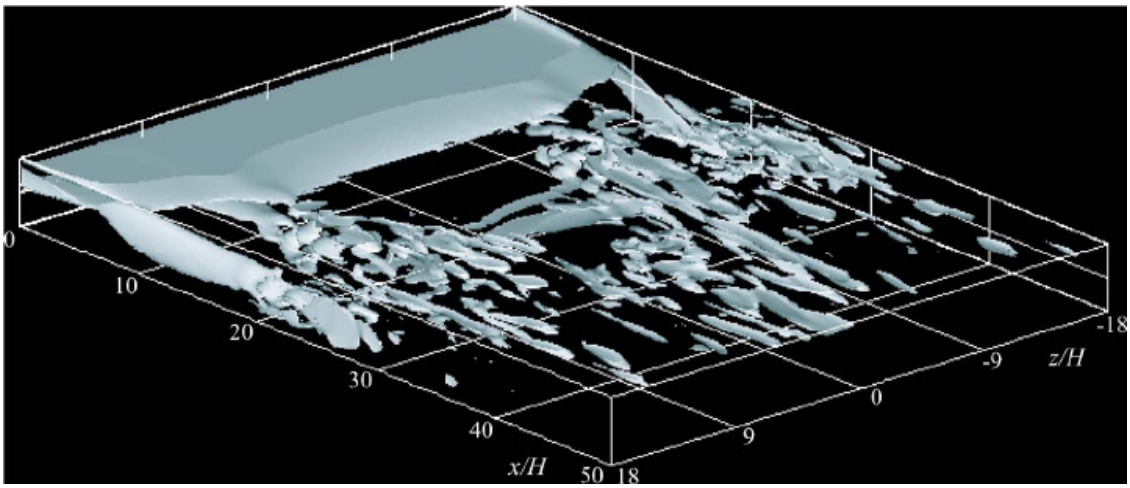

Figure 1.19. Isosurfaces of instantaneous ensotropy at $Re = 681$, $\omega = 2$ and $ER = 2$. Source: Kitoh et al. [37].

sity inside the boundary layer while the utilisation of a grid increases turbulence intensity in both regions (Fig. 1.20). In order to change the turbulence intensity inside boundary layer, they created cavity at the distance of $0,5\ x/S$ from the step edge and of the same width and depth, thus they obtained local increase of turbulence intensity observed at $y^+ = 100$ (see Fig. 1.21). So it was possible to obtain increased turbulence intensity at the near-wall region as well as small defect of the velocity profile at the separation point, however, already at distance of $x/S = 1.25$ from the step no changes in the turbulence intensity profiles as well as in the velocity profiles were observed. Although the turbulence intensity distributions are locally different, the reattachment length is the same and thereby it means that the

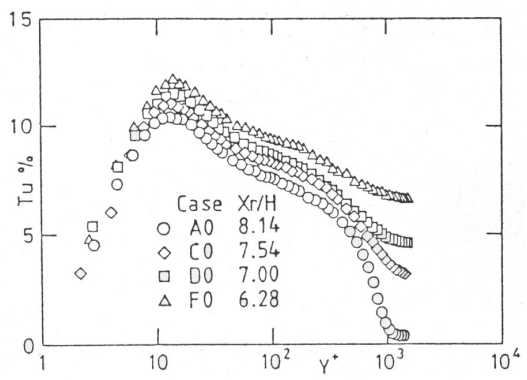

Figure 1.20. Turbulence intensity profiles at separation point. Source: Isomoto and Honami [30].

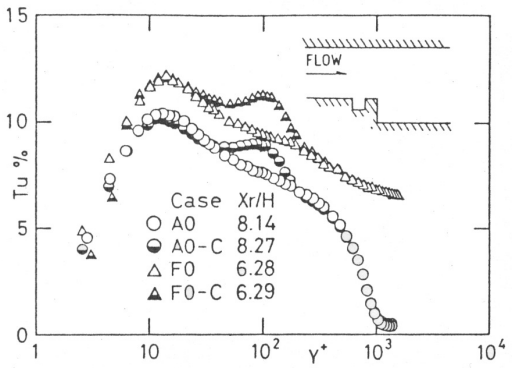

Figure 1.21. Turbulence intensity profiles at separation point with and without cavity. Source: Isomoto and Honami [30].

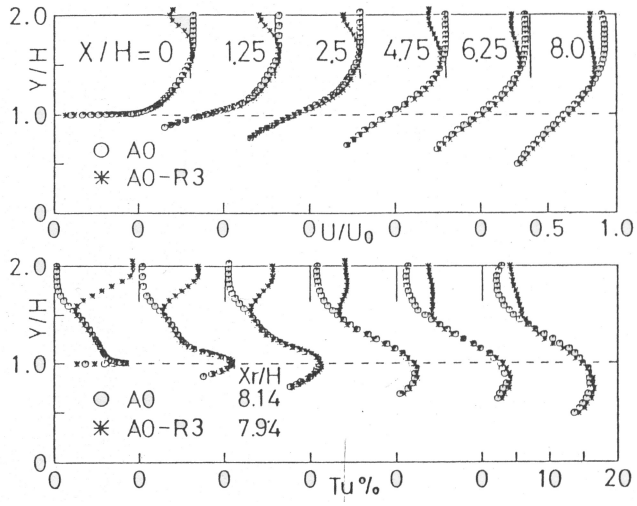

Figure 1.22. Velocity and turbulence intensity profiles for two cases with and without a rod in the freestream. Source: Isomoto and Honami [30].

local turbulence near $y^+ = 100$ generated by the cavity has no affect on the reattachment process.

Further they examined the effect of rod inserted in the free stream region. Indeed the turbulence intensity in the free stream region increased as well as the velocity decreased in this region but both the turbulence intensity profile and the velocity profile are almost identical within the shear layer (Fig. 1.22). These results indicate that free stream turbulence has no direct affect on the development of the inner mixing layer and the reattachment processes in the separated shear layer.

Similarly a local increase of turbulence near the boundary layer edge ($y^+ = 1000$) was attained when they placed a rod of 5 *mm* in diameter at the edge of boundary layer

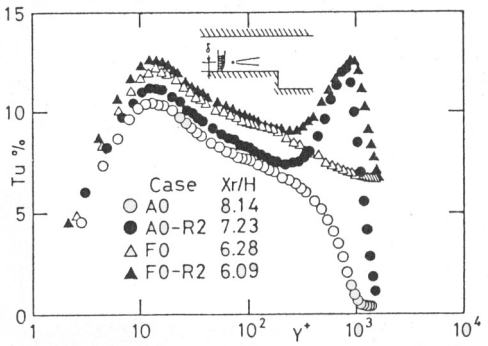

Figure 1.23. Turbulence intensity profiles when a rod is placed at the boundary layer edge. Source: Isomoto and Honami [30].

and also moderate overall increase of turbulence intensity from wall to the inner boundary layer was observed that led to abbreviation of reattachment length (Fig. 1.23). However, the reattachment length in the case of the rod placed at the edge of boundary layer without any perturbation of free stream flow was longer than in the case when the free stream flow was perturbed only by the grid, that the most increased the free stream turbulence. It seems, that the correlation between reattachment length and turbulence intensity at the edge of boundary layer is low.

When the rod of 3 *mm* in diameter was placed in the outer boundary layer, a local increase of turbulence intensity was observed at $y^+ \cong 500$, however, the reattachment length in this case was longer than in the case without the rod. Further they found that the turbulence intensity in the range of $y^+ = 100 - 200$ has no affect on the reattachment length as in the case with the cavity. Therefore, turbulence intensity in the region where y^+ is more than 50 is considered to have no direct effect on the reattachment process from the experimental results with the cavity or rod. They found correlation factor of value 0.987 between reattachment length and the maximum turbulence intensity, which is extremely high. It is interesting to note that only a change in 2 percent of turbulence intensity near the wall introduces a change of 2 step heights in the reattachment length (Fig. 1.24). They

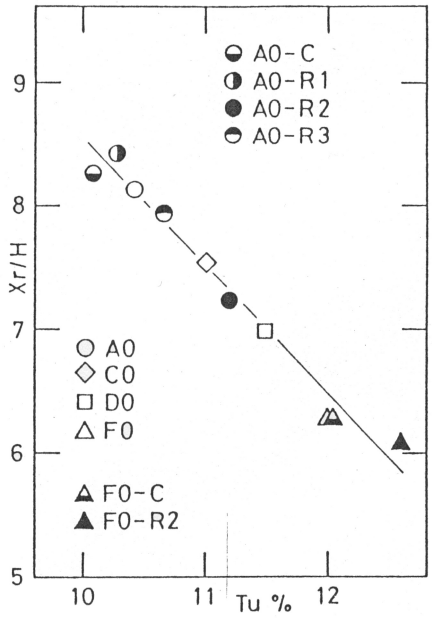

Figure 1.24. Reattachment length versus maximum turbulence intensity near the wall at hte separation point. Source: Isomoto and Honami [30].

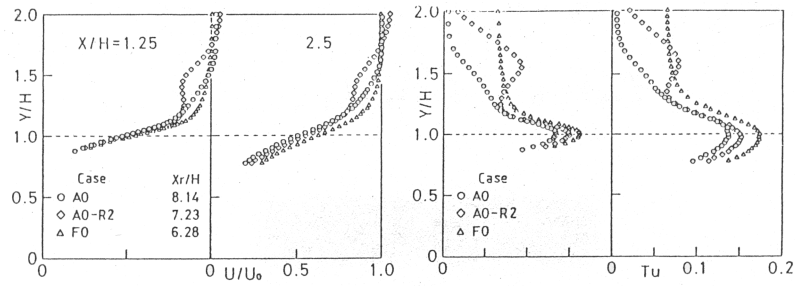

Figure 1.25. Turbulence intensity and velocity profiles in the entrainment region. Source: Isomoto and Honami [30].

found that the turbulence intensity in the entrainment region has substantial affect on the reattachment length (Fig. 1.25). Similar results could be found in the work of Badran and Bruun [8].

Hall et al. [27] conducted experimental study of a turbulent backward-facing step flow to investigate vortex structures behind the step with attention given to the secondary vortex, because of its potential for evaluating computational turbulence models. They conducted experimental measurements in channel with expansion ratio $ER = 1.5$ and aspect ratio $AR = 5$ using the PIV method. The chosen Reynolds number was $Re_S = 44000$ based on the step height. They conclude that secondary corner vortex is highly erratic, turbulent and contains reversing flow and flow structures are hardly to describe during any instant because of little meaning. However, the in the time averaged results the secondary corner vortex has well defined separation and reattachment points and a disticnt vortex center. Secondary vortex is highly three-dimensional (see Fig. 1.26 and Fig. 1.27). They found that the secondary corner vortex does not change its size from the symmetry plane towards sidewalls up to the spanwise plane of approximately $z = 100\ mm$ ($z/b = 0.4286$), where it undergoes changes due to the affect of sidewalls. It seems that the secondary corner vortex sheds from the bottom wall, reduces its size and curves towards the C corner that is defined as intersection of sidewall and the top corner edge. The primary vortex seems to be virtually eliminated by the sidewall effect at the spanwise plane of $z = 100\ mm$ ($z/b = 0.4286$), although the shear layer seems to remain. The separation points X_s and Y_s on the bottom wall and on the sidewall, respectively, are depicted in Fig. 1.26. X_s remains constant up to the spanwise plane of $z = 80\ mm$ ($z/b = 0.3429$) where it begins to shorten and becomes zero between $z = 95\ mm$ ($z/b = 0.4072$) and $z = 100\ mm$ ($z/b = 0.4286$), while Y_s seems to

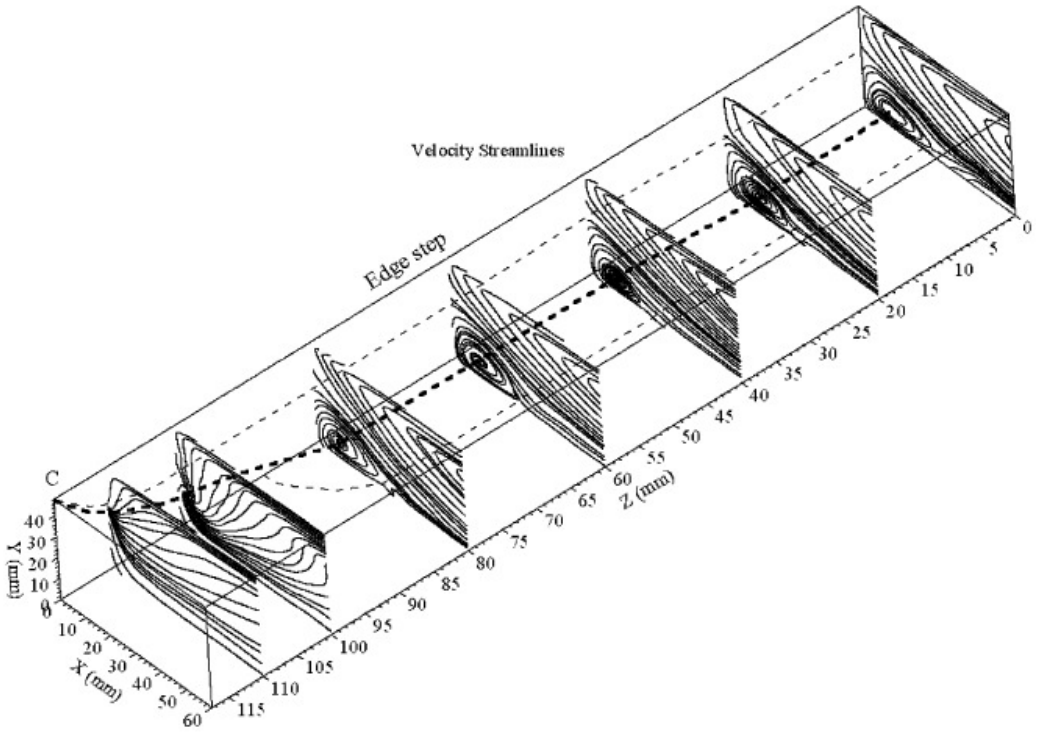

Figure 1.26. PIV streamlines for parralel planes. Source: Hall et al. [27].

join the wall at corner C, similarly as a curve for the center of the secondary vortex. From streamline results, they made important finding that streamlines spirally tend towards the center of the secondary corner vortex, what indicates a strong mass flow into the vortex core, which by conservation of mass must produce a z direction flow within the secondary corner vortex. According the results (see Fig. 1.26), they conclude that the spiral inflow

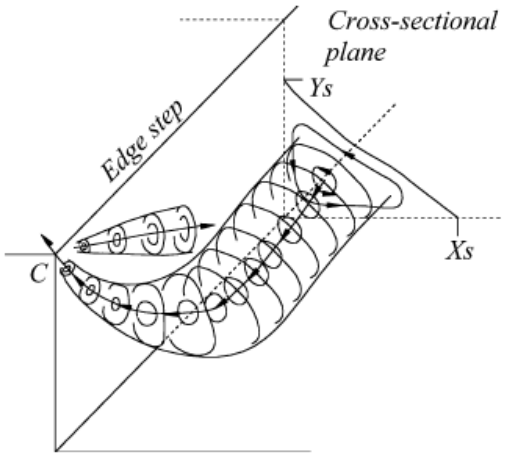

Figure 1.27. Mean flow structure for one half of the secondary vortex. Source: Hall et al. [27].

seems to become stronger further from the symmetry plane. Another conclusion they made was that the secondary corner vortex pulls fluid into its core and transports it across the step, delivering it to the high-speed shear layer adjacent to the corner C. The streamwise vortex, which is known to form at the corner C (Padoupoulosem and Oetuegenem [27]) is ilustrated in Fig. 1.27. They didn't find third corner vortex as predicted by the theory of Moffat [46] and numerical simulation by Biswas et al. [10].

Kostas et al. [39] conducted PIV experimental measurement in water channel with a backward-facing step geometry at $Re_S = 4660$ and $AR = 62$ a $ER = 1,02$. They identified secondary corner vortex similarly to Hall et al. [27]. They identified vortex street and vortex pairing within the separated shear layer in instantaneous vector fields.

Tihon et al. [63] used electro-diffusion technique to investigate reattaching and recirculating flows behind a backward-facing step with the aspect ratio $AR = 11$ and the expansion ratio $ER = 1.4$. They proved the existence of secondary flow behind the step, which extended up to dimensionless distance $x/S = 1.75 \pm 0.15$ and practically constant reattachment lenght near the dimensionless distance $x_1/S = 5.1 \pm 0.2$ in fully developed turbulent flow. They found small values of the fluctuating component of wall shear stress τ_w' in the corner region. However, the wall shear stress fluctuation were very large near the reattachment point, where large and energetic eddies are impinging on the wall. They located the maximum magnitude of near-wall flow fluctuation approximately one step height upstream of the reattachment point where the fluctuating component τ_w' reaches about 75% of the maximum level of τ_w.

The onset of three-dimensionality, equilibria and early transition of flow over a backward-facing step was numerically investigated by Kaiktsis et al. [34], who simulated flow in duct with expansion ratio $ER = 1.9423$ that is the same ratio as in experiment of Armaly et al. [5] for both cases, the two-dimensional and three-dimensional case, where the periodic boundary condition at sidewalls was used and the aspect ratio of the three-dimensional case was $AR = 6\pi$. According they results the onset of two- and three-dimensional instabilities occurs approximately at the same Reynolds number with the critical value $Re_c = 700$. The idea that the onset of three-dimensionality occurs in specific regions of the flow determined by the separation regions, and, in particular, at the boundaries be-

tween two separated stagnant flow zones and the bulk of the flow, was quantitatively verified through standard spanwise correlation coefficients and also by three different types of inhomogenity indices. This resulting three-dimensional states are 'stable' at finite amplitudes and they are periodic for slightly supercritical states ($Re > 700$) with the shear-layer frequency $f_2 = 0.104$ dominating everywhere in the field. At Reynolds number Re > 800 quasi-periodic states are formed which are characterized by two frequencies $f_1 = 0.504$ and f_2 that the former reflects the channel parabolic flow structure downstream and is same as the frequency corresponding to two-dimensional Tollmien-Schlichting (T-S) waves and the second is associated with the three-dimensionality effects of the flow which are more pronounced in the upstream inflexional region. The power spectrum at higher Reynolds number of the two-dimensional case was more wideband and it was therefore difficult for the authors to identify dominant frequencies. Using eigenvalue analysis they revealed a close resemblance of the fluctuating velocity field downstream with the channel T-S waves that typically encounter at higher Reynolds numbers, what is probably induced by the presence of an unstable shear layer upstream that causes excitation of these 'native' T-S waves even at strongly subcritical Reynolds numbers. In order to approximately determine critical Reynolds number Re_c they imposed initial perturbation as an external forcing for some initial period and removed after, the time trace of all velocity components were followed in time. At subcritical Reynolds numbers all initial perturbation in the velocity field decayed to zero and time traces at Re of the spanwise component revealed a rapid decay to zero suggesting that the flow returns to two-dimensionality. External excitation applied at the inlet boundary condition led to decrease of reattachment length when the forcing frequency corresponded to one of the natural frequencies f_1 and f_2. On the contrary, when the forcing frequency was different from the natural frequency of the flow, the reattachment length increased, in particular $f^*_1 = 0.0333$ and $f^*_2 = 0.565$.

However, based on their two-dimensional numerical simulation done in conjunction with stability analysis, local and global, (Kaiktsis et al. [35]), they later proved that this two-dimensional instability is in fact a convective instability for $Re \geq 700$. They verified this through observing development of perturbancies that were generated in the inlet part of the channel (by the means of impulsive excitation of shear layer and by impulsive excitation of the inlet). They credited this discrepancy in the results to the coarse resolution of

numerical simulation used in their previous work (Kaiktsis et al. [34]). This discretization 'noise' behaved as permanent forcing and thus completely changed the character of computed results and caused that the results showed global flow unsteadiness; thereby the convective instability was masked by this global unsteadiness. However, it is interesting, that the lower-resolution simulations also preserve the basic physics of this flow in that manner, that the distribution of fluctuations of the globally unsteady flow is found to be similar to the distribution of disturbances of the convectively unstable flow. Their numerical simulation demonstrated global stability to temporal perturbations up to $Re = 2500$, which is in contrast to real experiments, where the unsteadiness are triggered at lower Reynolds number as consequence of the presence of background noise (see Armaly et al. [5] $Re \leq 1200$).

Detailed three-dimensional stability analysis of the flow behind a backward-facing step was conducted by Barkley et al. [9]. Their analysis showed that the first absolute linear instability of the steady two-dimensional flow behind a backward-facing step with expansion ratio $ER = 2$ is a steady three-dimensional bifurcation. They computed, with high precision, the critical Reynolds number and spanwise wavelength of the instability and found the critical Reynolds number $Re_c = 997$ and $\lambda_c = 6.9$ in non-dimensional units based on the step height and the centerline velocity of the inflow (seeFig. 1.28). They have not found a two-dimensional bifurcation from the steady flow. They found that the critical

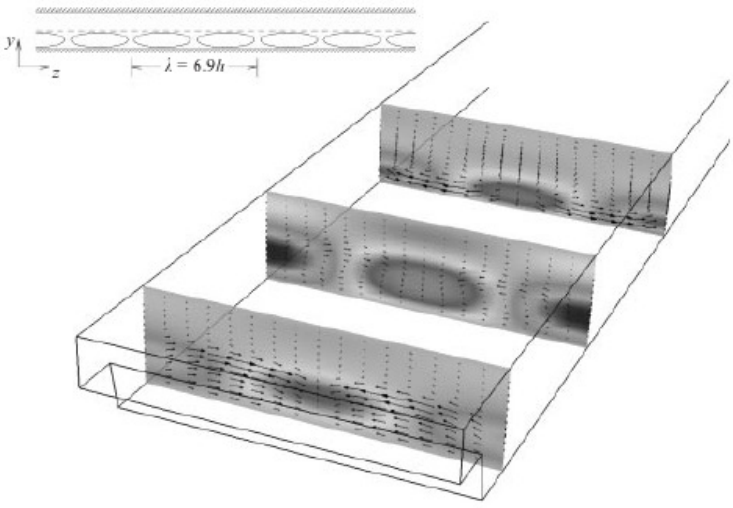

Figure 1.28. Three-dimensional flow structure of the critical eigenmode at $Re = 1000$ and $\beta = 0.9$. Contours indicate the strength of the streamwise velocity component and vectors show the (v, w) flow pattern in each cross-sectional plane: $x = 1.2,\ 6.2$ and 12.2. Source: Barkley et al. [9].

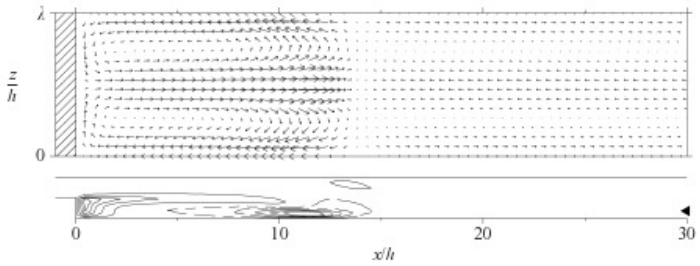

Figure 1.29. Sections of the critical three-dimensional eigenmode. Upper plot show (u, w) velocity vectors in the plane $y = -0.65$ (indicated by a triangle at the right of the lower plot). The lower plot contains w velocity (in the plane $z = \lambda/4$) with solid and dashed contours indicating the sign of w. Source: Barkley et al. [9].

eigenmode consists of a flat roll localized to the primary recirculation region behind the step edge (see Fig. 1.29) and that the secondary recirculation zone on the top wall and the core between the primary and secondary recirculation zone is not the locations, where at linear level the instability does arise as was previously described in study of Kaiktsis et al. [34]. They ruled out a Taylor-Görtler-type instability of the main flow as the source of three-dimensionality in experiments, but have argued that centrifugal instability is responsible for generating secondary flow with the separation zone.

Furuichi et al. [22] investigated vortex structures behind a backward-facing step with aspect ratio $AR = 11$ and expansion ratio $ER = 1.5$ using advanced multi-point Laser Doppler Velocimetry (LDV). They simultaneously obtained two spatio-temporal velocity fields $u(y, t)$, one at the separated shear layer $x/S = 3$ and the second one at reattachment region $x/S = 6 \sim 7$, these data were subject of a space and time correlation and conditional average calculations. Two high correlation areas of different y/s locations were found with a temporal distance $tU_b/S \approx 5$ what correspond the travelling velocity of the vortex structure shedding from the separated shear layer, which equals half the movement velocity of main flow. They calculated a two-point correlation coefficients focusing on the reverse flow from reattachment region to the separated shear layer. The time variation of the correlation coefficient revealed a peak at $tU_b/S \approx 17$, which clearly indicates that the fluctuation in the reattachment region influences the behaviour of the separated shear layer. The total period of one cycle (eg. the travelling time of the vortex from the separated shear layer to the reattachment region and its reverse by the recirculation flow) was found to be $tU_b/S \approx 22$ with corresponding Strouhal number $fS/U_b = 0.045$. This differs from the results of direct

numerical simulation of Le et al. [41], who simulated flow behind a backward-facing step with expansion ratio $ER = 1.2$, aspect ratio $AR = 8$ and Reynolds number $Re_S = 5100$. They revealed that the reattachment location oscillates around mean value $x_1/S = 6.28$ in range of $5 < x_1/S < 7.5$ with Strouhal frequency $St = fS/U_b = 0.6$. Le et al. [41] compared calculated velocity profile with the universal log-law profile and they revealed that all profiles were below universal log-law profile even at $x/S = 20$ downstream of the step.

Lee and Sung [42] and [43] utilized array of 32 microphones to measure wall pressure fluctuations in separated and reattaching flow over a backward-facing step at Reynolds number $Re = 33000$. Their pressure spectrum reached a maximum at $fS/U_0 \sim 0.068$ which is nearly the same as the result by Eaton [20] $fs/U_0 \sim 0.066$ (as mentioned in [42]). They revealed two modes of shed vortices, one is the global oscillation and the other is the vortex convection which are synchronized with the flapping frequency component of pressure fluctuations of frequency $fS/U_0 = 0.01358$. They described the possible scenario of the vortical motion as follows: first, a global intense oscillation appears with contraction of the separation bubble. As the bubble is enlarged, the separated shear layer receives positive momentum in the streamwise direction. After a quiscent period, a large scale vortical structure emerges and is then accelerated to form an orderly structure behind it. Second, these periodic vortices convect downstream and finally, the vortices are decelerated and the next global oscillation redevelops. The flapping frequency component of the pressure fluctuations is shown to develop a standing wave up to $x/s = 10$ and after this point its magnitude decreases significantly.

Sakuraba et al. [61] were concerned in the affect of suction and injection from a slit at the bottom corner of the step on the pressure drop and heat transfer coefficients in channel with expansion ratio $ER = 1.5$. The measurements were conducted using constant thermoanemometry technique with film probe for various slit width and various flow ratio. They have not found any affect of the split width either to the pressure coefficient or to the Nusselt number. In the case of injection they observed an increase of pressure drop coefficient while there was fall in values of the Nusselt number and thus the injection was found to be inconvenient. On the contrary, in the case of suction a fall of pressure drop coefficient was observed while the Nusselt number increased. Due to the suction, a drop

of reattachment lenght up to 75% was achieved and the turbulence intensity adjacent to the step increased. DNS and LES study of Neumann and Wengle [47] showed 13% fall of reattachment length when passive flow control elements were built-in into the bottom wall upstream the step edge.

1.2. Summary of the recherche

Based on this survey of the literature it can be concluded that there has been presented plenty of experimental and theoretical publications covering the problem of dependence of the reattachment length on Reynolds number in two-dimensional channel or in channels with high aspect ratio, where the flow near the symmetry plane can be considered as two-dimensional (experimentally and numerically: Armaly et al [5], Nie and Armaly [50], numerically: Kitoh et al. [37]).

Some of the presented works put stress on the aspect ratio effect, but only results of a numerical simulations of a wide range of aspect ratios was discussed (Iwai et al. [31]) and no complete experimental data for wide range of aspect ratios, ranging from very narrow channels with strongly three-dimensional flow structure to very wide channels with two-dimensional flow structure limited near the symmetry plane, were provided. However some works deal with narrow channels (experimentally: Armaly et al. [7], numerically: Chiang and Sheu [15], Nie and Armaly [48], [49], experimentally and numerically: Nie and Armaly [50]) and some works with wide channels (numerically: Biswas et al. [10], Chiang and Sheu [16], Kitoh et al. [37], Williams and Baker [67]).

The influence of varying step height and-or expansion ratio, is also unclear, since present publications provide contradictory results, either concluding the reattachment length is increasing with increasing expansion ratio or vice versa (numerically: Biswas et al. [10], Nie and Armaly [48] and Kitoh [37], experimentally: Ötügen [52]). As already noticed in the recherche section, this could be due to different treatment of aspect ratio when expansion ratio was changed.

Several works deal with the onset of the transition regime. However the theoretical works (Barkley et al. [9], Kaiktis et al. [34], [35]) indicate that the onset of transition takes

place at higher Reynolds numbers than results the experimental data (Armaly et al. [5]). They credited this discrepancy to the disturbances, which are always present in the real experiments and which can not be eliminated.

There are many of other fields of interest such as heat transfer, passive or active flow control, mostly sparsely published. Few works, mainly theoretical, provide some data with the stress on heat transfer (numerically: Nie and Armaly [48], Kitoh et al. [37]) and heated walls. Flow control based on varying turbulence intensity of the inlet flow and insertion passive flow control elements upstream the step edge was presented experimentally by Isomoto and Honami [30], Badran and Bruun [8]. Active flow control based on suction or injection fluid from a slit in the step wall near the bottom wall was experimentally investigated by Sakuraba et al. [61].

Recent enhancements in experimental methods, especially the particle image velocimetry (PIV), provide more complex information about the flow structure and help better understending of the phenomena involved. Some works that deal with PIV were presented by Hall et al. [27], Kostas et al. [39], Pirto et al. [53], [54] and Albrecht [4].

Existence of complete experimental database taking into account all possible parameters with an influence on the flow structure is of an extreme importance especially as a benchmark test source for validation of numerical turbulence models, yet the effort to conduct such measurements is immense.

1.3. The aim of the work

The aim of this work is the aspect ratio effects investigation and the endeavour to provide more complete experimental data set over a wide range of aspect ratios and over a wide range of Reynolds number ranging from laminar flow to the onset of transition and part of the transition regime. Still parameters like varying expansion ratio, turbulence intensity of the flow in the upstream section, etc. lie out of the scope of this work.

Both experimental and numerical investigation will be provided. In the experimental part four channels of different aspect ratio will be scanned using particle image velocimetry (PIV), a modern non-intrusive flow investigation method yielding two-dimensional in-

stantaneous velocity fields. In the numerical part of the work effort will be aimed to clarify some opaque details mainly emanating from three-dimensionality of the flow, which can not be resolved using simple two-dimensional PIV method.

Chapter 2. Experimental setup

2.1. Experimental channel with backward-facing step geometry

The experimental investigation was conducted in four channels with rectangular cross-section that were made from transparent plexi-glass. Each of the channels had different width with values 53 *mm*, 80 *mm*, 173 *mm* and 332 *mm*. The upstream section was 1 *m* long, 10 *mm* height and suddenly expanded in one direction, thus the downstream section was 20 *mm* height and 2 *m* long. This geometrical configuration resulted in constant expansion ratio for all channels given as

$$ER = \frac{H}{h} \tag{2.1.1}$$

where H is the downstream section height and h is the upstream section height as illustrated in Fig. 2.1, so the expansion ratio is $ER = 2$. While the expansion ratio was same for all geometries, the aspect ratio, expressed as

$$AR = \frac{b}{h} \tag{2.1.2}$$

where b is the channel width, so $AR = 5.3$, 8, 17.3 and 33.2 is achieved. Such a wide range of aspect ratios was chosen in order to get fundamentally different flow conditions inside the investigated geometry, varying from fully three-dimensional with strong sidewall effect $AR = 5.3$ to very wide channel $AR = 33.2$, where two-dimensional flow can be expected at least close to the symmetry plane, as was predicted by Iwai et al. [31]. Sidewalls were 8 *mm* thick with grooves to accommodate top and bottom wall, which were 10 *mm* thick. Sidewalls were fixed together by 32 steel threaded rods. Two pairs of thread mutters at each rod fixed the distance between sidewalls as shown in Fig. 2.2. In order to avoid deflection of wide channels, small block with hole for the threaded rod was mounted on the bottom and top wall. The upstream section was attached to the settling chamber, which was 1000 *mm*

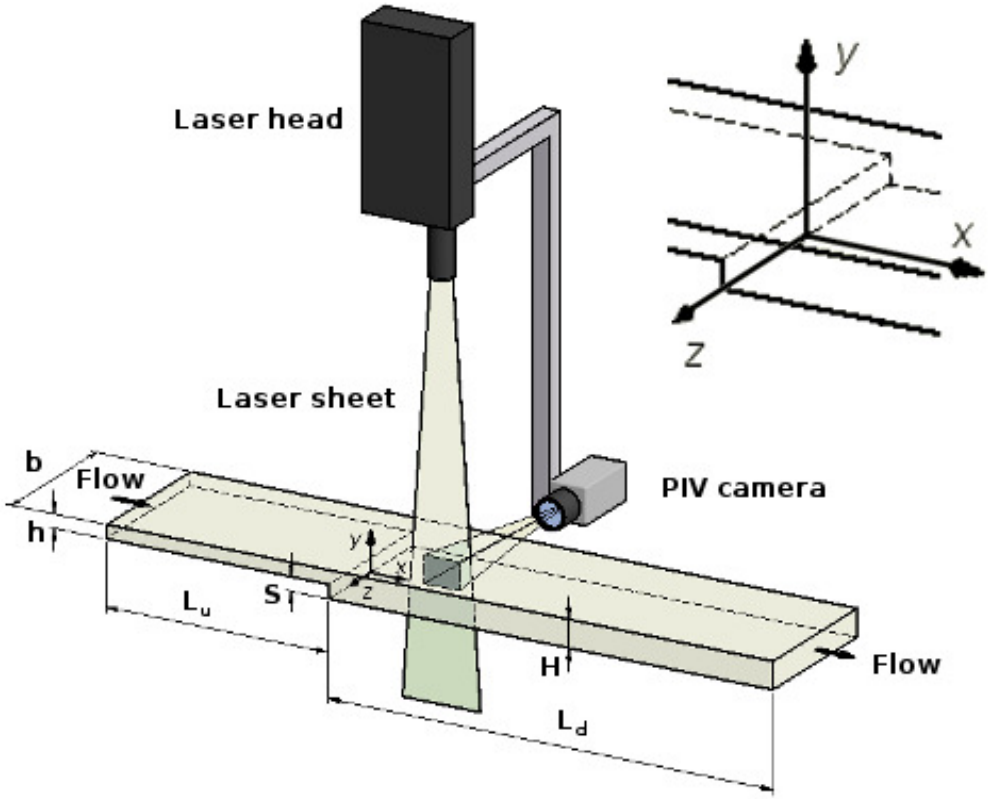

Figure 2.1. Schematical view on the apparatus layout with geometrical notation and coordinate system orientation.

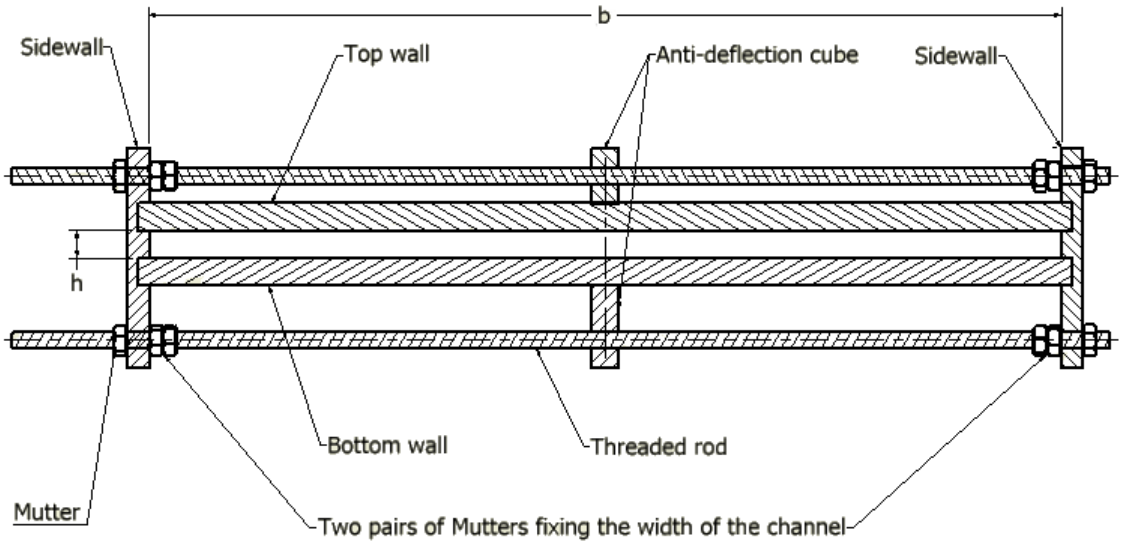

Figure 2.2. Cross section showing the threaded rods fixing the sidewalls.

long, 200 *mm* high and 600 *mm* wide, equiped with 393 *mm* long pyramidal diffusor where the inlet hose was attached (see Fig. 2.4). The inlet diffuser and first 200 *mm* of the settling chamber was filled with foam in order to avoid vortex shedding in the diffuser section because of the large angle of the diffuser and partly to achieve homogenous isotropic turbulence in the entire cross-section of the settling chamber. The passage from the settling chamber to the upstream section was in the case of $AR = 5.3$, 17.3 and 33.2 formed by simple rounded edge with 5 *mm* radius as is illustrated in Fig. 2.4 detail A and Fig. 2.3 a). In the case of channel with $AR = 8$, aluminium profile of shape ilustrated on Fig. 2.3 b) was clued before the inlet of the channel. An alcohol thermometer was inserted inside the settling chamber, 400 *mm* before the channel inlet (marked as 't' in Fig. 2.4), in order to measure the air temperature. In order to obtain information about the pressure in the settling chamber, a declinable U-tube manometer was tapped to the pressure connection, which was placed 300 *mm* before the channel inlet (marked as 'p' in Fig. 2.4). The channel flow is supplied by compressed air, which was after purification and drying stored in com-

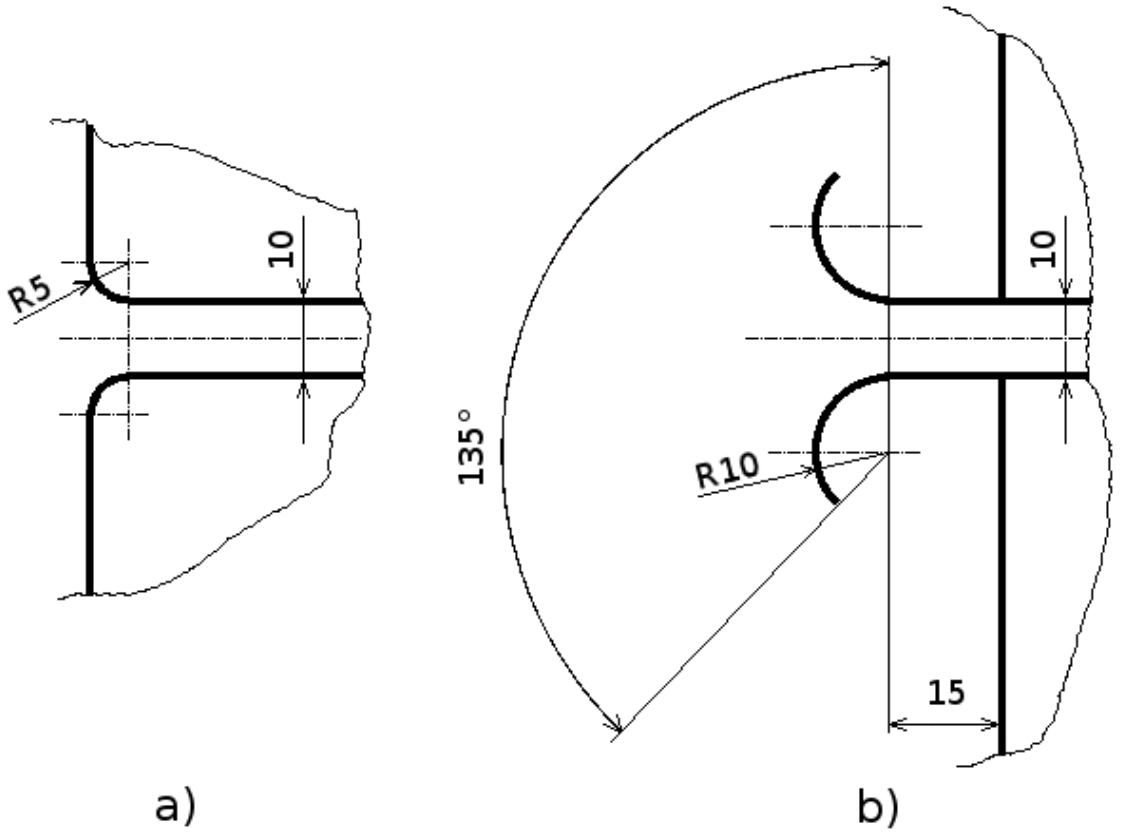

Figure 2.3. Detailed view of channe inlets. a) channels with $AR = 5.3$, 17.3 and 33.2, b) channel with $AR = 8$.

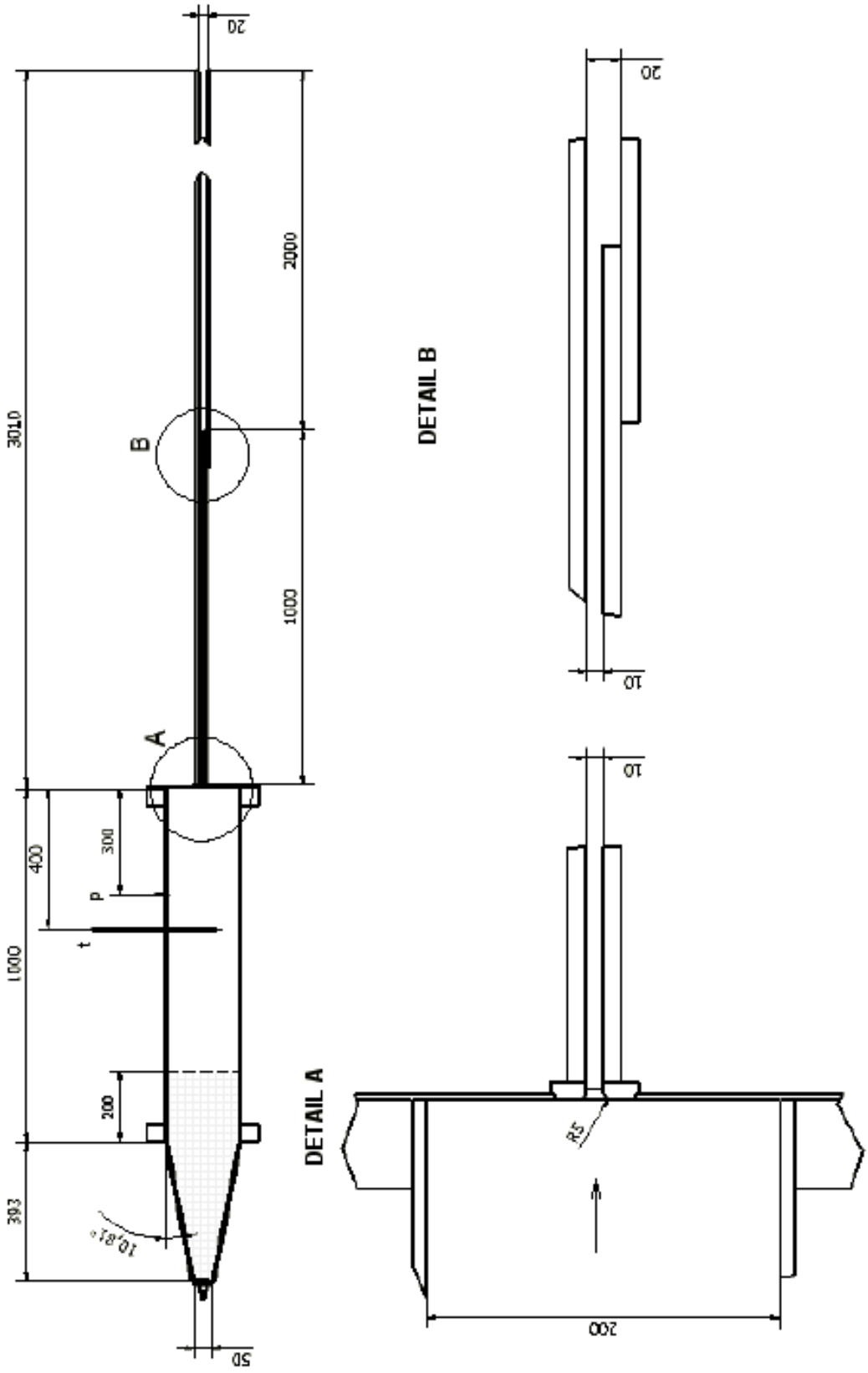

Figure 2.4. Channel geometry - cross-section throug symmetry plane.

pressed air tanks (not shown in the layouts) and kept at constant gauge pressure 700 *kPa*. The pressure tank serves as part of compressed air distribution system in the laboratory, where pressure regulation system allows constant output pressure to be adjusted. Alcohol thermometer was installed in the compressed air distribution system to give the information about source air temperature. The transforming valve was set so, that the air pressure at the inlet of the flow rate instrumentations was 200 *kPa*. The presence of tracking particles disabled any conventional flow rate measurement after the seeding process, because the tracking particles, i.e., the air droplets consequently settled either at the tip of pitot tube or on the float of rotameter. To remedy this, the flow rate was measured before seeding. Two separated branches (see Fig. 2.5) were necessary in order to achieve optimum density of seeding particles. In the first branch pure air was led through rotameter directly to the settling chamber (the upper branch in Fig. 2.5), while in the second branch an atomizer was installed downstream from the rotameter output. The atomizer output was than connected to the output of the pure air branch and eventually connected to the settling chamber. The air flow rate in both branches was adjusted by virtue of adjusting valve, which is part of the rotameter. At the output of the rotameters Bourdon tube type manometers were tapped to measure the output air pressure in order to correct the density according actual pressure and temperature, while the rotameter was calibrated for standard pressure and temperature of the air. Finally, the air flow rate in the channel is arithmetical sum of flow rates through both branches $\dot{Q} = \dot{Q}_1 + \dot{Q}_2$ corrected with respect to the temperature and pressure inside the settling chamber according relation:

$$\dot{Q}_i = \dot{Q}_{mi}\sqrt{\frac{p_{bi}}{p_{flow}}\frac{T_{flow}}{T_{src}}} \tag{2.1.3}$$

where barometric pressure p_{bi} is the sum of ambient and manometric pressure $p_{bi} = p_{amb} + p_{mi}$. Reynolds number is defined by hydraulic diameter and the bulk velocity in the upstream section:

$$Re = \frac{U_b d_h}{\nu} \tag{2.1.4}$$

where the bulk velocity in the upstream section is calculated from

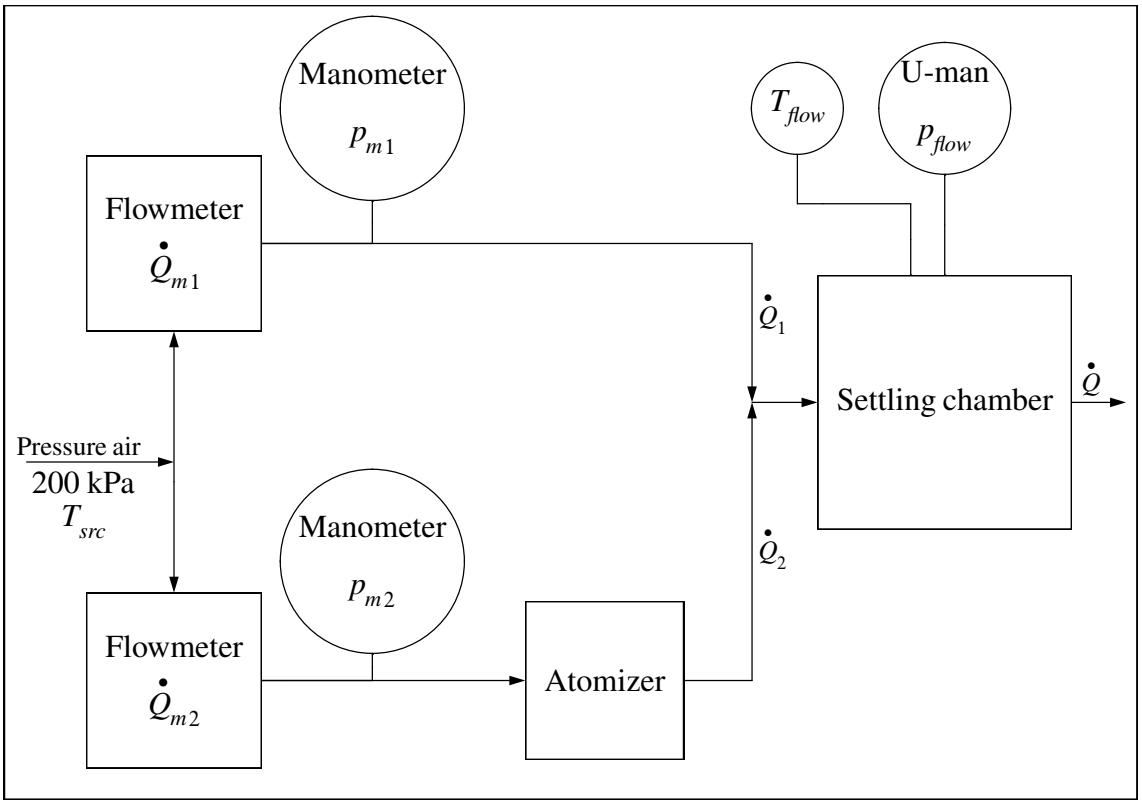

Figure 2.5. Flow instrumentation installation layout.

$$U_b = \frac{\dot{Q}}{b\,h} \tag{2.1.5}$$

the hydraulic diameter as

$$d_h = \frac{4A}{P} = \frac{4bh}{2(b+h)} = \frac{2AR}{AR+1} \tag{2.1.6}$$

and where ν is the kinematic viscosity defined by the air temperature and by the static pressure inside the settling chamber. The aerosol (air mixed with the seeding particles) was issued into the lavatory space though open exit section of the channel and eventually exhausted by lavatory ventilation system.

2.2. Experimental apparatus

The Nd:YAG laser with dual laser head system was source of the light (here New Wave Research - Gemini was employed). Second harmonic generator, part of the laser system,

produced visible green light with the wavelength of $\lambda = 532$ *nm*, which is ideal because being visible for human eyes and because of the high sensitivity of the camera at this wavelength. The laser was operated in Q-switched mode with maximum energy output 120 *mJ* per pulse and 10 *ns* duration. The laser beam passed through laser sheet optics, where laser sheet of low divergence and controlled thickness was created. The laser sheet thickness was adjusted to approximately 0.7 *mm*.

A CCD 12-bit double-frame mode camera (HiSense from Dantec) was used to record the double frames. The camera resolution is $1280x1024$ pixels with 6.7 μm pixel pitch. AF Micro-NIKKOR 60mm $f/2.8D$ from Nikon was mounted on the camera. Dichoric filter was employed to pass light of the wavelength 532 *nm* in order to reduce the background noise in that only the light of this wavelength, i.e., the same wavelength used for the illumination, is passed through the optics. Liquid Seeding Generator LS-10e from Dantec was used to generate seeding particles (droplets) from olive oil. The droplet size was not measured, however, should be approximately $\sim 3\,\mu m$ according the Dantec's User manual [18]. Experimental channel together with the settling chamber was placed on three-dimensional traversing system (shown in Fig. 2.6), which allowed precise positioning with 0.02 *mm* resolution in all three axes.

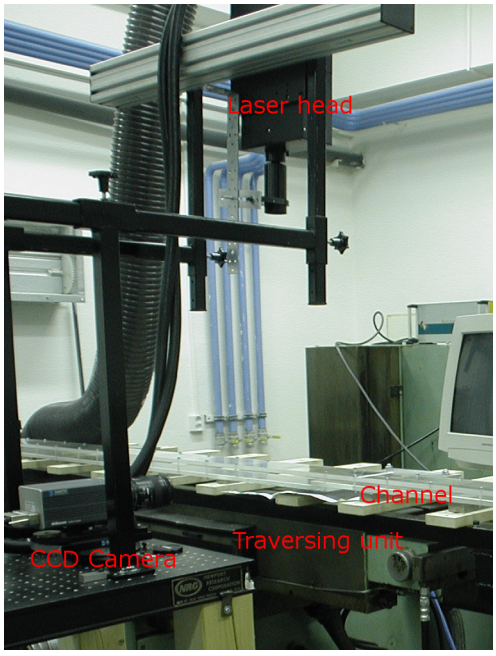

Figure 2.6. Experimental setup in real view.

Laser head was fixed above the channel and the laser optics was aligned parallel to the channel symmetry plane by virtue of calibration pinholes temporary mounted on the channel sidewall. The vertical position of the laser optics over the channel was high enough to create laser sheet of 90 *mm* width and approximately the same intensity. The camera assembly was placed on the table so, that the lens axis was normal to the channel symmetry plane as well as the laser sheet plane. The channel was traversed so, that the laser sheet plane was parallel to the outer side of the channel sidewall, where gauge was glued. The lenses were focused on this gauge and consequently an image was captured in order to calibrate the camera according the gauge. After the calibration the channel was traversed in a starting position, which was chosen so, that the step edge ($x/S = 0$, $y/S = 1$ and $z/S = 0$) was in the center of the focus plane of the camera's field-of-view, i.e., the point in the channel of coordinates $x/S = 0$, $y/S = 1$ and $z/S = 0$ was aligned with a pixel of the camera of indices $639x511$. Figure 2.6 shows the laser head and the camera placement in the laboratory.

The distance of the camera sensor from the laser sheet plane was approximately 450 *mm*, thereby the field-of-view was approximately $49x39$ mm^2, i.e., one pixel represents $d_x \, x \, d_y = 0.0385 \, x \, 0.0385$ mm^2 in the object plane. The pixel size of used CCD camera is $D_x \times D_y = 6.7 \times 6.7$ μm^2, thereby the optical magnification expressed as

$$M = \frac{D_x}{d_x} \tag{2.2.1}$$

was 0.1741. A compromise between the amount of light reflected from surface and amount of light scattered from tracking particles that pass the optics had to be taken, f-number of $f^{\#} = 5.6$ was found to be optimal choice. The depth-of-field corresponding to this f-number was 2 *mm* (according the manufacture's manual [51]).

2.3. Measurement procedure

The backward-facing step flow forms complex flow situation where high velocity gradients occur between the bulk flow and the recirculation flow region. The velocities inside the recirculation flow region are below $0.2 \; U_b$ of the bulk velocity in the mean flow (see [1],

[5], [16], [41] and [49]), what puts high demands on PIV measurement method, particularly the dynamic velocity range. The dynamic velocity range (DVR) is derived as the ratio of maximum measurable velocity to the minimum resolvable velocity [2]

$$DVR = \frac{u_{\max}}{\sigma_u} \tag{2.3.1}$$

where σ_u is the rms error in the velocity measurement and $u_{\max} = \frac{\triangle x_{\max}}{\triangle t}$ is maximum measurable velocity. The dynamic velocity range is given by the digital camera resolution, diameter of particle image prior to being recorded, magnification, f-number and the algorithm used to determine displacement between images.

Maximum measurable velocity is determined by the pulse separation time between two successive light pulses and the size of the interrogation window. Long pulse separation times lead to large particle displacements, i.e., large interrogation window is required to fulfil the 'one-quarter-rule' [36] and increased dynamic velocity range, simultaneously. Unfortunately, long time delay between image pair results in the loss of some information about the motion of the particle, because only initial and final location is recorded but no information about the trajectory between both points is recorded. This is crucial especially for high speed particles. Also particle pair losses become more probable. Large interrogation windows can tolerate much smaller displacement gradients than the small interrogation windows, since the results contain biased data due to the velocity gradients across the interrogation window, which shift the resulting displacement to lower values because the particles with small displacement will be presented more frequently than those with higher displacements [58]. Large interrogation windows yield small dynamic spatial range (DSR) that is defined as the ratio of the largest observable length scale to the smallest observable length scale (typically the interrogation window size)

$$DSR = \frac{l_x}{N_x d_x} \tag{2.3.2}$$

where l_x is lenght of field-of-view, d_x is the pixel size in the object plane and N_x is number of pixels in x-direction within interrogation window. For practical reasons multipass cross-correlation method is used, where the interrogation window size is gradually decreased and

a window offset between the first and the second frame is introduced. This offset is equal to the displacement obtained from the previous step. Practically, the separation time between pulses was chosen so, that the displacement of the fastest particles will be equal to $\frac{D_x\, c_{\max}}{M}$, where D_x is the pixel size of the sensor, $c_{\max}$ is the number of pixels the particle can move and M is the magnification factor. It was assumed that the fastest particles will travel with double the bulk velocity, i.e., $2U_b$, thus the separation time can be calculated as

$$\triangle t = \frac{D_x\, c_{\max}}{M\, 2U_b} \tag{2.3.3}$$

Multipass method with two steps was used. The initial interrogation windows size was $128 \times 64\ px^2$, where the transversal size was half of the streamwise direction, since it was assumed that the transversal velocities are smaller. $c_{\max} = 16$ was set according the 'one-quarter-rule' [36]. After each step the interrogation window was refined to the half of the previous window and central difference scheme was used to offset both interrogation windows. The final interrogation window size was $32 \times 16\ px^2$ with 50% window overlap.

The rms error in velocity measurement in equation 2.3.1 is qiven by relation

$$\sigma_u = \frac{\sigma_{\triangle x}}{\triangle t} = \frac{\sigma_{\triangle X}}{M\, \triangle t} \tag{2.3.4}$$

where $\sigma_{\triangle X}$ is rms displacement error that depends upon the method used to determine the particle image displacement $\triangle X_p$, which Adrian [2] asserts so

$$\sigma_{\triangle X} = c_\tau d_\tau \tag{2.3.5}$$

where c_τ is a constant that depends on the analysis procedure ability to determine the displacement between images and typically is of $1 - 10\%$ of the image diameter (Adrian [2] asserts value $c_\tau = 0.05$). The d_τ is the diameter of the recorded image given by the resolution of the recording medium d_r and the diameter of the optical image prior to being recorded d_e that

$$d_\tau^{\,2} = d_e^{\,2} + d_r^{\,2} \tag{2.3.6}$$

Here $d_r = D_x$ and d_e can be expressed as

$$d_e^{\,2} = d_s^{\,2} + M^2 d_p^{\,2} \tag{2.3.7}$$

where d_p is the particle diameter and d_s is the diffraction limited spot size given by

$$d_s = 2.44(1 + M)f^{\#}\lambda \tag{2.3.8}$$

where λ is the wavelength of the laser light. Diameter of tracking particles d_p was not measured, however, it was assumed that they have the same size distribution as published in Dantec's Manual for the atomizer [18], so value of $3\mu mm$ was substituted for d_p. Since the sampled image diameter d_e should agree with Nyquist's criterion, the lens was slightly defocused [58] so, that the particle image prior to being recorded corresponded to $d_e \geq 2d_r$, what leads to negligible effect of the recording medium resolution on the accuracy of the displacement measurement of the particle image [2]. Equation 2.3.1 can be now expressed as

$$DVR = \frac{M \triangle x_{pmax}}{c_\tau d_\tau} \tag{2.3.9}$$

yields after the substitution $DVR \approx 143$.

To ensure that the acquired data are statistically independent, the sample interval between successive image pairs should be separated by two integral time-scales $2T_1$. Because no autocorrelation measurements to evaluate the integral time-scale T_1 was conducted, the value of integral time-scale had to be estimated using Taylor frozen turbulence hypothesis [13]

$$T_1 = \frac{L}{U_b} \tag{2.3.10}$$

where L is the integral length scale which describes the average size of the large, energy-containing eddies [33]. The unknown integral lenght scale in equation 2.3.10 was estimated as the length of primary recirculation bubble, i.e., the length of reattachment length, thus $L = x_1$. The maximum of the integral time-scale T_1 was found for the case of the highest

aspect ratio $AR = 33.2$ and the lowest investigated Reynolds number $Re = 100$, thereby the integral time-scale was approximately $T_1 = 0.48\ s$ and consequentlly the sample interval $\triangle t = 2T_1 \approx 0.96\ s$ [13]. For practical reasons, the sampling rate of the PIV system

$$SR = \frac{1}{2T_1} \tag{2.3.11}$$

was chosen as the nearest integer value $SR = 1\,Hz$.

It was impossible to cover whole area downstream the step with single field-of-view, since it was approximately only 49 *mm* long. Thus areas where the separation at the step edge, shear layer, reattachment (that takes place almost 200 mm downstream the step edge) and commencing relaxation of the flow occur were observed separately. In order to cover whole area of interest, several measurements sets with increasing distance from the step edge had to be realized. Practically, the distance in the streamwise direction was increased by 40 *mm*, thereby approximately 4.6 *mm* overlap on both sides of each field-of-view was achieved. Each measurement set contains 100 image pairs captured with time separation between successive laser pulses calculated according equation 2.3.3. This was separated into two tasks.

Scanning the symmetry plane. In the first step, measurements at the symmetry plane were performed in order to obtain general information about the reattachment length and the flow situation at the symmetry plane. The procedure was conducted in following steps:

1. The channel was traversed in the starting position, namely the center of the focus plane of the camera´s field-of-view was aligned with the point $x/s = 0, y/S = 1$ and $z/b = 0$.

2. Measurement was initiated and a set of 100 image pairs was captured with time separation between successive laser pulses calculated according equation 2.3.3.

3. The channel was traversed in the streamwise direction by $\triangle x = 40\ mm$, i.e., the streamwise position of the center of the field-of-view was increased by $\triangle x/S = 4$.

4. Steps 2. and 3. were iteratively repeated until the required distance from step edge was reached.

Scanning half of the channel. In the second step, the assumption was taken that the range of Reynolds numbers investigated within this project is low enough that the flow in the downstream section will be symmetric. Thereby only half of the channel was scanned in order to obtain spanwise distribution of reattachment length and secondary recirculation bubble adjacent to the top plane. The scanning was performed in following steps:

1. The measurement begun as in "Scanning the symmetry plane", the steps 1. and 2., i.e., channel was traversed in the starting position and a set of 100 image pairs was acquired.

2. The channel was traversed towards the wall. Near the symmetry plane the spanwise separation between measurements was 10 *mm* for $AR = 33.2$ and 5 *mm* for narrow channels. Near the sidewall the separation was decreased down to 1 *mm*. At each position set of 100 image pairs was acquired.

3. At each position set of 100 image pairs was acquired.

4. When the measurement closest to the sidewall was finished, the channel was traversed back to symmetry plane, i.e., $z/b = 0$.

5. The channel was traversed in the streamwise direction the same way as in the step 4 "Scanning the symmetry plane".

6. Steps 2. through 5. were iteratively repeated until the required area was fully scanned.

Figure 2.7 elucidates locations of individual fields of view when the area downstream the step was scanned as described above. The maximum distance of the field of view center point from the step edge varied from $20S$ to $32S$.

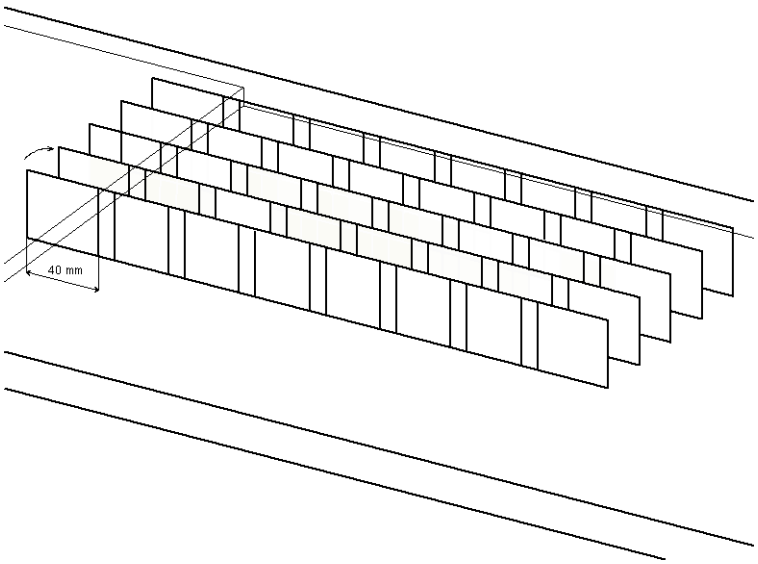

Figure 2.7. Schematical view elucidating locations of individual fields of view when the area downstream the step was scanned.

2.4. Data processing

2.4.1. Pre-processing

Since the field-of-view was larger than the height of channel, part of the top and the bottom wall of the channel was also recorded on the raw PIV images, but removed before image pre-processing. The raw data stored in PIV images were significantly affected by noise, especially pixel blooming produced by intense light reflection from impurities and scratches at the top and bottom walls (see Fig. 2.8) as well as from sidewalls, when the measurements were performed in the vicinity of the sidewall. These scratches on the surface occurred during channel manipulation. The impurities were mainly formed by droplets of seeding particles (here the olive oil), that agglomerated at the channel interior walls. The result of this phenomenon was the occurrence of spurious vectors in the vector field, which biased the results (see Fig. 2.9). Filtration of the data was necessary to reject this vectors before post-processing (Fig. 2.9).

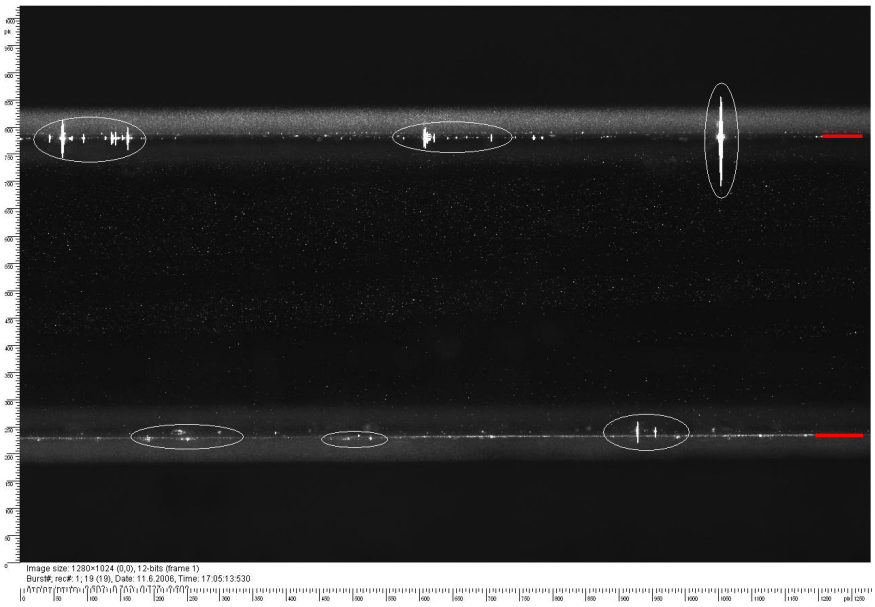

Figure 2.8. Raw image as captured by the CCD camera. The pixel blooming is marked inside ellipses. The interference between plexi-glass and flowing fluid is emphasized on right side of the image with red strips.

Possible way how to reduce the pixel blooming was the use of higher F-number to reduce amount of photons passing lens optics, but this was not found effective, since it also reduced useful signal scattered from the seeding particles. The size of the area affected by the pixel blooming varied within the time and also between both images of the pair, therefore, a simple technique, where background noise is substracted from each image, was inapplicable, since the average image that is substracted from each image pair contains smaller affected areas than is the area of individual images. For this reason simple rejection algorithm was developed, where pixels with greyscale intensity higher than certain threshold value are marked as affected ($I > I_{tres}$) and the intensity is reduced [4]. The drawback of this approach was, that also pixels inside the investigated area were marked, although they didn't represent noise. To remedy this, an improvement of the algorithm was made, where the greyscale intensity of the candidate pixels was compared against average intensity value calculated from the neighbouring pixels.

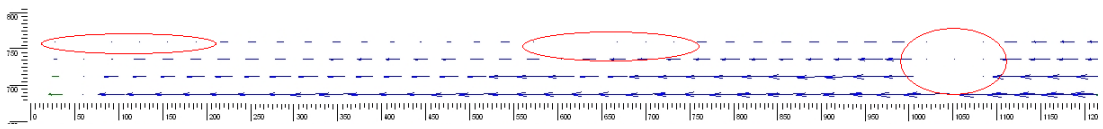

Figure 2.9. Areas where spurious vectors due to pixel blooming were rejected.

2.4.2. PIV calculation

The pre-processed data were subject to PIV cross-correlation calculation Because of the presence of gradients in the flow, a multipass cross-correlation method with gradually decreased window size and offset between the first and the second frame was chosen in order to achieve high dynamic velocity range and to minimise the effect of the velocity gradients. It was used two pass iteration scheme with initial interrogation window size $128x64\ px^2$ and the final interrogation window of $32x16\ px^2$ with 50% overlap. The size of the last interrogation window was $1.232x0.616\ mm^2$ in the object space. The offset between the first and the second image was set according the velocity vector obtained from the previous iteration step. Central difference scheme was used for the offset. No window function was used to remove the edge discontinuity effect. Moving average validation was used as a data validation method to detect spurious vectors. This method validates vectors in comparison with median value of the neighbouring vectors with an acceptance factor 0.1 within 3 iterations. Removed vectors were recovered by applying bilinear interpolation calculated from the four neighbouring vectors.

2.4.3. Post-processing

Each set of vectors field was subject of statistical calculation and calculation of turbulence quantities such:

Average value

$$\overline{u}_i = \frac{\sum_{k=1}^{N} u_i^{(k)}}{N} \tag{2.4.1}$$

where N represents number of vector fields within the set. Index i (and j used later) are similar to Einstein´s notation but reach only values $i, j = 1, 2$.

Fluctuation component

$$u'^{(k)}_i = = u_i^{(k)} - \overline{u}_i \tag{2.4.2}$$

Root mean square values

$$u_{i(rms)} = \sqrt{\frac{\sum_{k=1}^{N} (u'_i{}^{(k)})^2}{N-1}} \tag{2.4.3}$$

Strain rate tensor

$$S_{ij} = \frac{1}{2}\left(\frac{\partial u_i}{\partial x_j} + \frac{\partial u_j}{\partial x_i}\right) \tag{2.4.4}$$

Reynolds stresses

$$\tau'_{ij} = -\bar{\rho}\overline{u'_i u'_j} = -\bar{\rho}\frac{\sum_{k=1}^{N} u_i'^{(k)} u_j'^{(k)}}{N} \tag{2.4.5}$$

Turbulent kinetic energy

$$K = \frac{1}{2}\overline{u'_j u'_j} = \frac{1}{2}\left(\overline{u'^2} + \overline{v'^2}\right) \tag{2.4.6}$$

Turbulence production

$$P_{2D} = -\left[\overline{u'^2}\frac{\partial \bar{u}}{\partial x} + \overline{v'^2}\frac{\partial \bar{v}}{\partial y} + \overline{u'v'}\left(\frac{\partial \bar{u}}{\partial y} + \frac{\partial \bar{v}}{\partial x}\right)\right] \tag{2.4.7}$$

Dissipation

$$-\varepsilon = -\nu\left[2\overline{\left(\frac{\partial u'}{\partial x}\right)^2} + 2\overline{\left(\frac{\partial v'}{\partial y}\right)^2} + \overline{\left(\frac{\partial u'}{\partial y} + \frac{\partial v'}{\partial x}\right)^2}\right] \tag{2.4.8}$$

Consequently, this data were resampled to new grid with resolution $0.5x0.5\ mm^2$ using bilinear interpolation method and than joined together to form single vector/scalar field. In locations where images overlapped each other, the data were obtained as arithmetical average of both overlapping data structures. This way several sheets were created, each contains velocity vector, statistical and turbulence data at same distance from symmetry plane. In following, this sheet is called "Whole Domain Ensemble Average". Finaly, positions of separation and reattachment points were located.

Typical values of transversal velocities in the channel were close to the lower limit of measurable velocity (displacement), so the measured profile was strongly affected (see Fig. 2.10). Reflections near the upper wall also affected the measured velocity profile, where the transversal velocity was not zero near the top wall. The raw measured velocity profile had to be processed in order to obtain smooth profile to calculate the strain rate. Two attempt were made, one using moving average filtering and the second using polynomial interpolation of sixth order, both depicted in Fig. 2.10 together with transversal velocity profile obtained from numerical solution at same location as the experimental one. However, the resulting strain rate profiles (Fig. 2.11) were influenced by the filtering (interpolation) method used. For this reason no data, that are calculated by using derivations will be presented within this work.

2.4.4. Separation and reattachment points detection

Several different methods to detect the location of separation and reattachment points are used depending on the authors preference. Most of the authors ([5], [10], [16], [48], [49], [65] and [67]) define the position of separation or reattachment as a point where where the average streamwise velocity component adjacent to the wall is equal zero:

$$\lim_{\triangle t \to \infty} \frac{1}{\triangle t} \int_{\mathbf{x},t_0}^{\mathbf{x},t_0+\triangle t} U(t)\, dt = 0 \tag{2.4.9}$$

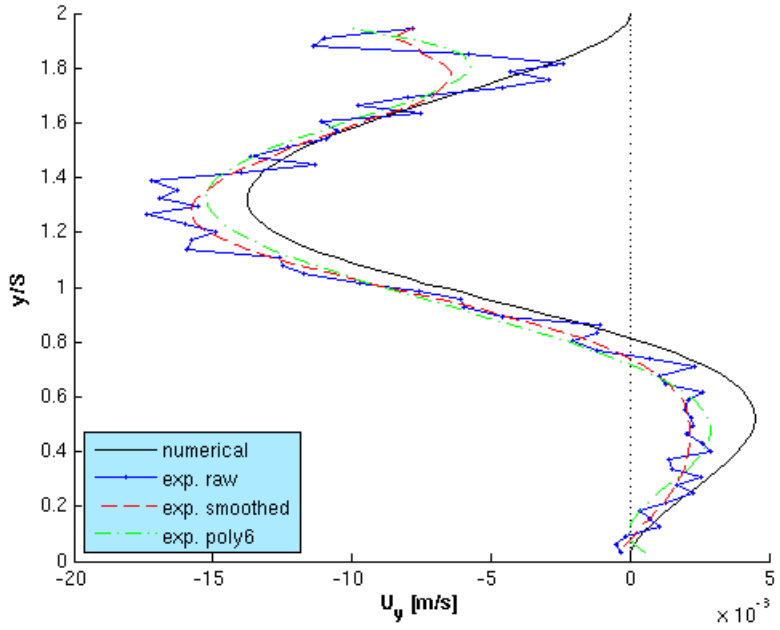

Figure 2.10. Transversal velocity profiles.

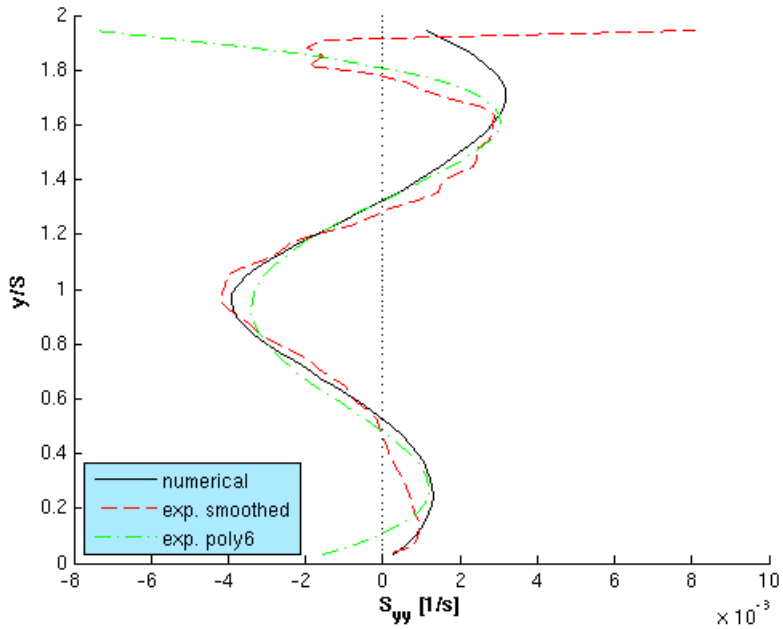

Figure 2.11. Strain rates calculated from transversal velocities presented in Fig. 2.10.

Some authors ([9], [31], [49] and [63]) define reattachment/separation as a point where the skin friction coefficient, respectively, the gradient of streamwise velocity component is equal zero

$$\left(\frac{\partial u}{\partial y}\right)_{y=0} = 0 \tag{2.4.10}$$

Some authors, who published mostly hot wire anemometry measurement results ([30], [42], [52] and [66]), determine the reattachment point by forward flow fraction, γ_p, using flow direction probe:

$$\gamma_p = \frac{T_f}{T} = \frac{N_f}{N} \tag{2.4.11}$$

where T_f is additive time of forward flow and T is total time of observation, respectively, N_f is number of observations of downstream flow and N is total number of realizations.

In the present work two different data processing approaches were applied to locate the position of reattachment/separation.

In the first approach, it was expected that the "whole domain ensemble average" represents time averaged vector field, where all effects such a vortex shedding, which produces different reattachment length in time, will diminish, and noise effects such a surface reflections will be smoothed out. Thereby, this average vector field would have simple profile of streamwise velocity component adjacent to the bottom and the top wall, respectively, where change from positive to negative value indicates separation point and change from negative to positive value indicates reattachment point as shown with blue line in Fig. 2.12. However, the data were still affected by reflections that were projected in the results as sudden changes, as could be seen in Fig. 2.12, especially around $x/S = 3.7$. Filtration of these sudden changes was applied to smooth out the streamwise velocity curve; median filtration over five neighbouring points was used and the result is shown in Fig. 2.12 as red dashed line. Vertical lines in the figure demonstrate individual uncorrelated fields-of-view, since they were recorded at different time (understand that the field-of-view was approx-

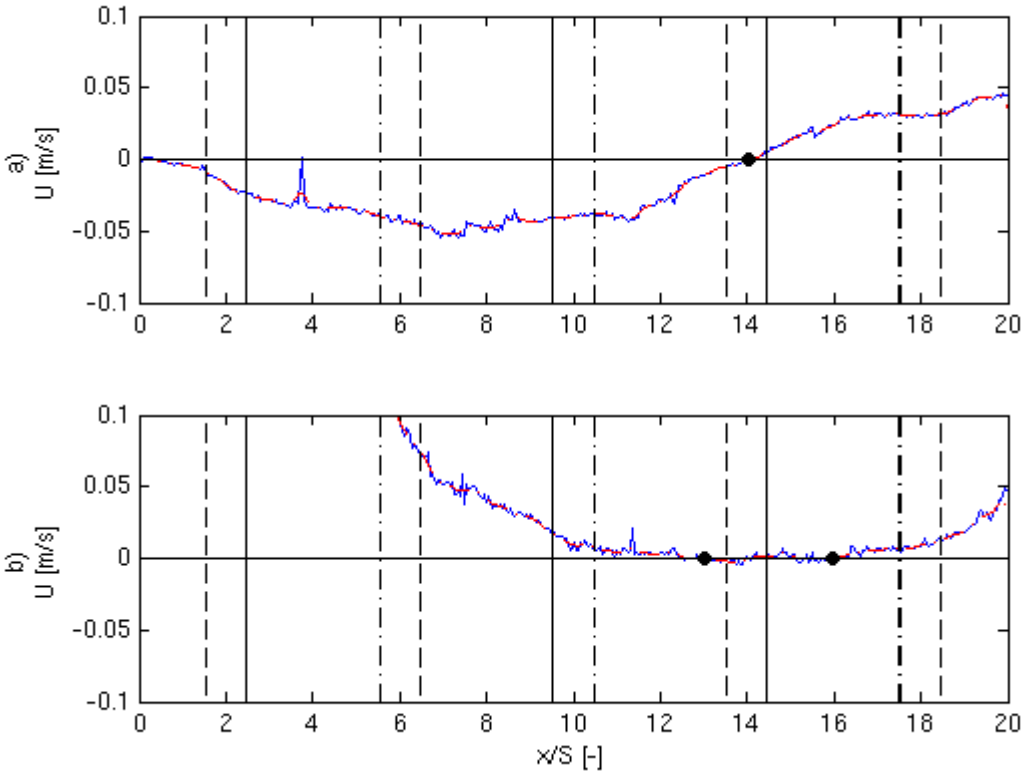

Figure 2.12. Example of separation and reattachment points detection. Streamwise velocity component $AR = 17.2, Re = 991$, a) adjacent to bottom wall $z/b = 0$, b) adjacent to top wall $z/b = 0.3642$.

imately 45*mm* long and thus each data set was acquired at much distant time compared to the delay between individual double frames). An arithmetic average of both vector fields was calculated in the overlap area. Matlab function `sign()` was applied on the smoothed line to locate indexes, where sign of the streamwise velocity component changes due to the presence of separation or reattachment point. This approach represents realisation of equation 2.4.9 and is used in the entire work if not mentioned otherwise.

Since no statistical information can be obtained from the average vector field to provide estimations about the oscillations of the separation/reattachment point around equilibrium position, second approach was utilised, namely the forward flow fraction Eq. 2.4.11. In this case, point where the distribution of forward flow fraction was equal $\gamma_p = 0.5$ was taken as location of reattachment/separation. Furthermore, minimum and maximum reattachment length can be extracted from the distribution of forward flow fraction as points

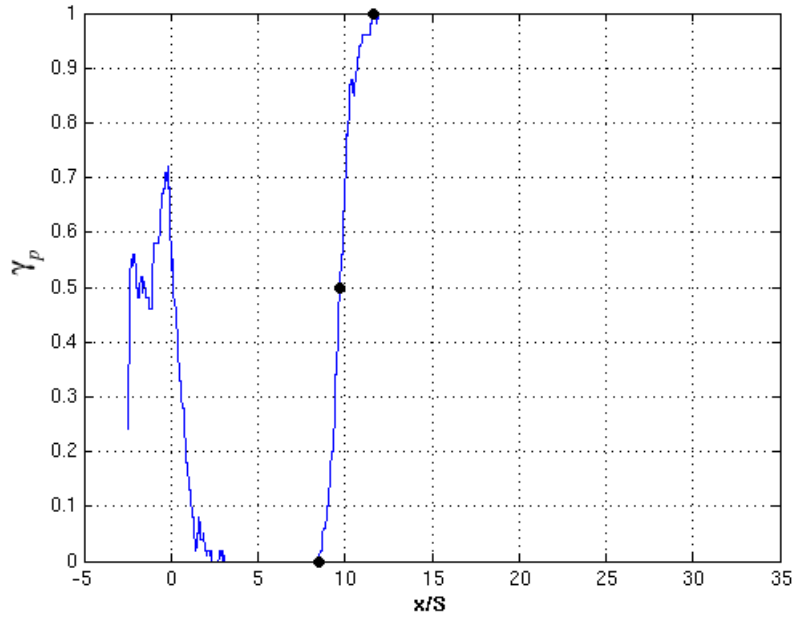

Figure 2.13. Typical distribution of forward flow fraction. Dots mark points where $\gamma_p = 0; 0.5$ and 1 were detected.

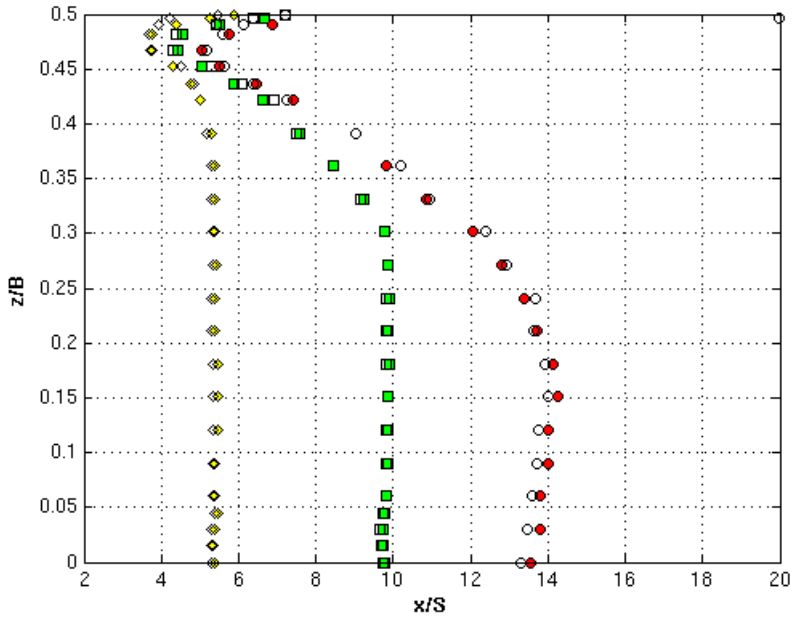

Figure 2.14. Comparision of both detection methods. Full symbols are for method locating the reattachment point in point where average streamwise velocity component is equal zero; empty symbols are for method using forward flow fraction.

where $\gamma_p = 0$ and $\gamma_p = 1$, respectively. Typical distribution of the forward flow fraction is depicted in Fig. 2.13. Results of both methods are compared in Fig. 2.14.

Chapter 3. Numerical simulation

Numerical simulations are next to experimental investigation and analytical solution one of the three main categories applied in engineering research. Analytical solution revealed very early to be capable to describe only simple problems, and failures when facing complexity of turbulent flows that are stochastic and strongly nonlinear. Experimental flow investigation is appreciated for its significance and plays an important role in the validation of numerical solutions. Unfortunately a limited number of flow quantities can be acquired simultaneously. Predominantly single point measurement are achieved with hot wire anemometry (HWA) [13] or Laser-Doppler anemometry (LDA) [3]. The advent in laser technology made significant step in the experimental fluid dynamics enabling concurrent measurements of the flow velocities in the entire plane defined by the laser sheet, as is the case of the two- and three-dimensional particle image velocimetry (PIV) [58], dual-plane stereoscopic particle image velocimetry [58] and very recently tomographic-piv [21]. Despite these advances in measurement techniques, experimental fluid mechanics is still very costly for everyday engineering applications, but serve as necessary validation tool. The popularity of numerical simulations has recently risen altogether with the development of faster computers, making simulation of complex flow cases more economical. Numerical simulations compared to the experimental methods has the advantage being cost effective, flexible method with the capability to provide informations about any flow quantities at any point of the solution domain at any time. Even though these advantages, numerical simulations suffer a major drawback: their inability to guarantee accuracy of turbulent flows under all conditions and thus requiring experimental data for validation.

Fundamental for computational fluid dynamics simulations is the system of Navier-Stokes equations representing conservation of mass, momentum and energy[1].

[1] Here an ambiguity exist, since some literature describes only the momentum conservation equations as the Navier-Stokes equations.

- conservation of mass

$$\frac{\partial \rho}{\partial t} + \frac{\partial (\rho u_i)}{\partial x_i} = 0 \tag{3.1}$$

where $u = (u_1, u_2, u_3)$ is the velocity vector and $x = (x_1, x_2, x_3)$ is the cartesian coordinate.

- conservation of momentum

$$\frac{\partial (\rho u_i)}{\partial t} + \frac{\partial (\rho u_i u_j)}{\partial x_j} = -\frac{\partial p}{\partial x_i} + \frac{\partial \tau_{ij}}{\partial x_j} + f_i \tag{3.2}$$

where stress tensor τ_{ij}[1]

$$\tau_{ij} = \mu \left(\frac{\partial u_i}{\partial x_j} + \frac{\partial u_j}{\partial x_i} - \frac{2}{3}\delta_{ij}\frac{\partial u_k}{\partial x_k} \right) + \zeta \delta_{ij}\frac{\partial u_k}{\partial x_k} \tag{3.3}$$

- conservation of energy

$$\frac{\partial (\rho h)}{\partial t} + \frac{\partial (\rho h u_j)}{\partial x_j} = \frac{\partial p}{\partial t} + u_j \frac{\partial p}{\partial x_j} + \tau_{ij}\frac{\partial u_i}{\partial x_j} - \frac{\partial q_j}{\partial x_j} \tag{3.4}$$

where heat flux q_j is given by Fourier law

$$q_j = -k\frac{\partial T}{\partial x_j} \tag{3.5}$$

[1]Here, τ_{ij} is the stress tensor $[kg^{-1}s^{-2}]$, different from subgrid stress tensor.

They need to be completed with an equation of state and expressions for material properties. Straight solution of these equations is called Direct Numerical Simulation (DNS). Specific for DNS approach is that it solves all scales of the fluid motion ranging from the largest coherent structures to the smallest dissipating eddies without any turbulence modelling or application of any empirical correlation, smoothing and averaging of the solution field. As a cost of resolving all scales, DNS simulation requires very dense computational mesh capable to resolve the smallest dissipative eddies that are generated by inertial forces and dissipated by viscous forces. Thus the grid size has to be smaller or equal than viscously determined Kolmogorov scale which is given as

$$\eta = \left(\frac{\nu^3}{\varepsilon} \right)^{\frac{1}{4}} \tag{3.6}$$

On the other side, the domain has to be large enough to encompass the largest turbulence scales. Required number of grids is proportional $Re^{9/4}$ and rapidly rises with the Reynolds number. Consequently, the time step to fulfil Courant number condition has to be decreased. Only low to moderate Reynolds number DNS solutions up to 10^4 to 10^5 were provided up to now. Despite the computational costs, DNS provides significant contribution in understanding turbulent flow structures that are hard to obtain from experiments.

All these constrain make DNS impractical for engineering applications. In order to reduce the computational costs, an averaging to Navier-Stokes equations was introduced. Classical averaging method, proposed by Reynolds [59], splits instantaneous flow quantities into an ensemble average value and a fluctuation part, and solves governing equations for these ensemble averaged quantities. These equations are called Reynolds Averaged Navier-Stokes equations (RANS), however, new unknown quantities are introduced into these equations and need to be modelled in order to close the system. Several different turbulence models are available, from simple algebraic models [57], two equations models [40], to full Reynolds stress models [28]. The drawback of all turbulence models is their incapability to cover all flow situations. This means that models, which were designed for flow around bodies, will perform poorly when used to calculate channel flow and vice versa. It seems very unlikely that an universal turbulence model will be created.

A compromise between DNS and RANS approaches is represented by Large Eddy Simulation (LES). LES doesn't solve full turbulent scale range as DNS does, but uses a filtration method, where scales larger than the filter size are fully resolved and scales smaller than the filter size are modelled by means of Sub Grid Scale modelling (SGS). The resolved range is still much larger than in the case of RANS simulation. Contribution of small scale turbulence to the resolved flow is small, since most of the energy is contained within large scales that are also responsible for most of the transport of conserved properties. The errors introduced by subgrid models should be small, making LES more accurate than RANS simulations. Together with the development of more powerful computers LES plays more important role in the development process of engineering applications.

In this work DNS was precluded, since the computational time will be enormous with the available resources. RANS approach applying High Re models is not applicable, since it would be impossible to fit the first grid point according to the y^+ requirements of these models (see section 3.5.1). Low-Re models would be good choice, yet the motivation was focused on LES approach, since the experimental part was carried out using PIV technique, which gives information about an average displacement of all particles inside an interrogation window. This means that the information about the fluid movement of scales smaller than the interrogation window is not known, and only the information of scales equal or larger than the interrogation window is obtained, which is very similar to the filtration technique used in LES. Also the available computational resources made LES approach feasible with realistic costs.

3.1. Principles of Large Eddy Simulation

First ideas of LES date back to early 1960's to the work of Smagorinsky [62]. Up to now plenty of works dealing with LES have been published; one of the most comprehensive are books by Sagaut [60] and Garier et. al. [23] The method is based on the theory of Kolmogorov's energy cascade [38] that the small scales are uniform, their contribution to the total energy budget is small compared to the large scales from those they drain energy though a cascade process. Large scales are in LES concept directly simulated, because the large scales contain most of the energy, are responsible for most of the transporting and are

strongly affected by the boundary conditions, while small scales are modelled. Figure 3.1 shows how this approach is realized.
The decomposition is described by following equation:

$$\overline{\phi} = \phi - \phi' \tag{3.1.1}$$

where overbar states for large scales and prime for small scales.

In order to separate large (resolved) and small scales (subgrid-scales), some kind of cut-off length has to be determined. Contrary to RANS approach, where ensemble average is utilized, in LES a filter function performs the cut-off of small scales based on locally weighted average of the flow properties over volume of the fluid. In the filtering process, scales larger than the filter width $\triangle$ are retained in the flow field, while scales smaller than filter width $\triangle$ are modelled by approach of subgrid-scale modelling. In most of the subgrid-scale models the basic filter width is related to the cell side length ($\triangle \approx (\triangle x, \triangle y, \triangle z)$). Often the cell side is the filter width, what practically means that vortices larger than the mesh spacing pass the filter and are fully resolved, while vortices smaller than mesh spacing are wiped out and have to be modelled (see Figure 3.2). Mathematically the cut-off (high-pass) filter is represented in physical space as a convolution product of the flow quantity and convolution kernel $G(x, x', \triangle)$

$$\overline{\phi}(x) = \oint G(\mathbf{x}\,,\ x, \triangle)\, \phi(x)\, dx' \tag{3.1.2}$$

which is large only when x and x' are not far apart and fulfils:

$$\oint G(x, x, \triangle)\, dx' = 1 \tag{3.1.3}$$

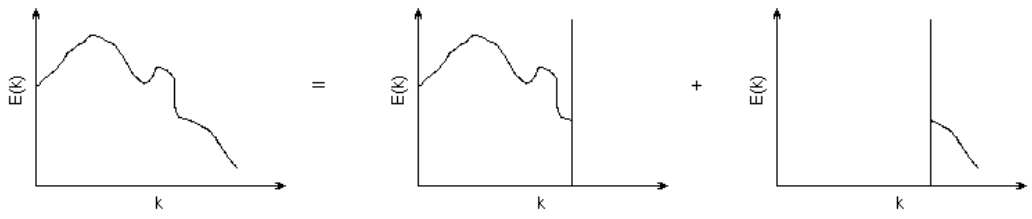

Figure 3.1. Decomposition of energy spectrum in LES.

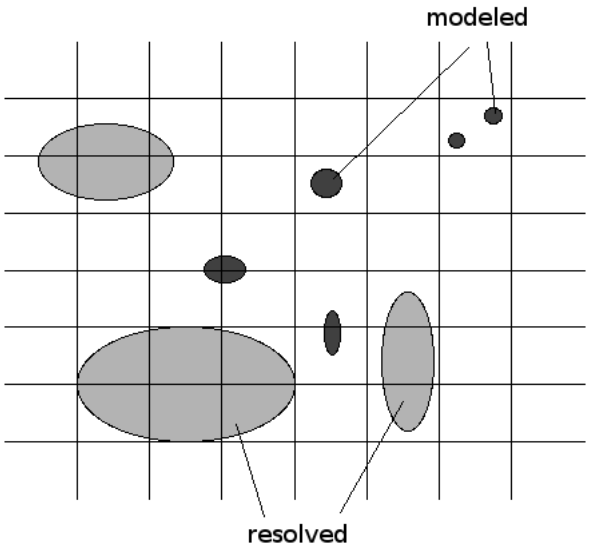

Figure 3.2. Decomposition of energy spectrum in LES.

The most used kernels applied in LES are:

- The Gaussian filter

$$G(x-x,\triangle)=\sqrt{\frac{6}{\pi\triangle^2}}\,e^{-\frac{6|x-x|^2}{\triangle^2}} \tag{3.1.4}$$

- The top-hat filter, which produces simple average over the integration volume. When the filter width is chosen to be equal to the grid spacing, the averaged value and the local value of $\bar{\phi}$ are equal.

$$G(x-x,\triangle)=\begin{cases}\frac{1}{\triangle} & : \quad if \ |x-x|\leq\frac{\triangle}{2}\\ 0 & : \quad otherwise\end{cases} \tag{3.1.5}$$

- The sharp Fourier filter, which is defined in Fourier space as sharp low-pass filter that cuts off all wave numbers above chosen wave number; mostly used in conjunction with spectral methods. The mathematical expression of the filter in Fourier space is:

$$\hat{G}(k, \triangle) = \begin{cases} 1 & : \quad if \ |k| \leq \frac{\pi}{\triangle} \\ 0 & : \quad otherwise \end{cases} \tag{3.1.6}$$

One of the properties of top-hat and Gaussian filters is they smooth both, large and small scale fluctuations, since they are not sharp in Fourier space [64]. On the contrary does the sharp Fourier Filter.

Applying the filtering process to the Navier-Stokes equations, one obtains filtered equations of motion that are at the first sight very similar to the RANS equations. For incompressible flow, we deal here, they state:

$$\frac{\partial \overline{u}_i}{\partial x_i} = 0 \tag{3.1.7}$$

$$\frac{\partial \overline{u}_i}{\partial t} + \frac{\partial (\overline{u_i u_j})}{\partial x_j} = -\frac{1}{\rho}\frac{\partial p}{\partial x_i} + \nu \frac{\partial}{\partial x_j}\left(\frac{\partial \overline{u}_j}{\partial x_i} + \frac{\partial \overline{u}_i}{\partial x_j}\right) \tag{3.1.8}$$

where the non-linear term, $\overline{u_i u_j}$, can be expressed as a function of $\overline{u}_i$ and u'_j according eq. 3.1.1. Applying Leonard's decomposition [44] we obtain the filtered momentum equation in the form:

$$\frac{\partial \overline{u}_i}{\partial t} + \frac{\partial (\overline{u}_i \overline{u}_j)}{\partial x_j} = -\frac{1}{\rho}\frac{\partial \overline{p}}{\partial x_i} + \nu \frac{\partial}{\partial x_j}\left(\frac{\partial \overline{u}_j}{\partial x_i} + \frac{\partial \overline{u}_i}{\partial x_j}\right) - \frac{\partial \tau_{ij}}{\partial x_j} \tag{3.1.9}$$

where the term

$$\tau_{ij} = \overline{u_i u_j} - \overline{u}_i \overline{u}_j = L_{ij} + C_{ij} + R_{ij} \tag{3.1.10}$$

is the subgrid-scale stress and the terms on the right are:

- Leonard term, $L_{ij} = \overline{\overline{u}_i \overline{u}_j} - \overline{u}_i \overline{u}_j$, which represents the interactions between resolved scales to produce subgrid turbulence.

- Cross-stress tensor, $C_{ij} = \overline{\overline{u}_i u_i'} + \overline{u_i' \overline{u}_j}$, which represents the interaction between resolved and unresolved scales
- Reynolds subgrid tensor, $R_{ij} = \overline{u_i' u_j'}$, which represents interaction between subgrid-scales.

Similar to the RANS approach, a closure problem of the eq. 3.1.9 arises, since the filtration technique described ebove, wipes out any information concerning small scales, i.e., the terms u_i' cannot be calculated directly. Subgrid-scale modelling is thus required in order to obtain approximation of the small scales and consider them, in order the dynamics of the resolved scales remain correct.

3.2. Subgrid-scale models

The subgrid-scale modelling has to solve two problems:

1. At each point of the domain it has to determine if there are in space and time, any smaller scales than those established by the filter technique. This requires additional information, either derived from knowledge of fluid mechanics, or by introducing new unknowns, such as kinetic energy, for example.
2. Interaction between subgrid-scales and resolved scales have to be reflected, since the quality of the simulation depends on the fidelity of this reflection.

Interactions between the large and small scales have to reflect two mechanisms, a forward energy cascade and a backward energy cascade. The forward energy cascade, proportional to $k^{-5/3}$, represents energy drain from the large scales by small scale. The backward energy cascade, proportional to k^4, represents the energy return to the resolved scales. This feedback of energy is weaker than the case of forward energy cascade. Some subgrid-scale models based on the assumption of local isotropy will be introduced in this section. For more comprehensive survey, the reader may refer to Sagaut [60].

Models based on the assumption of local isotropy assume, that the filter cutoff frequency is located far into the inertial range[1]. Similar to Boussinesqs approximation in RANS approach, also in LES the deviatoric part of the subgrid-scale stress tensor is proportional to rate of strain of the resolved scales

$$\overline{\mathbf{S}} = \overline{S}_{ij} = \frac{1}{2}\left(\frac{\partial u_i}{\partial x_j} + \frac{\partial u_j}{\partial x_i}\right) \tag{3.2.1}$$

$$\tau_{ij}^{d} = \tau_{ij} - \frac{1}{3}\tau_{kk}\delta_{ij} = -\nu_{sgs}\left(\frac{\partial u_i}{\partial x_j} + \frac{\partial u_j}{\partial x_i}\right) = -2\nu_{sgs}\overline{S_{ij}} \tag{3.2.2}$$

where the isotropic part of the stress tensor, $\frac{1}{3}\tau_{kk}\delta_{ij}$, is added to the filtered static pressure term and requires no additional modelling. The subgrid-scale eddy-viscosity, ν_{sgs}, introduced here, is not property of the fluid but is property of the flow.

3.2.1. Models based on the resolved scales

This model family is based on the hypothesis of local equilibrium of small scales that the flow is in constant spectral equilibria, energy is not accumulated at any frequency and all the energy received from the resolved scales is dissipated entirely.

$$\langle \varepsilon_I \rangle = \langle \tilde{\varepsilon} \rangle = \langle \varepsilon \rangle \tag{3.2.3}$$

where the rate of injected energy is denoted ε_I, transfer rate through the cutoff at wave number k_c, is denoted $\tilde{\varepsilon}$ and the dissipation range is denoted ε, see Fig. 3.3.

First model derived according this hypothesis was the Smagorinsky model [62]. This model is expressed:

$$\nu_{sgs}(\mathbf{x}, t) = (C_s \overline{\triangle})^2 \left(2\left|\overline{S}(\mathbf{x}, t)\right|^2\right)^{\frac{1}{2}} \tag{3.2.4}$$

[1]Chapman [14], estimating the resolved scales should form 80% to 90% of the total kinetic energy.

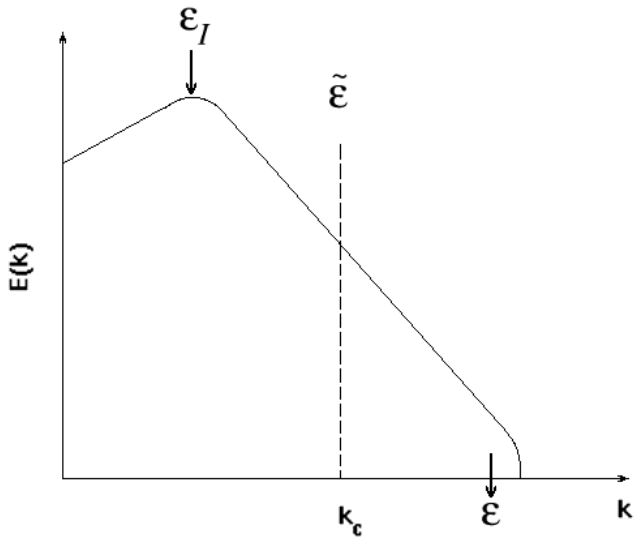

Figure 3.3. Dynamics of the kinetic energy in the spectral space

The constant C_s, the Smagorinsky constant, was theoretically determined from isotropic turbulence decay and ranges between 0.18 and 0.23 [19]. The deficiency of this model is that the subgrid viscousity is non-zero for flows with spatial variations, even in the case of laminar flow or when all scales are resolved. Also shear regions sustain excessive dissipation caused by high $\overline{\mathbf{S}}$. In such situations, the Smagorinsky constant has to be decreased $C_s \simeq 0.1 - 0.12$ [60].

3.2.2. Models based on the subgrid-scales

The physical inconsistency of models based on resolved scales, where they produce non-zero subgrid viscosity as mentioned above, led to development of models that use additional information directly related to the subgrid-scales. Here the subgrid viscosity depends on one or more of the subgrid turbulence characteristics, obtained from additional transport equation of this quantity. Since this models contain more information about the subgrid-scales than the previous model family, they should theoretically give better results when solving problems with large scale intermittency and in the cases of non-equilibrium, such are in free shear layers, separating and reattaching boundary layers. The subgrid viscosity is expressed:

$$\langle \nu_{sgs} \rangle = \langle \nu_{sgs} \rangle (\overline{\triangle}, \langle q^2_{sgs} \rangle, \langle \varepsilon \rangle) \tag{3.2.5}$$

where q^2_{sgs} is the kinetic energy of subgrid-scales and ε, the kinetic energy dissipation rate. One form of the model based on subgrid-scales was developed by Yoshizawa [68]:

$$\nu_{sgs}(\mathbf{x}, t) = C_k \overline{\triangle} \sqrt{q^2_{sgs}(\mathbf{x}, t)} \tag{3.2.6}$$

where the kinetic energy of subgrid-scales, q^2_{sgs}, is obtained by solving transport equation of the form:

$$\frac{\partial q^2_{sgs}}{\partial t} + \frac{\partial \overline{u}_j q^2_{sgs}}{\partial x_j} = -\tau_{ij} \overline{S}_{ij} + \nu \frac{\partial^2 q^2_{sgs}}{\partial x_j \partial x_j} + \frac{\partial}{\partial x_j} \left(\nu_{sgs} \frac{\partial q^2_{sgs}}{\partial x_j} \right) - \varepsilon \tag{3.2.7}$$

where the dissipation term is

$$\varepsilon = C_\varepsilon \frac{(q^2_{sgs})^{3/2}}{\overline{\triangle}} \tag{3.2.8}$$

The value of constants in equations 3.2.7 and 3.2.8 were proposed by Yoshizawa [68] to be $C_k = 0.1$ and $C_\varepsilon = 1$.

3.2.3. Dynamic models

The above described models yield good results as long as the flow characteristics correspond to the hypothesis, they are derived from. This is the case of homogenous turbulent flows, and that the cutoff filter is located far into the inertial range of the spectrum. In other cases, where the flow characteristics differ from the hypothesis on which the models are based on, as in highly under-resolved flows, highly anisotropic flows, transitional flows, or those in high energetical disbalance, the performance of the subgrid models is crippled, because the models are flawed.

Several techniques were developed to improve the simulation results by modification of the subgrid model to adapt it better to the local flow characteristics and remedy the drawbacks of the original forms. One of these approaches is a dynamic procedure for

computing subgrid model constants. First model was proposed by Germano et al. [24]. The idea of this procedure is that the model constant (the Smagorinsky constant for example) is automatically adjusted at each point and at each time step, thus this constant becomes time- and space-dependent: $C_s \rightarrow C_s(\mathbf{x}, t)$. This adjustions are based on Germano identity [25] and is written as:

$$L_{ij} = T_{ij} - \tilde{\tau}_{ij} \tag{3.2.9}$$

where

$$\tau_{ij} = \overline{u_i u_j} - \overline{u}_i \overline{u}_j \tag{3.2.10}$$

$$\mathrm{T}_{ij} = \widetilde{\overline{u_i u_j}} - \widetilde{\overline{u}}_i \widetilde{\overline{u}}_j \tag{3.2.11}$$

$$L_{ij} = \widetilde{\overline{u_i u_j}} - \widetilde{\overline{u}}_i \widetilde{\overline{u}}_j \tag{3.2.12}$$

where the tilde symbol, $\widetilde{\ }$, designates the test filter with width larger than the first filter width $\widetilde{\overline{\triangle}} > \overline{\triangle}$. Typicaly $\widetilde{\overline{\triangle}} \approx 2\ \overline{\triangle}$ is chosen. The tensor, τ_{ij}, is the subgrid stress tensor corresponding to the first filter with the width $\overline{\triangle}$ and the tensor, T_{ij}, is the subgrid stress tensor corresponding to the test filter. The Leonard stress tensor, L_{ij}, consists only resolved scales and can thus be directly calculated.

Now we assume that both subgrid stress tensors, T_{ij} and τ_{ij}, can be modelled with the same constant C_d:

$$\tau_{ij} - \frac{1}{3}\tau_{kk}\delta_{ij} = C_d \beta_{ij} \tag{3.2.13}$$

$$\mathrm{T}_{ij} - \frac{1}{3}\mathrm{T}_{kk}\delta_{ij} = C_d \alpha_{ij} \tag{3.2.14}$$

where the tensors α_{ij} and β_{ij} represent subgrid model deprived of its constant and with all terms calculated with respect to the appropriate filter level (eq. 3.2.4 and eq. 3.2.6, for example). For the Leonard stres tensor L_{ij} we get

$$L_{ij} - \frac{1}{3}L_{kk}\delta_{ij} = C_d \alpha_{ij} - \widetilde{C_d \beta}_{ij} \tag{3.2.15}$$

With the followin approximation:

$$\widetilde{C_d \beta}_{ij} = C_d \tilde{\beta}_{ij} \tag{3.2.16}$$

we get:

$$L_{ij}^{d} = C_{d}\alpha_{ij} - C_{d}\tilde{\beta}_{ij} \tag{3.2.17}$$

This leads to system of six independent equations for the residual, E_{ij}

$$E_{ij} = L_{ij}^{d} - C_{d}m_{ij} \tag{3.2.18}$$

where L_{ij}^{d} denotes the deviatoric of tensor, L_{ij}, and

$$m_{ij} = \alpha_{ij} - \widetilde{\beta_{ij}} \tag{3.2.19}$$

Solution of eq. 3.2.18 will yield six values of the constant C_{d}. In order to remedy this problem, Lilly [45] proposed a leas-square method to calculate the constant C_{d}, thus the problem now becomes:

$$\frac{\partial E_{ij} : E_{ij}}{\partial C_{d}} = 0 \tag{3.2.20}$$

respectively

$$C_{d} = \frac{m_{ij} : L_{ij}^{d}}{m_{kl} : m_{kl}} \tag{3.2.21}$$

The constant C_{d} computed this way has following properties:

– It can take negative values and thus the model can have an anti-dissipative effect locally. This is often interpreted as modelling of the backward energy cascade mechanism.

– It can show very sharp fluctuations, since the denominator can cancel out.

Both above mentioned properties can potentially lead to numerical instability of the simulation. Numerical test have shown that the constant C_{d} can remain negative over long

time intervals [60]. A special treatment is required to avoid excessive fluctuations in the model constant and to ensure model stability. Several different ways performing treatment of the constant were proposed:

- *Averaging over homogenous directions*

  Here a statistical average over homogenous directions is calculated in two ways: first the denominator and numerator average is calculated separately:

$$C_d = \frac{\langle m_{ij} : L_{ij}^d \rangle}{\langle m_{kl} : m_{kl} \rangle} \tag{3.2.22}$$

  or by averaging the constant itself

$$C_d = \left\langle \frac{m_{ij} : L_{ij}^d}{\langle m_{kl} : m_{kl} \rangle} \right\rangle \tag{3.2.23}$$

  Despite this regulation, the constant can still take negative values and requires additional treatment, so-called clipping. The clipping process consists in a limitation of the solution thus the following conditions are ensured:

$$\nu + \nu_{sgs} \geq 0 \tag{3.2.24}$$

$$C_d \leq C_{\max} \tag{3.2.25}$$

  The drawback of this technique appears in complex geometries, which are totally inhomogeneous.

- *Lagrangian dynamic procedure*

  This approach overcomes the problem of averaging in homogenous directions in the case of complex geometries in that the average is calculated along the fluid particle trajectory.

- *Constrained localized dynamic procedure*
  Ghosal et al. [26] proposed method based on the idea of integral formulation of the identity eq. 3.2.9 that removes the mathematical inconsistency of previous formulations. In order to remove the instability problem, the constant is constrained to remain positive. Solution of integral equation results in increased computational time.

- *Approximate localized dynamic procedure*
  Piomelli and Liu [55] suggested method based on a time extrapolation of the constant C_d in the second term on the right of eq. 3.2.15. This results in fully local, and the computational cost compared to Constrained localized dynamic procedure is reduced. However, the clipping of the constant is still necessary.

3.3. Wall treatment

The dynamics and kinematics of the boundary layer is formed by complex interactions between coherent structures. These interactions are highly anisotropic, responsible for intense small scale dissipations in the buffer region. The backward energy cascade is associated with turbulent energy production at small scales, whose maximum is observed at $y^+ = 15$ [60]. These factors require special treatment for solid walls. There are two possible approaches:

– **Directly resolved near-wall dynamics.** Sufficiently fine resolution is necessary to follow all mechanisms in the boundary layer, since the subgrid modelling is incapable to capture them. No-slip condition is than applied on the solid wall. The distance of the first grid point should be smaller than the characteristic scales of the motion in boundary layer. In practice, the first point should lie within ($0 \leq y^+ \leq 1$). However, larger values are referenced in the literature [60].

– **Modeling the near-wall dynamics.** A so called wall model is used to represent the dynamics in the inner zone of the boundary layer. The distance of the first grid point is expected to be larger than the characteristic scales of the motion. The no-slip condition on the wall is removed and the wall shear stress is calculated as a function

of the local velocity at the first grid point, which can be placed in the logarithmic layer ($30 \leq y^+ \leq 200$).

Here, no description about the various wall models will be introduced, since the first grid point of the mesh used within this work was capable directly resolve the near-wall dynamics.

3.4. Inlet condition treatment

Inlet boundary condition is another crucial issue for large eddy simulation as well as direct numerical simulation. Improper representation of the inflow, when this is not fully known, can be source of error of the simulation. The correlation between the inflow specification and the flow conditions in the interior vary from case to case. Several inflow boundary condition generation techniques were developed:

– **Random noise.** This is the simplest method, where random fluctuations are superimposed on the mean inlet velocity profile. However, these fluctuations don't correspond with the real turbulence structure and are rapidly dumped out [19].

– **Precursor simulation**, where the simulation is divided into two parts. Firstly, the inlet velocity profile is obtained from separate simulation of the upstream section, and this is than applied as the inlet condition for the final simulation Figure 3.4 a). Two approaches are possible. The first requires sufficiently long time series of the upstream flow to provide inlet condition for the final simulation. This is the simplest way, but also the most resource expensive. The second approach involves technique of repeatedly re-used similar but much shorter data set. Several treatment techniques are necessary to remedy the periodicity problem induced by small data set used.

– **Mapped inlet.** This method estimates the inlet velocity profile based on information extracted from a plane downstream in the solution domain, as illustrated in Figure 3.4 b). Scaling to the data is applied to enforce specified bulk flow rate as well as to involve the boundary layer growth. This technique represents simple, resource sparing method, since no pre-calculation is performed and the mapped section is part

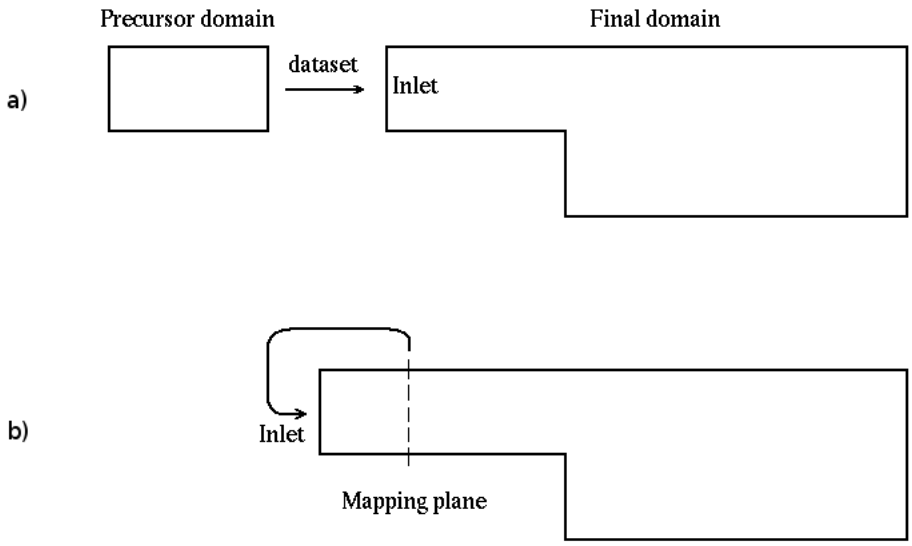

Figure 3.4. Different approaches of treatment of the inlet boundary condition.

of the simulation domain. However, attention has to be taken in the case, where disturbances can propagate upstream towards the mapping plane, eventually contaminate the inlet condition and leading to a feedback effect that can amplify the original disturbance which is again mapped to the inlet. This can be overcome by placing the mapping plane far upstream from any source of large disturbances in the main domain.

3.5. Present numerical model

Numerical simulation was performed in *OpenFoam*, an open source CFD toolbox freely distributed under General Public License (GPL). This C++ library stems from *FOAM*, originally developed at Imperial College in London. It features wide spectrum of solvers for various fluid dynamics problems including laminar flows, turbulent flows, both incompressible and compressible solvers, multiphase flows, bubble flows, magneto hydrodynamics etc. Most of the important, recently published turbulence and subgrid models are included. Features like parallel computing together with increasing computational power today´s computers and their decreasing price, make this toolbox more and more popular in commercial

area, since no additional licensing cost are needed. Here, the last version 1.6 was operated on computers in Czech METACenter.

3.5.1. Mesh

The mesh for the simulation was created by *blockMesh* tool with hexagonal grid. The domain was 10 step heights long in the upstream section and 50 step heights long in the downstream section. No symmetry condition was applied and thus full geometry was solved. The grid spacing was chosen so, that first grid point position was around $y^+ \approx 1$. Estimation was made based on the presumption that the flow in the inlet section is laminar and assuming that the velocity profile at the symmetry section is similar to Poiseuille flow between parallel plates:

$$U(y) = \frac{i}{2\mu}(y\,h - y^2) \tag{3.5.1}$$

where i is calculated from bulk velocity at the inlet section

$$U_b = \frac{12\mu}{h^2} \tag{3.5.2}$$

$$U_b = \frac{\nu\,Re}{d_h} \tag{3.5.3}$$

where d_h is the hydraulic ratio. The wall friction velocity is defined as

$$u_\tau = \sqrt{\frac{\tau_w}{\rho}} \tag{3.5.4}$$

where the wall shear stress τ_w

$$\tau_w = \mu\frac{\partial U_w}{\partial y} \tag{3.5.5}$$

and the dimensionless wall distance, y^+

$$y^+ = y\frac{u_\tau}{\nu} \tag{3.5.6}$$

this gives $y = 1.5182\ 10^{-4}\ m$ for the distance of the first grid point from the wall when $y^+ = 1$ and the highest Reynolds number.

In practice, the downstream cross section was divided into eight same sections as depicted on Figure 3.5. Similarly, the upstream section was divided into four same quadrants. Each segment was vertically divided into 20 cells with simple grading with ratio $\frac{\delta_m}{\delta_w} = 2$, where δ_w is the vertical size (height) of the first cell adjacent to the wall and δ_m is the vertical size (height) of the cell adjacent to the vertical middle of the upstream section (respectively, to the middle of upper and lower half of the downstream section). The number of cells in the horizontal direction was adjusted according the channel width. Simple grading with ratio $\frac{\delta_m}{\delta_w} = 4$, where δ_w and δ_m are horizontal size (width) of cells adjacent to the wall and adjacent to the middle, respectively.

In the streamwise direction, the mesh density was higher near the step edge and less dense near the inlet boundary and exit boundary of the computational domain. Simple grading with ratio $\frac{\delta_m}{\delta_w} = 4$ was applied in both sections (upstream and downstream), where δ_w is the streamwise cell size near the step edge and δ_m is the streamwise cell size near the inlet boundary and exit boundary, respectively.

The number of cells and the distance of the first grid point from the wall is mentioned in Table 3.1. As illustrated in Table 3.1, the first grid point is located approximatelly $y^+ \approx 1$ from the wall. However, the distance between first grid raw and sidewalls was larger than $y^+ = 1$, probably requiring higher number of cells in the z direction or refinement near the walls. Mesh topology at the symmetry plane is ilustrated on Fig. 3.6.

AR	N_x^u	N_x^d	N_y^u	N_y^d	N_z	$\triangle y_y^+$	$\triangle y_z^+$
5.3					70	1.139	2.251
17.3	75	250	40	80	120	1.073	4.099
32.2					240	1.059	3.909

Table 3.1. Present computational mesh. N_x, N_y and N_z stay for number of cells in the x, y and z direction, respectively. The upper indices u and d stay for upstream and downstream section, respectively. $\triangle y_y^+$ and $\triangle y_z^+$ represent distance of the first grid point from the wall in respective direction.

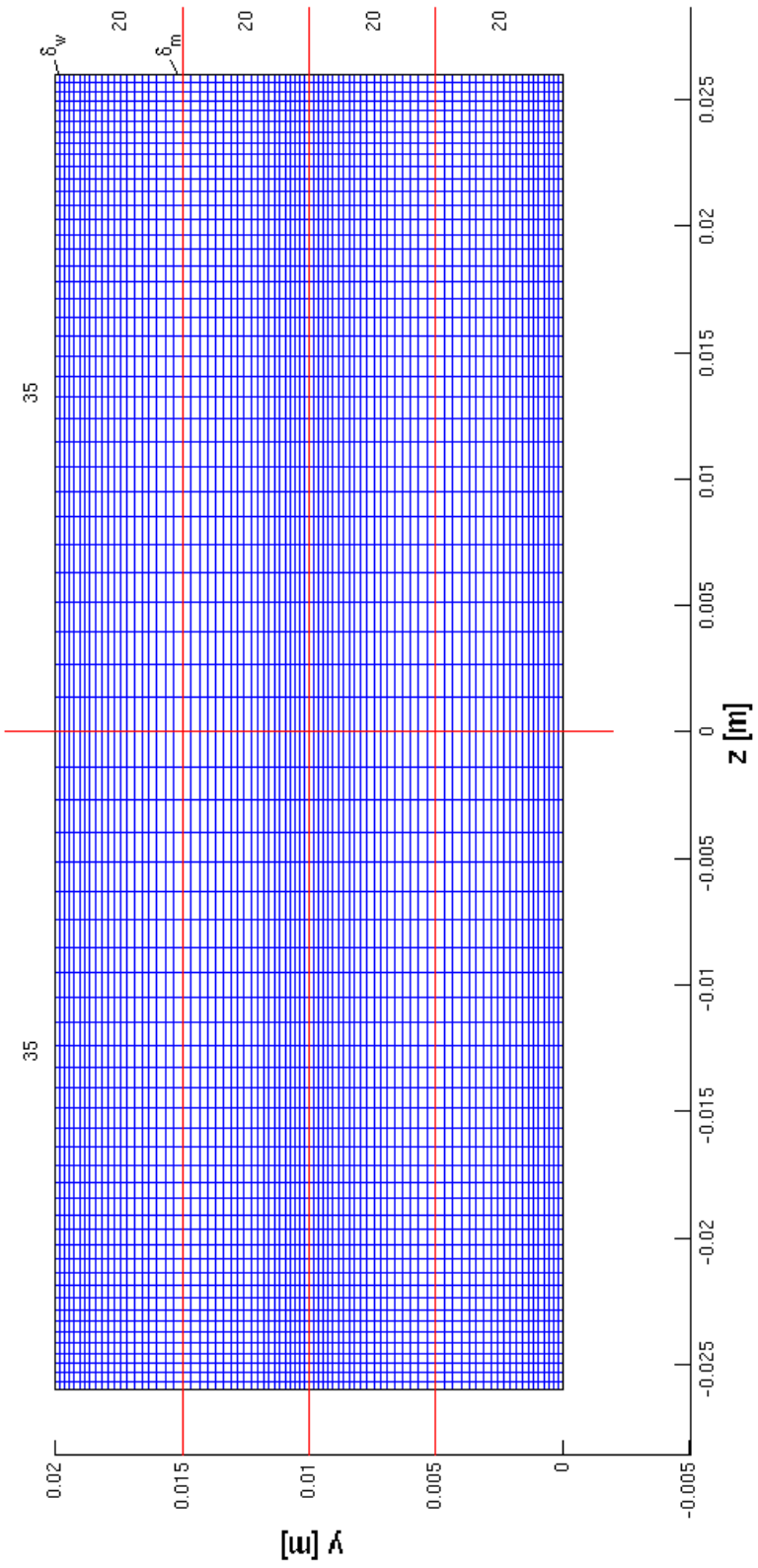

Figure 3.5. Cross section view of the mesh in the downstream section for $AR = 5.3$. Red lines represent the dividing line between sections.

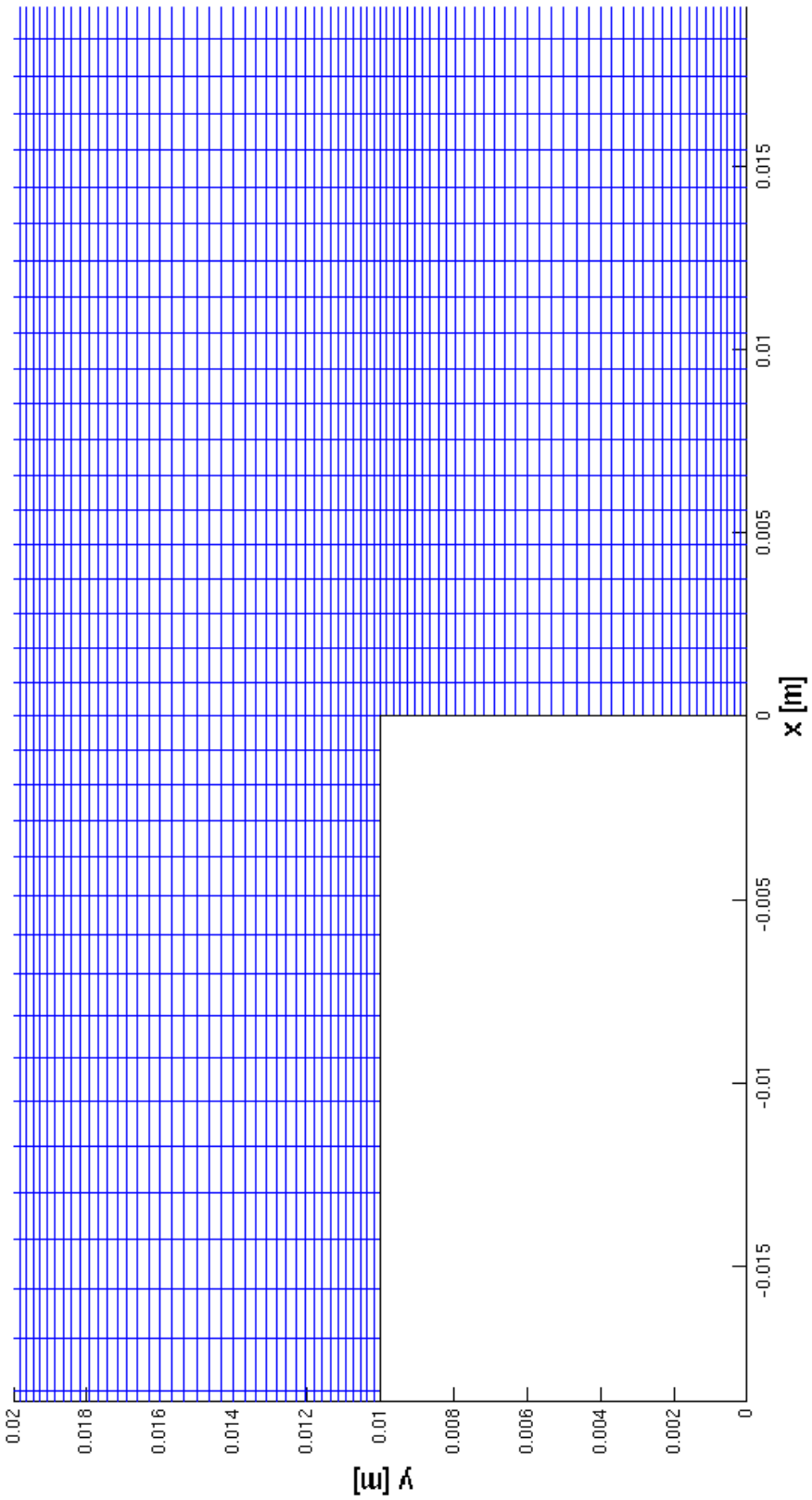

Figure 3.6. Detail of mesh topology at the symmetry plane near the step.

The application of wall models describing the wall dynamics expects that the first grid point is placed in the logarithmic layer ($30 \leq y^+ \leq 200$). If we introduce the lower limit to Eq. 3.5.6, we get the distance of first grid point from the wall to be $0.0046\ m$ for the highest Reynolds number. For lower Reynolds numbers, the distance is even larger. Simple comparison with the height of the upstream section of the channel gives only two cells per the height, certainly insufficient for LES.

3.5.2. Boundary conditions

Mapped inlet was used in this project. The mapping plane was placed $5S$ downstream from the inlet, i.e., at $x/S = -5$. In order to obtain velocity profile that matched with the required Reynolds number, an average (bulk) velocity condition was imposed at the inlet, where bulk velocity is calculated from Eq. 3.5.3. Zero velocity at walls was set, and zero velocity gradient normal to the outlet plane was applied at the exit.

A condition of the type zero pressure gradient normal to the plane was applied at the inlet plane and at walls, while at the exit plane constant zero pressure was set.

3.5.3. Simulation

Smagorinsky model with dynamic adjustment of the constant was used throughout this project. The time step of each calculation was set so, that the Courant number condition $CFL < 1$ was satisfied at each cell of the computational domain, where $CFL = \frac{\mathbf{U}\triangle t}{\triangle \mathbf{x}}$. Approximately $8\,s$ of the flow time were necessary to initialize the flow inside the domain, as illustrated on Figure 3.7, where the development history of the U_x and U_y velocity components near the exit plane is charted. After initialization phase, average of the flow quantities was calculated over $4\ s$ of the flow time.

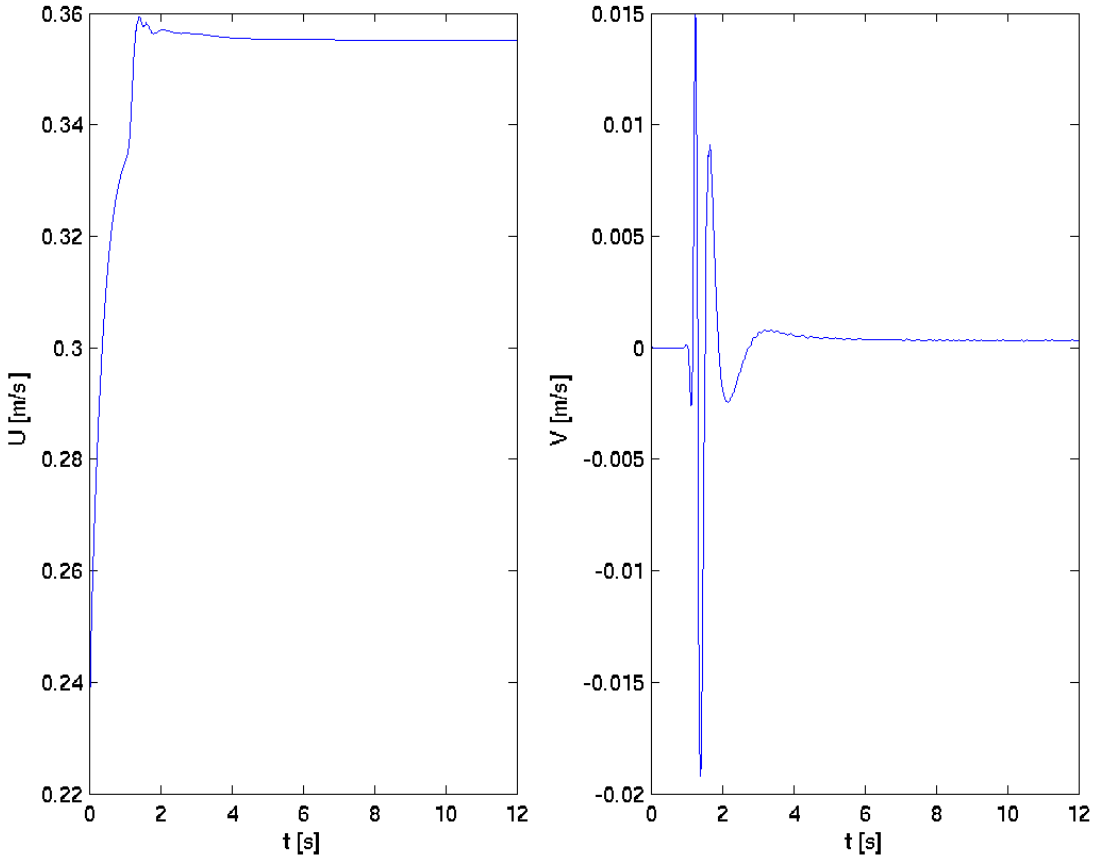

Figure 3.7. Time history of U_x (left) and U_y (right) velocity components at $x/S = 49.5$, $y/S = 1$ and $z/S = 0$.

3.6. Post processing

Mean velocities inside the simulation domain were calculated as already described in Section 2.4.3, in order to compare these results with experimental data. Separation and reattachment points were detected according Eq. 2.4.9, in order to use the same method as used for experimental data.

The detection of a vortex was done by method proposed by Jeong and Hussain [29] referred as Lambda2 method. They rejected pressure minimum as a general detection criterion for a vortex core, since two effects: unsteady straining, which can create a pressure minimum without presence of vortical motion, and viscous effects, which can eliminate

the pressure minimum in a flow with vortical motion. To remedy this, they decompose velocity gradient tensor into its symmetric part, the strain rate tensor

$$S_{ij} = \frac{1}{2}\left(\frac{\partial u_i}{\partial x_j} + \frac{\partial u_j}{\partial x_i}\right)$$

and antisymmetric part, the rate of rotation tensor

$$\Omega_{ij} = \frac{1}{2}\left(\frac{\partial u_i}{\partial x_j} - \frac{\partial u_j}{\partial x_i}\right)$$

They derived the following equation

$$S_{ik}S_{kj} + \Omega_{ik}\Omega_{kj} = \left(-\frac{1}{\rho}\frac{\partial^2 p}{\partial x_i \partial x_j}\right) \tag{3.6.1}$$

which is interpreted in a way, that only tensor $S^2 + \Omega^2$ is able to determine the existence of a local pressure minimum due to vortical motion and defines a vortex core as a connected region with two negative eigenvalues of $S^2 + \Omega^2$. Because $S^2 + \Omega^2$ is real and symmetric, it has only real eigenvalues, λ_1, λ_2 and λ_3 and $\lambda_1 \geq \lambda_2 \geq \lambda_3$, then the point where $\lambda_2 < 0$ belongs to a vortex core. This method overcomes other methods in most of the situations as the authors demonstrated, however, in situations where several vortices exist, it can be difficult for this method to distinguish between individual vortices [32].

Visualisation of all regions complying the $\lambda_2 < 0$ condition can produce vortex map that is hard to read (see Fig. 3.8). A more negative value of λ_2 can be chosen, in order to distinguish a stronger vortical region [11] and to overcome the fuzziness when the isosurfaces at $\lambda_2 = 0$ are mapped; see same situation as in Fig. 3.8 when $\lambda_2 = -400$ (Fig. 3.9) Visualisation was performed in open source visualisation program ParaView version 3.8.0-RC1.

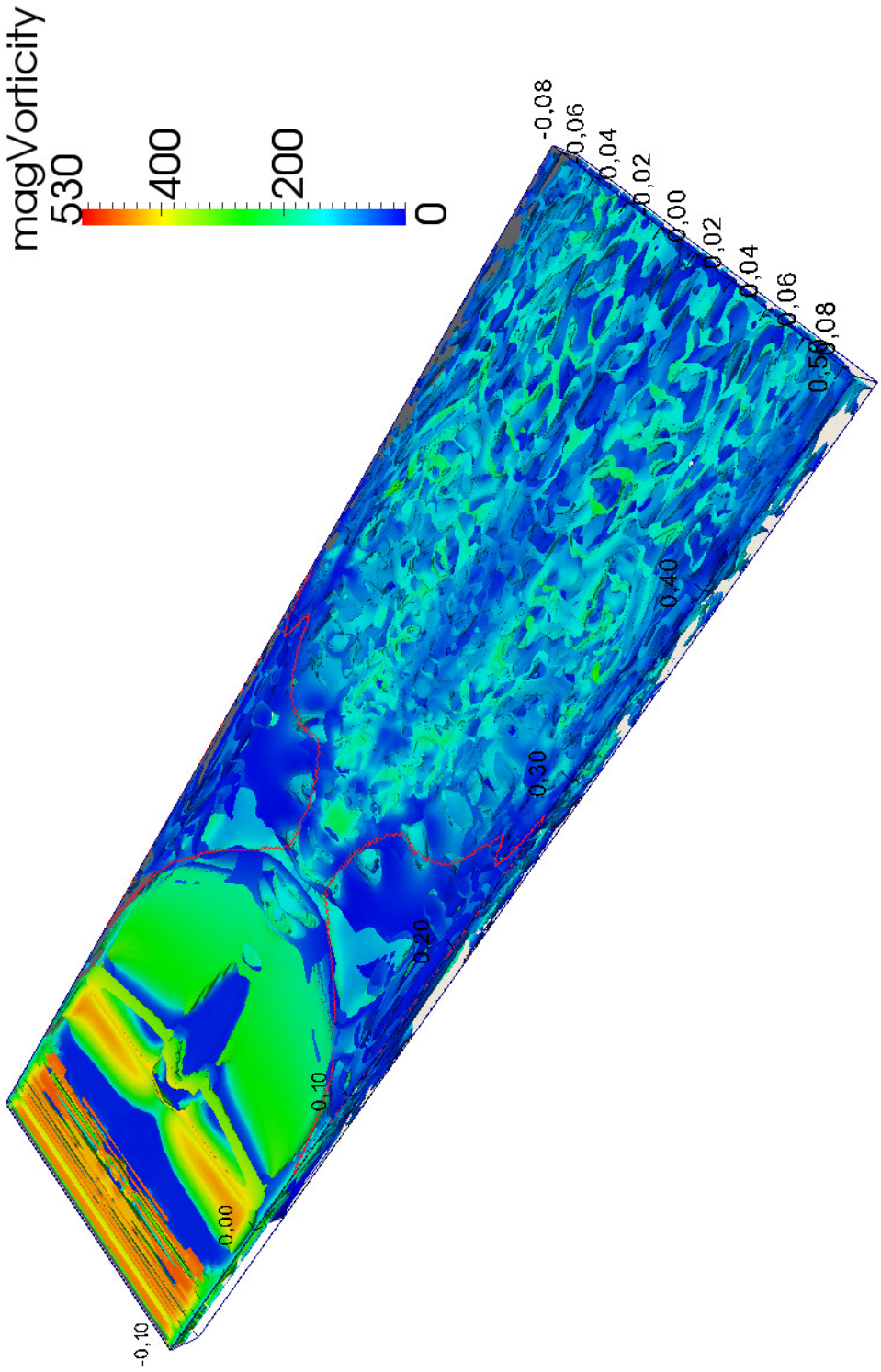

Figure 3.8. Visualization of vortices - isosurfaces at $\lambda_2 = 0$. Colors by vorticity magnitude; aspect ratio $AR = 17.3$, $Re = 905$. Black line denotes reattachment line of the primary recirculation flow region; red line ilustrates secondary flow region projected on the upper wall.

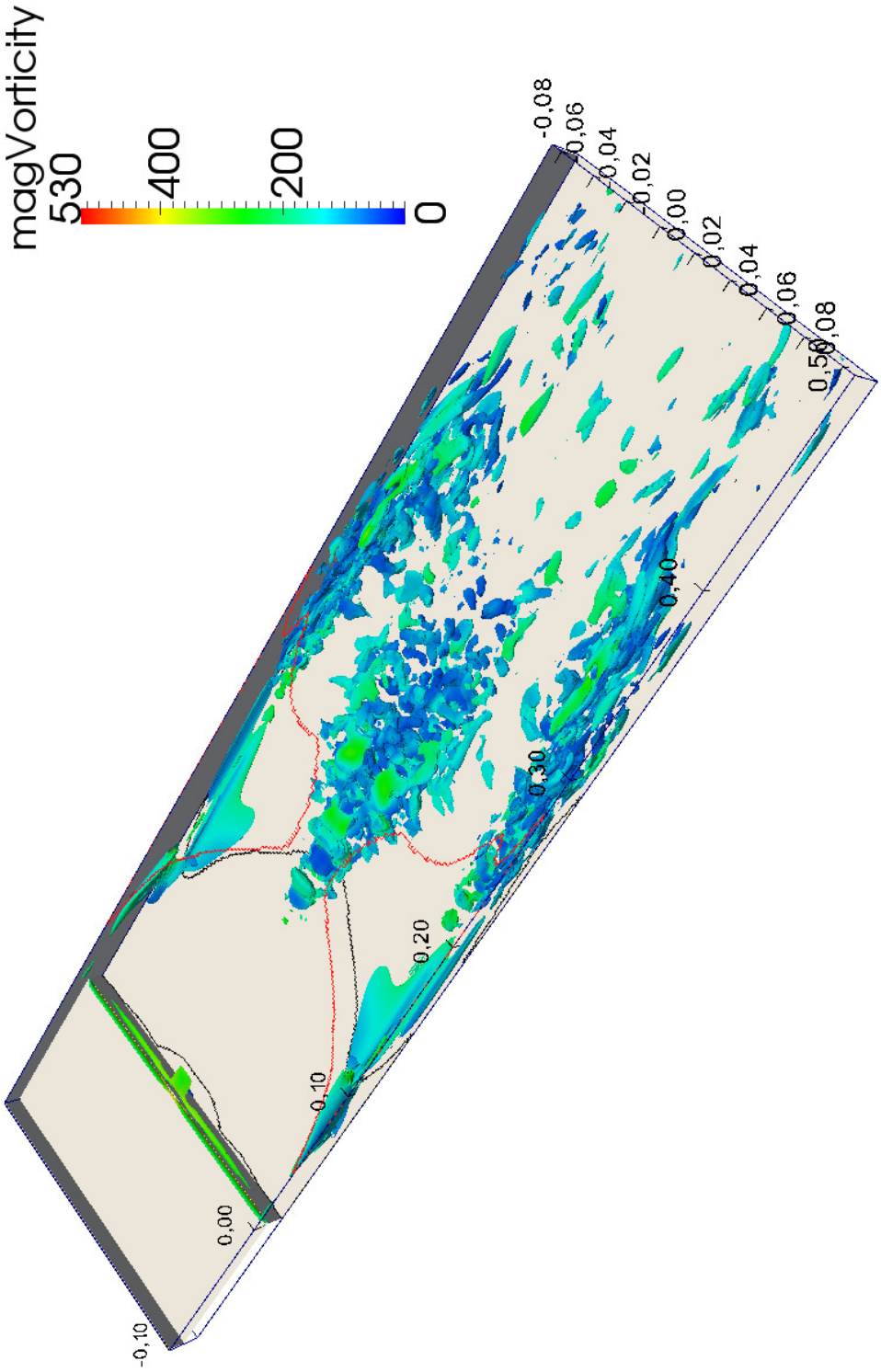

Figure 3.9. Visualization of vortices - isosurfaces at $\lambda_2 = -400$. Colors by vorticity magnitude; aspect ratio $AR = 17.3$, $Re = 905$. Black line denotes reattachment line of the primary recirculation flow region; red line ilustrates secondary flow region projected on the upper wall.

Chapter 4. Results and discussion

4.1. Inlet flow properties

Measurements at the inlet section were conducted to provide information on the quality of the channel inlet and to give information about velocity and turbulence intensity profiles at the same location as well as about the symmetry of velocity profiles at the inlet. Table 4.1 shows Reynolds numbers and bulk velocities that were set during the measurements when half of the channel was scanned. Fig. 4.1 and 4.2 demonstrate spanwise velocity profiles at the horizontal middle plane $y/S = 1.5$ (horizontal middle plane of the upstream section) at the upstream distance $x/S = -1$ from the step edge for cases $AR = 5.3$ and 17.3, where black marks indicate two-dimensional region close to the symmetry plane. The printed numbers express percentual width of this region which was found as point where the streamwise velocity is smaller than 0.98 of the moving average the velocity.

Different perspective is given by spanwise velocity profiles when the spanwise coordinate is expressed relative to step height as seen in Fig. 4.4 and Table 4.3. It is obvious that the boundary layer thickness at the sidewall is similar for all channel aspect ratios and all investigated Reynolds number and lies around $\delta/h = 1.4$. It is notable that the width of this two-dimensional region is almost independent from the Reynolds number while the depen-

	AR							
	5.3		8		17.3		33.2	
Re	Re_{true}	$U_b[m/s]$	Re_{true}	$U_b[m/s]$	Re_{true}	$U_b[m/s]$	Re_{true}	$U_b[m/s]$
220	**218**	**0.1787**	**296**	**0.2427**	**256**	**0.2099**	**229**	**0.1828**
450	**437**	**0.3583**	**505**	**0.4140**	**476**	**0.3903**	**465**	**0.3813**
670	**652**	**0.5346**			**703**	**0.5764**	**679**	**0.5567**
900	**874**	**0.7166**	**976**	**0.8002**	**934**	**0.7658**	**904**	**0.7412**
1100	**1084**	**0.8888**			**1165**	**0.9552**	**1179**	**0.9667**

Table 4.1. Intended Reynolds numbers (first column) versus true Reynolds numbers and bulk velocities of the measurement for each aspect ratio.

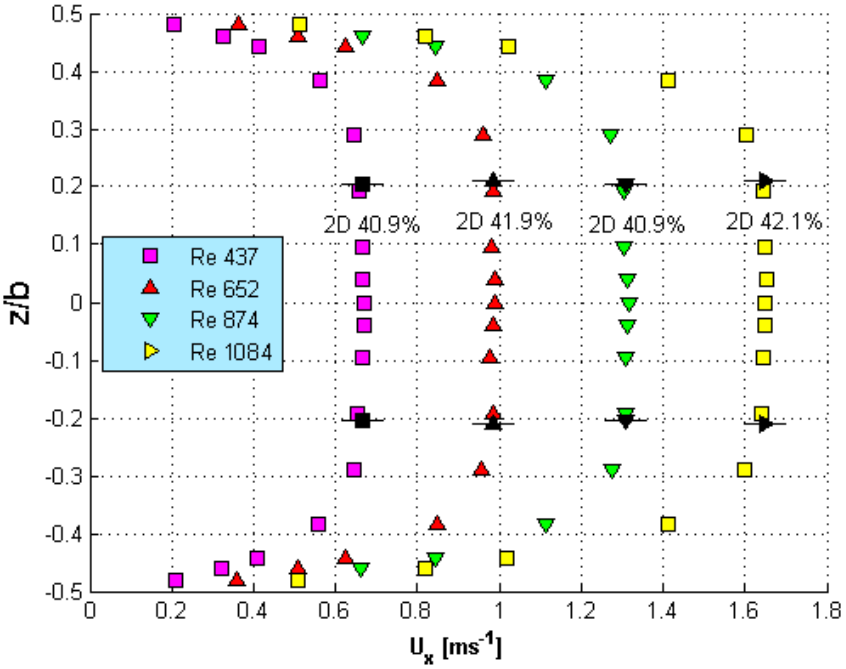

Figure 4.1. Spanwise velocity profiles in the horizontal middleplane $y/S = 1.5$ at upstream distance $x/S = -1$, aspect ratio $AR = 5.3$.

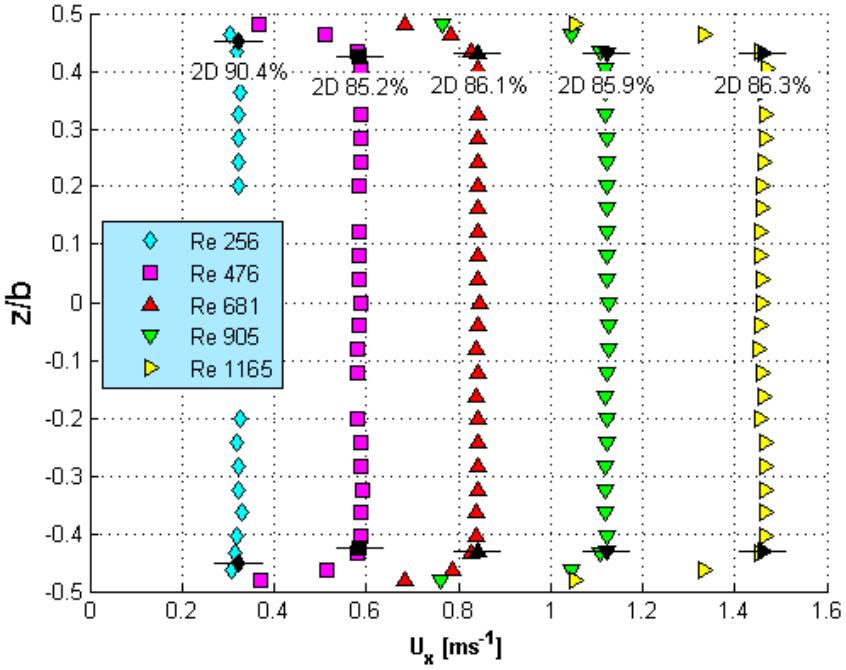

Figure 4.2. Spanwise velocity profiles in the horizontal middleplane $y/S = 1.5$ at upstream distance $x/S = -1$, aspect ratio $AR = 17.3$.

dence on the channel width is more significant as shown in Fig. 4.3 and Table. 4.2, where the spanwise coordinate is expressed relative to channel width. Figure 4.5 demonstrates good conformity between velocity profiles, measured at the symmetry plane and at the upstream distance $x/S = -1$ from step edge, with corresponding laminar velocity profiles calculated using equation

$$U(y) = -\frac{U_{\max}}{h^2}(y^2 - hy) \tag{4.1.1}$$

where $U_{\max}$ is 3/2 bulk velocity U_b used in relation for Reynolds number. The conformity is good for all Reynolds numbers over entire channel height except region between $y/S = (1.8 : 2)$, where strong laser light reflections from tracking particles, settled on the upper plane at the region close to $x/S = 0$, occured.

	AR			
Re	**5.3**	**8**	**17.3**	**33.2**
220			90.4	86.6
450	40.9	63.6	85.2	89.6
670	41.9		86.1	
900	40.9		85.1	
1100	42.1		86.3	

Table 4.2. Percentual width of two-dimensional region close to symmetry plane.[1]

Spanwise distributions of turbulence intensity are illustrated in Fig. 4.6. For wide channels with $AR = 17.3$ and 33.2, the turbulence intensity in the two-dimensional region close to symmetry plane indicates constant values with average value 0.8%. On the contrary, narrow channels with $AR = 5.3$ and 8 have higher turbulence intensity with average value lying around 3% and slightly higher for the case $AR = 8$, what can explain the earlier drop in slope angle of reattachment length (see Fig. 4.11) as reported by Isomoto [30]. Individual measurements in the channel with $AR = 5.3$ show scattered values without any dependence on Reynolds number in the case of $AR = 5.3$ (see Fig. 4.7), while in the case

[1]The Reynolds numbers in the first columnt represent intended Reynolds numbers of particular measurements, see Table 4.1.

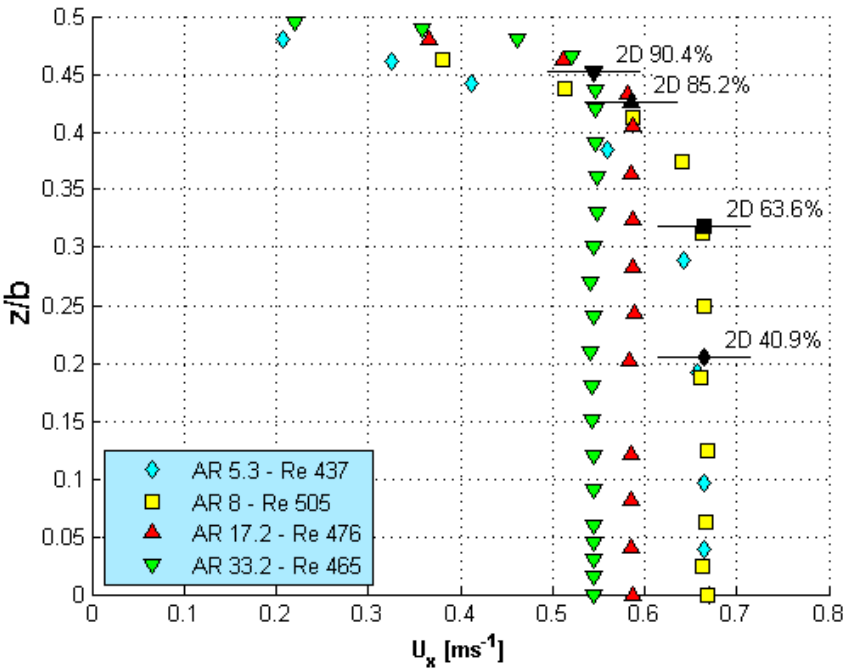

Figure 4.3. Spanwise velocity profiles in the horizontal middleplane $y/S = 1.5$ at upstream distance $x/S = -1$; spanwise coordinates expressed relative to channel width. The two-dimensional region around the channel symmetry plane expressed by black mark and percentual ratio within the chart.

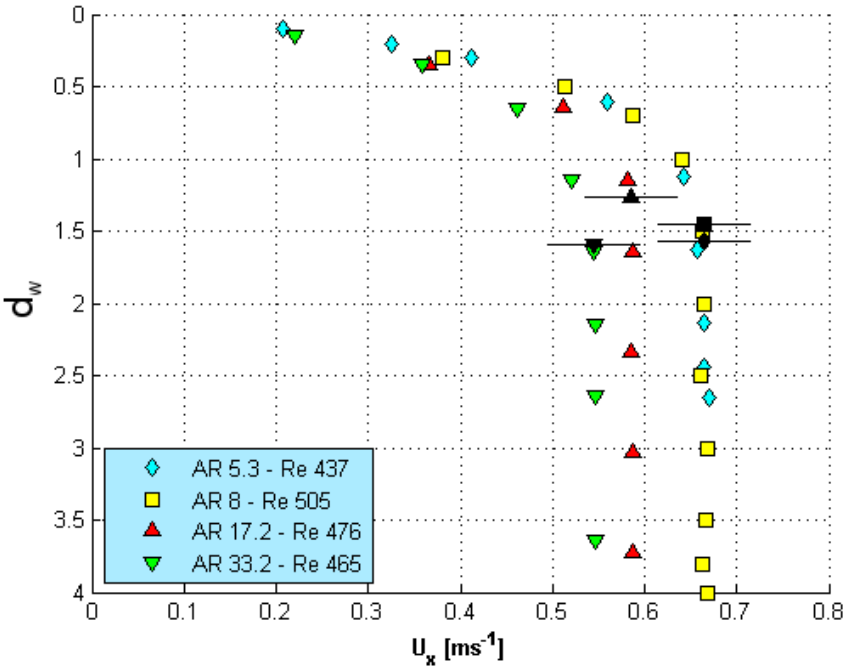

Figure 4.4. Spanwise velocity profiles in the horizontal middleplane $y/S = 1.5$ at upstream distance $x/S = -1$; spanwise coordinates expressed as absolute distance from the sidewall.

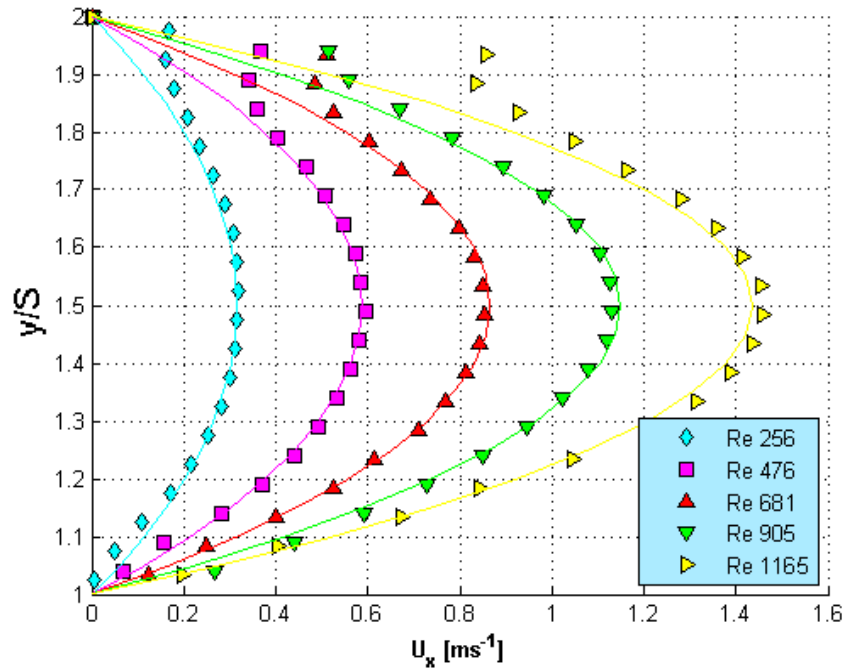

Figure 4.5. Measured velocity profiles at upstream channel section symmetry plane $z/b = 0$ at upstream distance $x/S = -1$, aspect ratio $AR = 17.3$, compared with corresponding laminar velocity profiles.

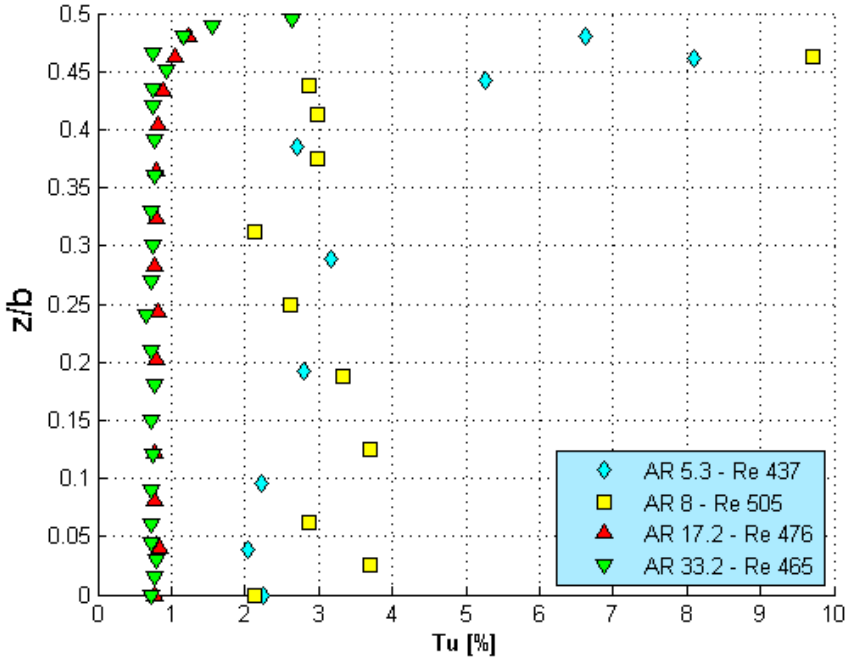

Figure 4.6. Spanwise turbulence intensity profiles at upstream channel section horizontal middleplane $y/S = 1.5$ at upstream distance $x/S = -1$.

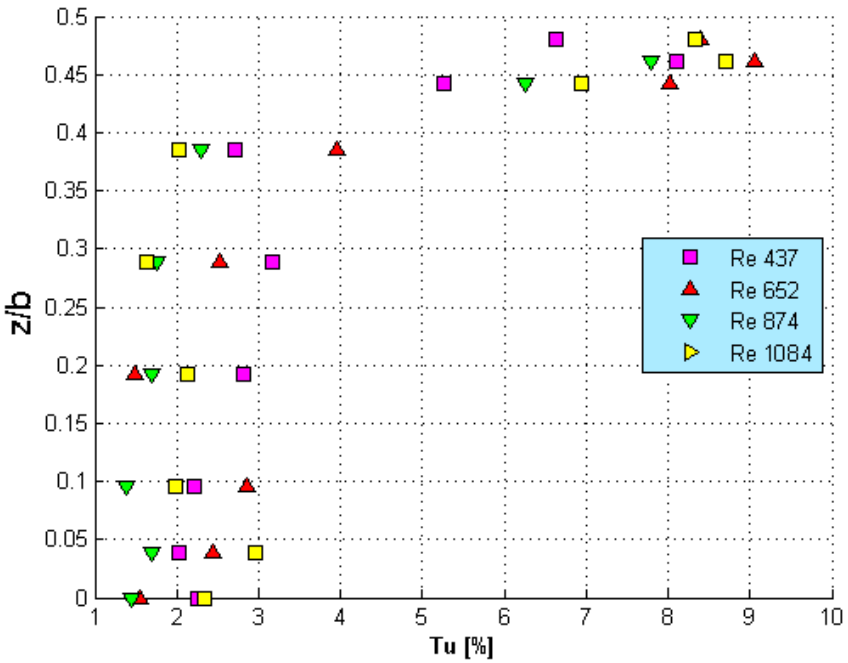

Figure 4.7. Spanwise turbulence intensity profiles at upstream channel section horizontal middleplane $y/S = 1.5$ at upstream distance $x/S = -1$, aspect ratio $AR = 5.3$.

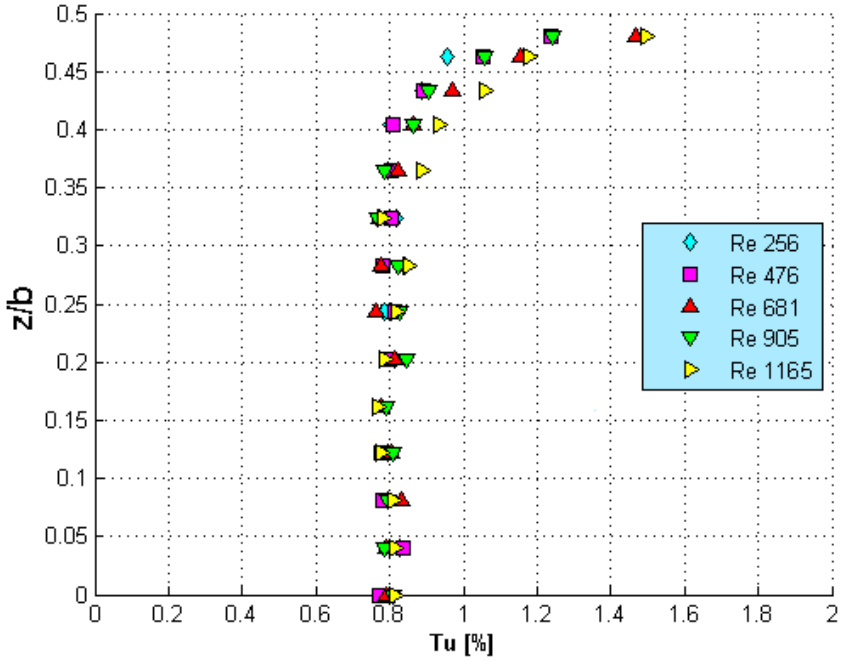

Figure 4.8. Spanwise turbulence intensity profiles at upstream channel section horizontal middleplane $y/S = 1.5$ at upstream distance $x/S = -1$, aspect ratio $AR = 17.3$.

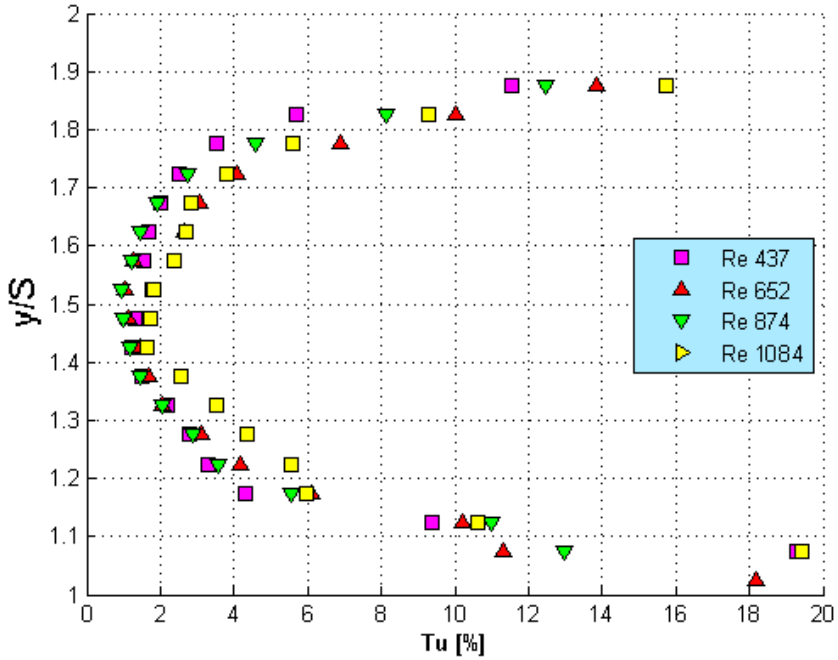

Figure 4.9. Turbulence intensity profiles at upstream channel section symmetry plane $z/b = 0$ at upstream distance $x/S = -1$, aspect ratio $AR = 5.3$.

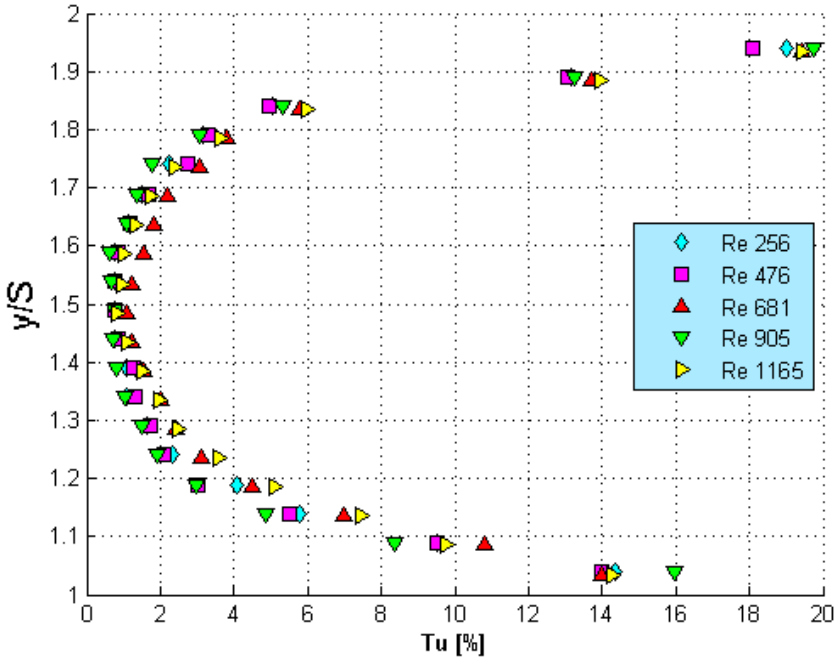

Figure 4.10. Turbulence intensity profiles at upstream channel section symmetry plane $z/b = 0$ at upstream distance $x/S = -1$, aspect ratio $AR = 17.3$.

of wide channel with aspect ratio $AR = 17.3$, there is good conformity between the results of all investigated Reynolds numbers (see Fig. 4.8). Turbulence intensity results obtained at the symmetry plane are shown in Fig. 4.9 and Fig. 4.10; the lowest value lie in the channel horizontal middle plane and rises towards top and bottom wall. Similar to spanwise turbulence intensity profiles also the values in the case of narrow channel $AR = 5.3$ are scattered (see Fig. 4.9), while in the case of wide channel $AR = 17.3$, they are in good conformity (see Fig. 4.10).

	AR			
Re	**5.3**	**8**	**17.3**	**33.2**
220			0.827	1.59
450	1.54	1.46	1.28	1.61
670	1.51		1.2	
900	1.54		1.22	
1100	1.5		1.19	

Table 4.3. Boundary layer thickness δ/S adjacent to sidewall.[1]

4.2. Reattachment length

The fundamental feature of separated flow in duct with backward-facing step geometry is the reattachment length for its meaning to heat transfer properties behind the step. The reattachment length at the symmetry plane was measured for all aspect ratios in wide range of Reynolds numbers; the results are illustrated on Fig. 4.11 together with experimental results by Armaly [5] and Nie and Armaly [50] and numerical results by Kitoh [37]. The reattachment location is here defined as a point where the average streamwise velocity component adjacent to the wall is equal zero (see Eq. 2.4.9).

All results steadily increase the reattachment length with increasing Reynolds number in the laminar regime, the slope in the case of the widest channel $AR = 33.2$ corresponds to

$$2.1724 + 0.0138Re \tag{4.2.1}$$

[1]The Reynolds numbers in the first column represent intended Reynolds numbers of particular measurements, see Table 4.1.

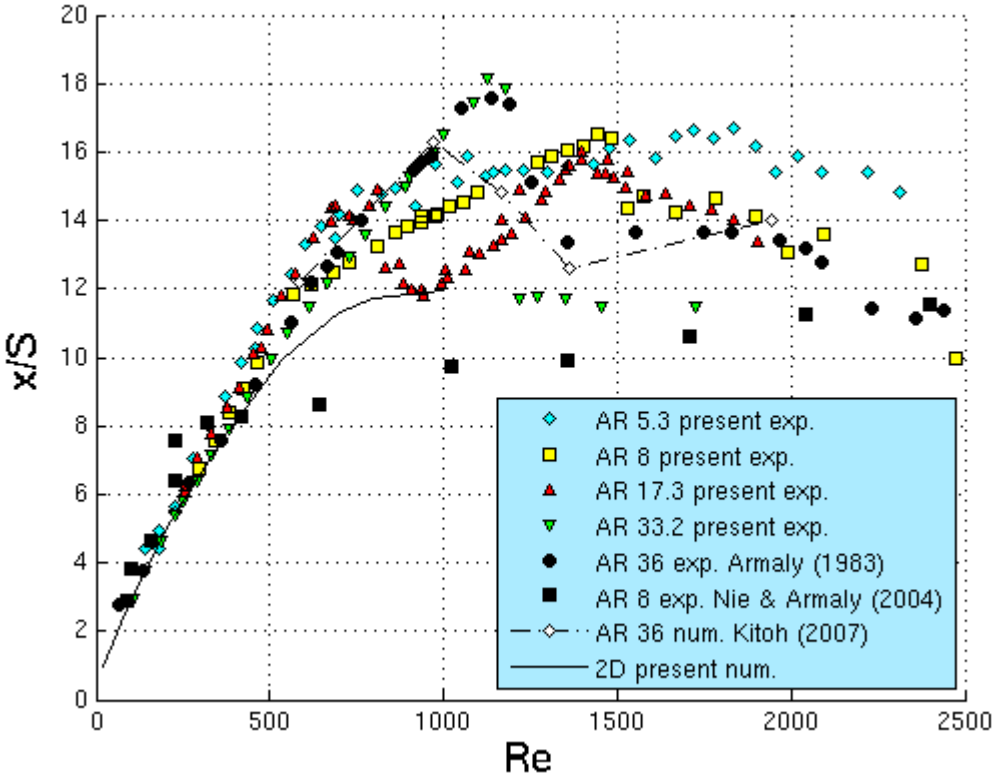

Figure 4.11. Reattachment length versus Reynolds number.

up to maximum reattachment length found at $x_1/S = 18.2$ at Reynolds number 1183 and followed with sudden drop back to $x_1/S \sim 12.5$. This is in very good conformity with the experimental data by Armaly [5] which are also depicted for comparison. On the contrary, in the case of narrow channels ($AR = 5.3$; 8 and 17.3), the trend of reattachment length curve demonstrate steeper increase corresponding to

$$1.5401 + 0.0187Re \tag{4.2.2}$$

up to Reynolds number ≈ 681, respectively, up to $Re = 561$ for $AR = 8$. At this point a transition regime probably begins. After this Reynolds number, the reattachment lenght increses less steeply until it reaches maximum lenght $x_1/S = 16.7$ and 16.5 at Reynolds number 1837 and 1444 for $AR = 5.3$ and 8, respectively. When the Reynolds number is increased further, as in the case of $AR = 5.3$, 8 and 17.3, it slowly decreases; it can be expected that it stabilizes around steady value after fully turbulent flow is developed as was demonstrated

by Armaly [5]. Presented results demonstrate shorter maximum reattachment length when the aspect ratio is $AR = 17.3$ than in the case of aspect ratio $AR = 33.2$.

In the case of $AR = 8$, there is apparent earlier onset of transition demonstrated by drop in the trend angle of the reattachment length. It is questionable if this is either due to different inlet design inside the settling chamber contrary to all other channels that all have the same inlet design or due to the effects of sidewalls, but it is noteworthy, that the maximum reattachment length in this case is almost the same length as in the case of narrowest channel $AR = 5.3$. Also the turbulence intensity in middle of the channel at the horizontal middle plane $y/S = 1.5$ is approximately of the same magnitude (see Fig. 4.6). Notable is that in the cases of $AR = 5.3$ and 17.3, that has the same inlet design, the onset of transition appears around the same Reynolds number and the same reattachment length. For comparison results by Nie and Armaly [50] are presented, which reach approximately only 2/3 of reattachment length of present results for the case of $AR = 8$ between the point of onset of transition regime and at the maximum reattachment length. They results indicate faster growth of reattachment length in the laminar regime and flatter growth in the transition regime with maximum reattachment length at higher Reynolds number than present case. It is questionable if this discrepancy between presented results and results of Nie and Armaly [50] is not caused by different expansion, since they had $ER = 2.02$ compared to present $AR = 2$, what according numerical simulation by Kitoh et al. [37] causes shortening of the reattachment length as the expansion ratio is increased. Also measurements by Ötügen [52] indicate same phenomena as results by Kitoh et al. [37], but his results vary only slightly, about 4, 5%. Thus it appears more likely that the earlier onset of transition in the case of $AR = 8$ is caused by the different inlet design and that the flow after this critical Reynolds number is than more affected by the transition and the sidewall effects that limits the maximum of reattachment length.

On the contrary to all other results, the reattachment length for aspect ratio $AR = 17.3$ steeply drops around Reynolds number 681; decreases its length from $x_1/S \sim 14.5$ back to value approximately 12 at $Re \sim 905$ and then again rises less steeply up to maximum reattachment length $x_1/S = 16$ at $Re = 1399$. This phenomena firstly appeared as a result of some fault in the experimental setup credited to some opening in the connection between

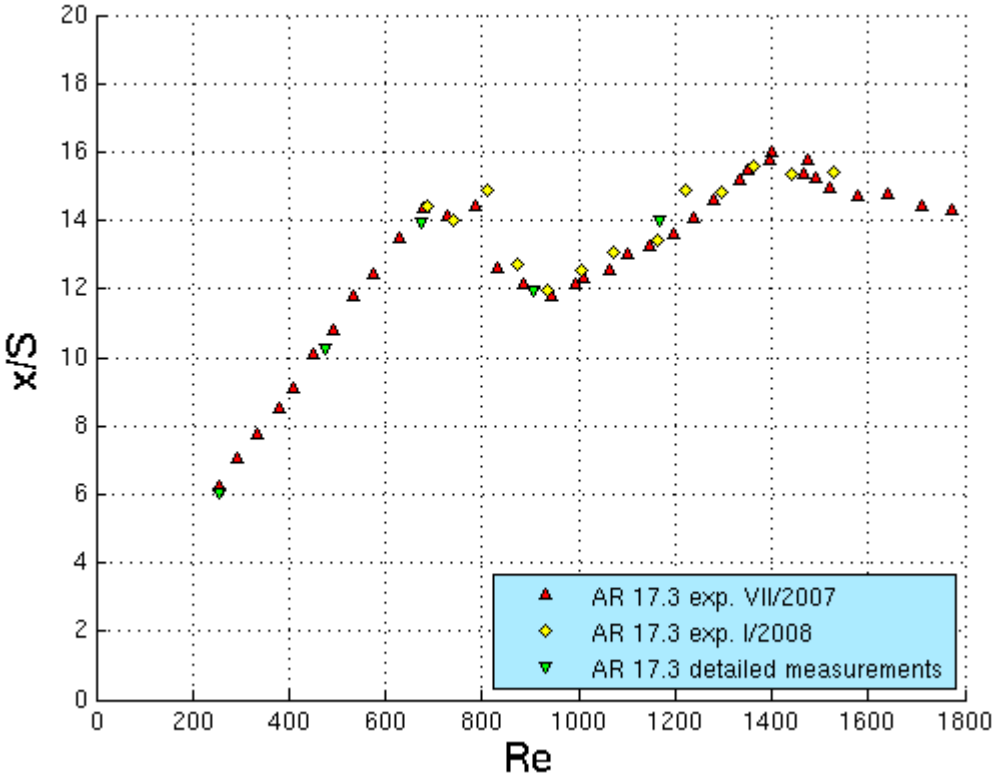

Figure 4.12. Reattachment length versus Reynolds number in the case of AR = 17.3.

the settling chamber and the channel, thus second measurements to eliminate this doubt was done with special attention devoted to any leakages. The measurements were done in the same Reynolds number range as depicted in Fig. 4.12; marked by yellow diamonds. Also reattachment lengths resulting from measurements over half of the spanwise are depicted in the same figure; marked by green upside-down triangles. As seen on Fig. 4.12, all subsequently conducted measurements show the same phenomena as the former results and thus it is obvious that this phenomena is not caused by any fault in the experimental setup.

4.3. Primary recirculation flow region

The developed channel flow separates at the step edge and forms mixing layer that slowly propagates within the extended section past the step until it reaches the bottom plane at reattachment point and thereafter new channel flow starts to develop. This process is

accompanied by primary recirculation flow region development bounded by the bottom plane, the step plane and this shear layer whose development is dominated by the entrainment process due to flow rate from step corner region up to $2.5S$ as demonstrated by Isomoto and Honami [30]. At the reattachment point the inner mixing layer splits and portion of the fluid continues in the downstream direction while the other portion turns back in the upstream direction inside the primary recirculation flow region. The spanwise distributions of reattachment points at bottom plane are illustrated in figures 4.13 to 4.16 for all investigated aspect ratios and for all investigated Reynolds numbers. In most cases, the maximum reattachment length is located at the symmetry plane and drops towards the sidewalls with minimum reattachment length located close to sidewalls. In the cases with high aspect ratio and low Reynolds number, it has constant value in the two-dimensional region close to the symmetry plane and thereafter it starts to drop similarly to the other cases and reaches the minimum reattachment length close to the sidewall as demonstrated in figures 4.13 to 4.16. After the reattachment length reaches the minimum, it rises again towards the sidewall, where the reattachment length is almost the same length as at the symmetry plane or even longer.

In all cases, the minimum in reattachment length, which is located close to sidewall, moves in the downstream direction towards the symmetry plane as the Reynolds number is increased. From these figures it could be concluded that the distance of the minimum reattachment length from the sidewall is strongly dependent on the aspect ratio of the channel when the spanwise distance is related to the channel width. But considering distance related to the step height, it reveals the distance from sidewall δ_{sw}/S is weakly dependent on aspect ratio as demonstrated in Table 4.4.

In the case with high aspect ratio $AR = 17.3$ and 33.2 and high Reynolds number, the maximum reattachment length was not found at the symmetry plane but approximately in one quarter of the channel width, from the symmetry plane (see Fig. 4.16).

The width of two-dimensional region close to the symmetry plane was obtained using the same data processing as for inlet spanwise velocity profile. No proof about two-dimensional region in channels with aspect ratio $AR = 5.3$ and 8 (see Fig. 4.13 and 4.14) was found, although it seems there is a very narrow two dimensional region at lowest Reynolds

	AR							
	5.3		**8**		**17.3**		**33.2**	
Re	x_1/S	δ_{sw}/S	x_1/S	δ_{sw}/S	x_1/S	δ_{sw}/S	x_1/S	δ_{sw}/S
220	4.46	0.72	4.83	0.89	4.16	0.77	3.57	0.83
450	7.69	0.67	6.92	1.02	5.37	0.93	4.16	0.93
670	9.52	0.84			6.29	1.03	4.96	1.13
900	10.86	0.83	9.19	1.51	6.33	1.36	8.46	1.89
1100	10.99	1.32			7.74	1.57	7.39	1.89

Table 4.4. Location of minimum reattachment length. Minimum reattachment length in left column, distance from sidewall δ_{sw}/S in right column.[1]

number 218 in the narrowest channel $AR = 5.3$. In the case of $AR = 17.3$ and 33.2, the two-dimensional region was found and is emphesised in Fig. 4.15 and 4.16 with black marks and line demonstrating maximum distance from the sidewall with the influence of sidewall effect. The width of the region influenced by sidewall effect is presented in Table 4.5. From the Fig. 4.15 it seems that the region affected by sidewall reaches the symmetry plane approximately at $Re \approx 700$ what exactly appears in the case where $Re = 681$. Similarly, the two-dimensional region close to the symmetry plane was found for the case of $AR = 33.2$, for Reynolds number $Re = 679$, shown in Fig. 4.16, probably even higher, but detailed measurements were not performed. The line connecting all points, where maximum width of two-dimensional region appears, demonstrates linear dependence on reciprocal Reynolds number (understand $1/Re$) and according this, the region affected by sidewall should reach the symmetry plane at $Re \approx 1100$ at distance $x_1/S \approx 22$ from the step edge, what obviously does not happend, as seen in Fig. 4.11.

	AR	
Re	**17.3**	**33.2**
220	4.43	4.6
450	6.54	7.6
670		10.61

Table 4.5. Thickness δ_{sw}/S of region affected by sidewall effect.[1]

[1]The Reynolds numbers in the first columnt represent intended Reynolds numbers of particular measurements, see Table 4.1.

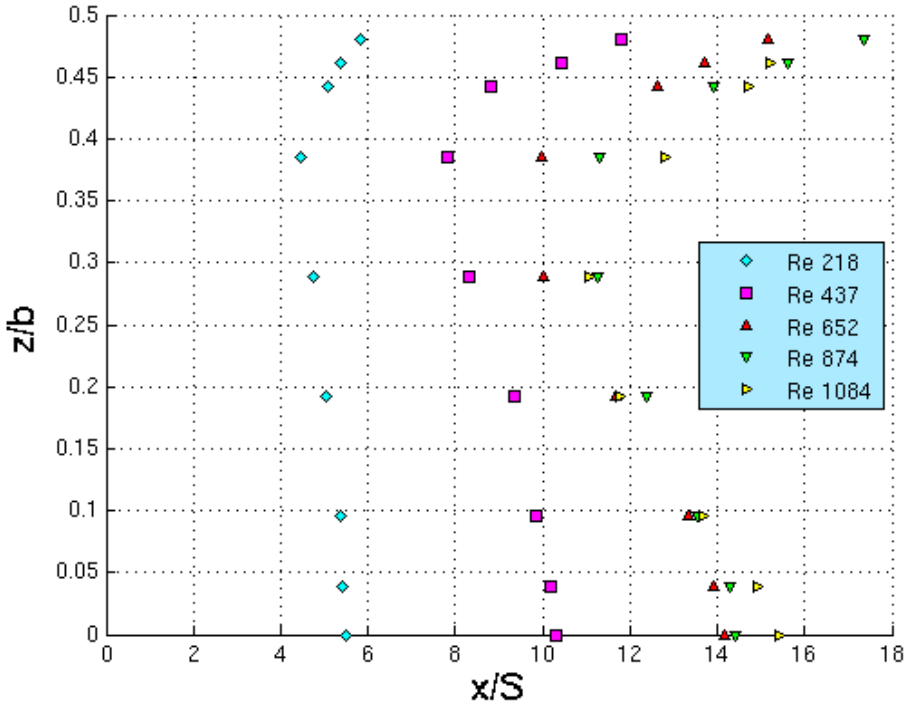

Figure 4.13. Spanwise distribution of reattachment length at the bottom plane, aspect ratio $AR = 5.3$.

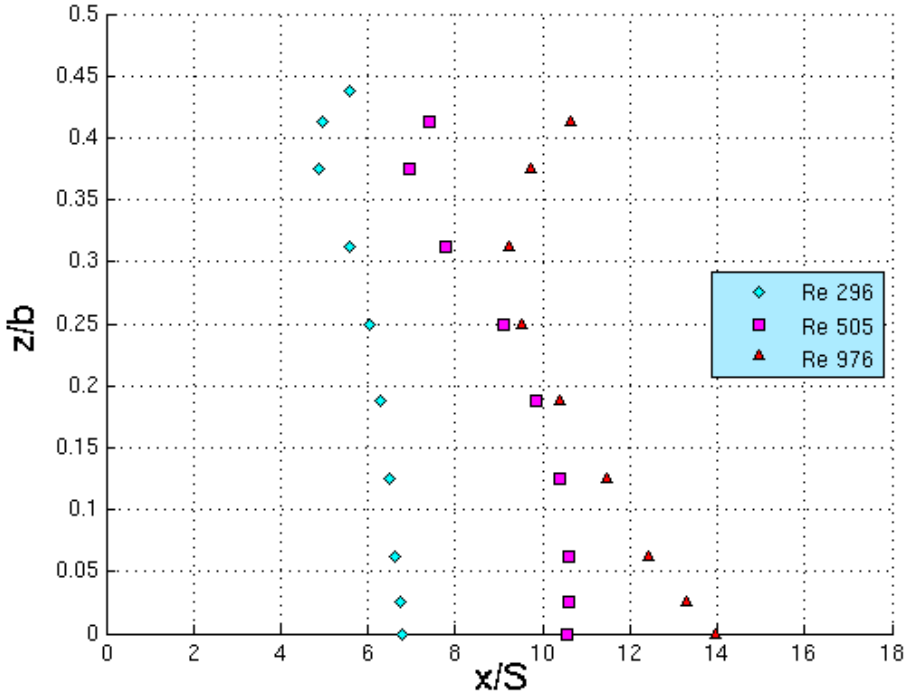

Figure 4.14. Spanwise distribution of reattachment length at the bottom plane, aspect ratio $AR = 8$.

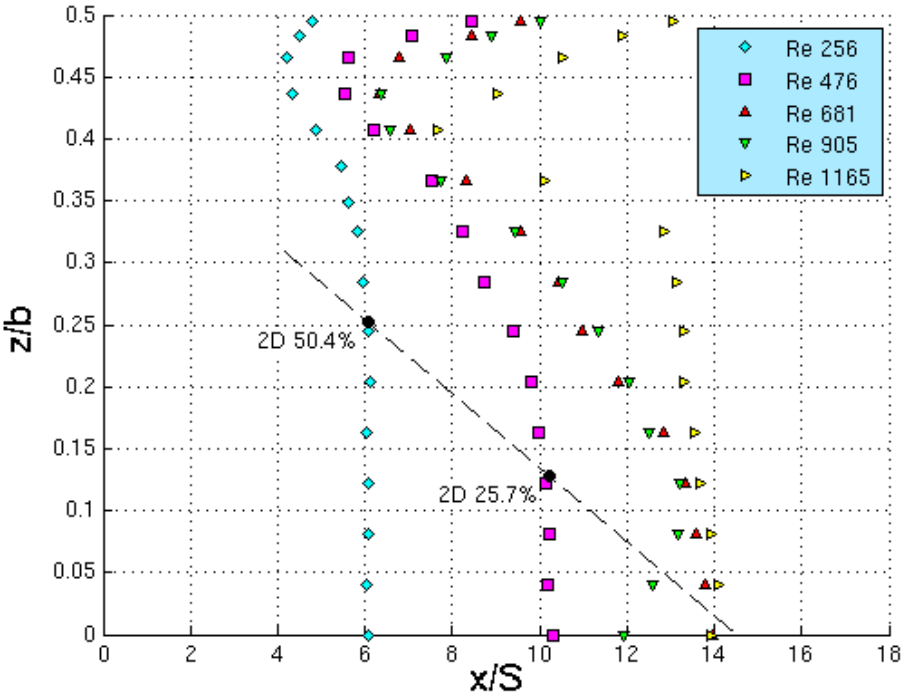

Figure 4.15. Spanwise distribution of reattachment length at the bottom plane, aspect ratio $AR = 17.3$.

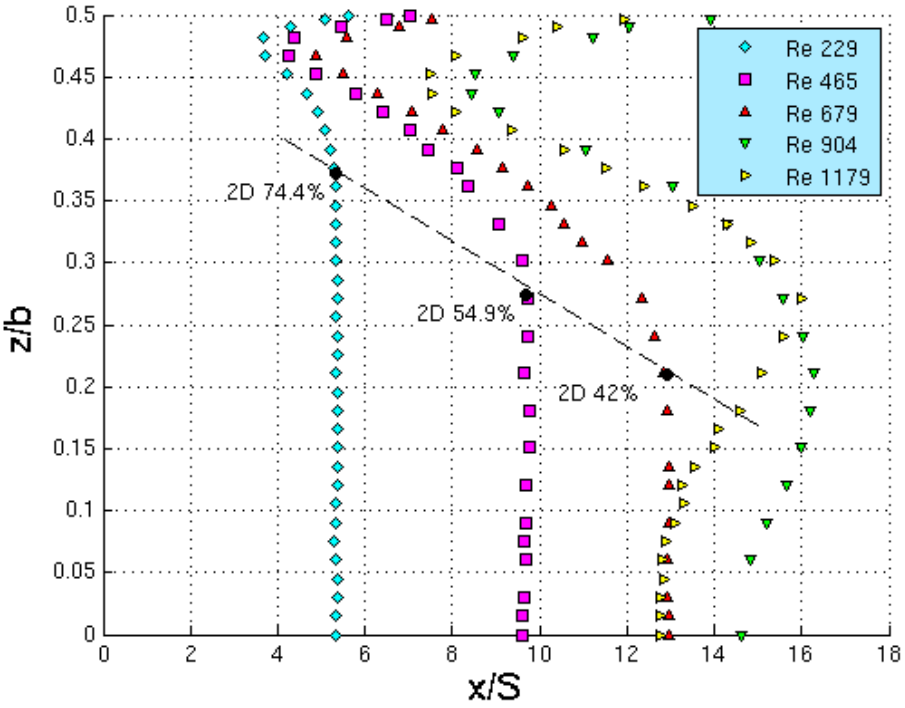

Figure 4.16. Spanwise distribution of reattachment length at the bottom plane, aspect ratio $AR = 33.2$.

The possible explanation for the earlier vanishing of the two-dimensional like flow near the symmetry plane than it could be expected from the interpolation lines in Fig. 4.15 and Fig. 4.16, involves the influence of the secondary recirculation flow region that appears adjacent to the top wall (see Fig. 4.19). This secondary recirculation flow region acts as an obstacle that pushes the bulk flow towards the bottom plane and thus shortens the reattachment length. But the question has to be issued why the secondary recirculation flow region does not extend over the entire span, but that the ''initial'' secondary recirculation flow region, that extends from the sidewall towards the symmetry plane as the Reynolds number increases, is interrupted at one quarter of the channel width and another recirculation flow region appears close to the symmetry plane adjacent to the top wall (see Fig. 4.19), and that the maximum reattachment length appears exactly at the same spanwise distance from the symmetry plane where the secondary recirculation flow region is interrupted (see Fig. 4.16). This fact is in direct conflict with result obtained in channel with $AR = 17.3$, where no secondary recirculation flow region close to the symmetry plane adjacent to the top wall (see Fig. 4.18) is observed, although the reattachment length has local minimum at the symmetry plane for $Re = 905$. Unfortunately, measurements performed only in one half of the channel cannot give the ansver if the flow loses the symmetry for higher Reynolds numbers. Thus the assumption that the present range of investigated Reynolds numbers yields symmetrical flow in the downstream section seems to be wrong.

4.4. Secondary recirculation region adjacent to top wall

Secondary recirculation flow region starts to develop adjacent to the top wall and extends from sidewall towards the symmetry plane as the Reynolds number increases as shown in Figures 4.17 to 4.19, where zero streamwise velocity contours at the top wall demonstrate the size of secondary recirculation flow region. The zero streamwise velocity countour at the top plane has symmetrical lenticular shape for Reynolds numbers below ≈ 650 and the streamwise distance of the bubble center axis from the step edge is almost identical with the reattachment length at the symmetry plane as demonstrated by the plotted lines. The bubble center axis moves further from the step edge and the bubble spreads towards

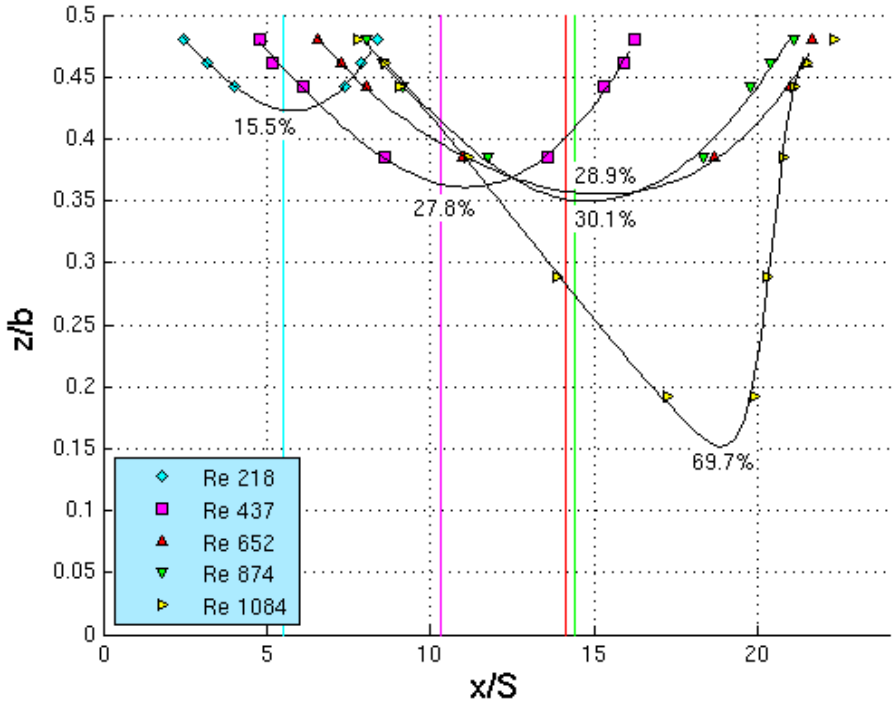

Figure 4.17. Location of secondary recirculation flow region at the top plane, aspect ratio $AR = 5.3$.

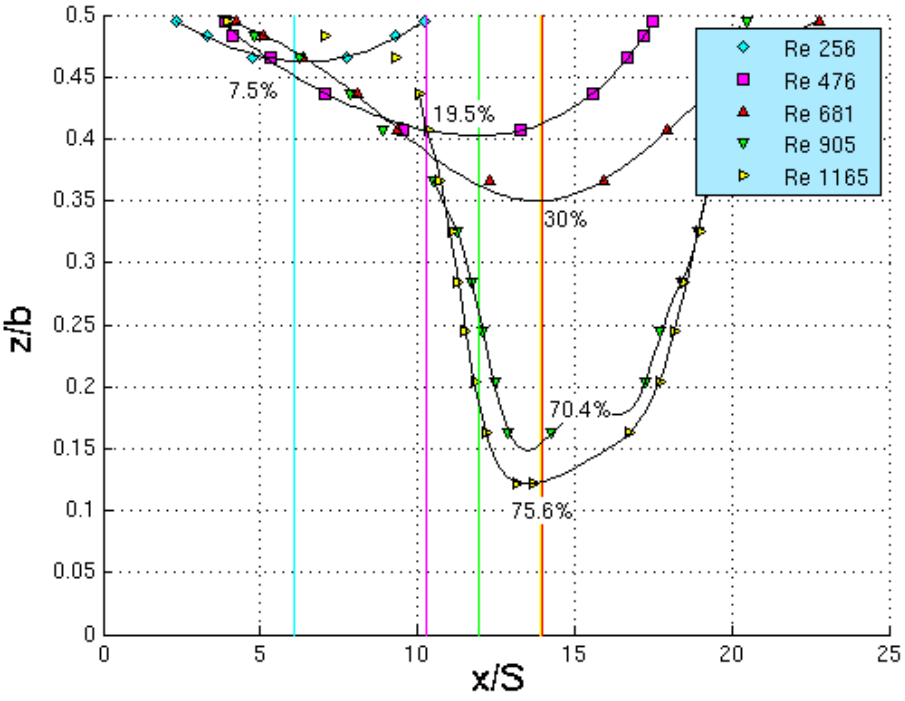

Figure 4.18. Location of secondary recirculation flow region at the top plane, aspect ratio $AR = 17.3$.

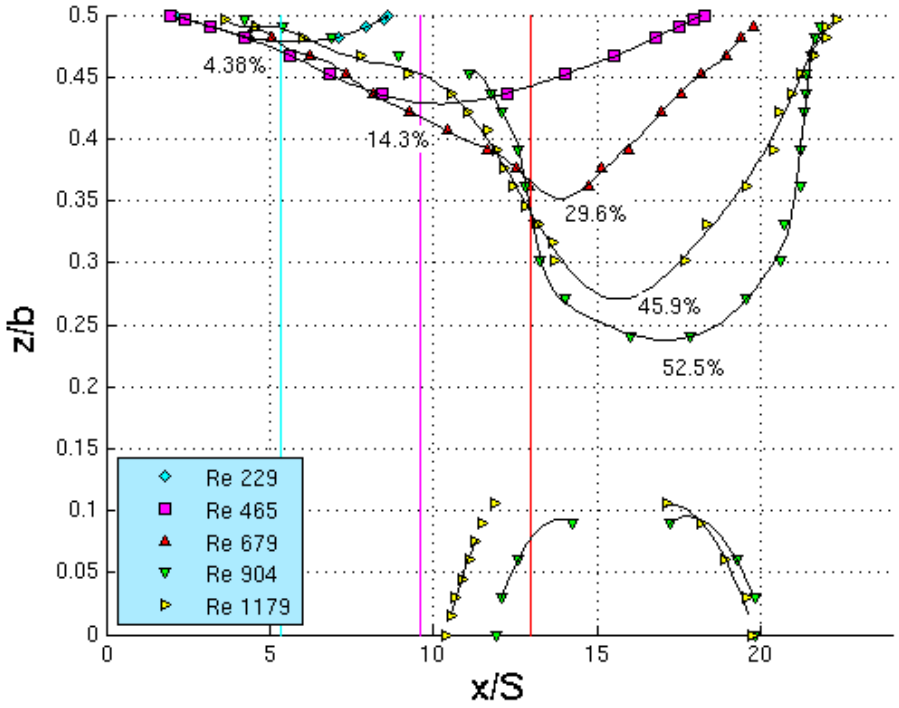

Figure 4.19. Location of secondary recirculation flow region at the top plane, aspect ratio $AR = 33.2$.

the symmetry plane as the reattachment length becomes longer with increasing Reynolds number.

When the Reynolds number is larger than ≈ 650 the zero streamwise velocity line at the top wall begins to change shape. The lenticular part elongates in the streamwise direction and loses its initial symmetry and extends towards the symmetry plane. The separation line of the bubble extends slowly towards the symmetry plane as the streamwise distance rises while the reattachment line returns quickly back to sidewall. No evidence of the secondary recirculation flow region close to the symmetry plane was found for all Reynolds numbers and all aspect ratios below $AR \leq 17.3$ as was already predicted in numerical simulation by Chiang et al. [16]. Isolated recirculation flow region develops close to the symmetry plane in the case of $AR = 33.2$, when the Reynolds number is over 900 (see Fig. 4.19), similar to the results by Armaly et al. [5]. The recirculation flow region close to the symmetry plane has the center axis closer to the step edge than the initial recirculation flow region emanating from the sidewall. A curve was fitted through these points to extrapolate and to locate the maximum distance from the sidewall, where the secondary recirculation flow

	AR			
Re	**5.3**	**8**	**17.3**	**33.2**
220	15.5%		7.5%	4.4%
450	27.8%		19.5%	14.3%
670	28.9%		30%	29.6%
900	30.1%		70.4%	52.5%
1100	69.7%		75.6%	45.9%

Table 4.6. The maximum distance from the sidewall where the secondary recirculation flow region extends at the top plane.[1]

region extends at the top plane, and is found in Table. 4.6 and in Figures 4.17 to 4.19 as percents of the half of the channel width. The aspect ratio $AR = 8$ was not investigated.

Vertical dimensions of top recirculation flow region described as points where streamwise velocity component is zero are depicted in Figures 4.20 through 4.24. The empty circles mark position where zero streamwise velocity component was found at cross-sec-

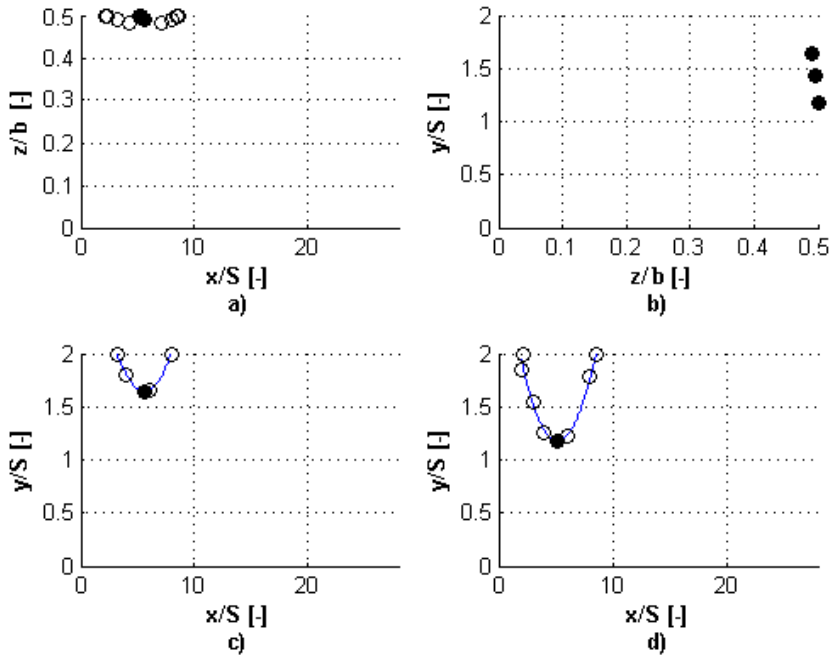

Figure 4.20. The secondary recirculation flow region adjacent to top wall $AR = 33.2$ and $Re = 218$. a) at top wall, b) streamwise view, c) 'xy'-plane $z/b = 0.4895$, d) 'xy'-plane $z/b = 0.4985$.

[1]The Reynolds numbers in the first columnt represent intended Reynolds numbers of particular measurements, see Table 4.1.

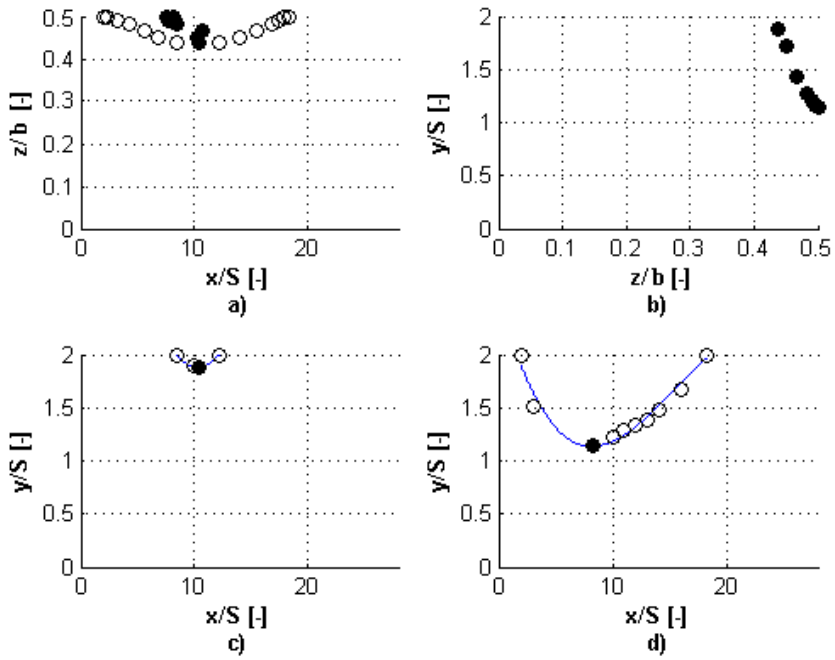

Figure 4.21. The secondary recirculation flow region adjacent to top wall $AR = 33.2$ and $Re = 465$. a) at top wall, b) streamwise view, c) 'xy'-plane $z/b = 0.4354$, d) 'xy'-plane $z/b = 0.4655$.

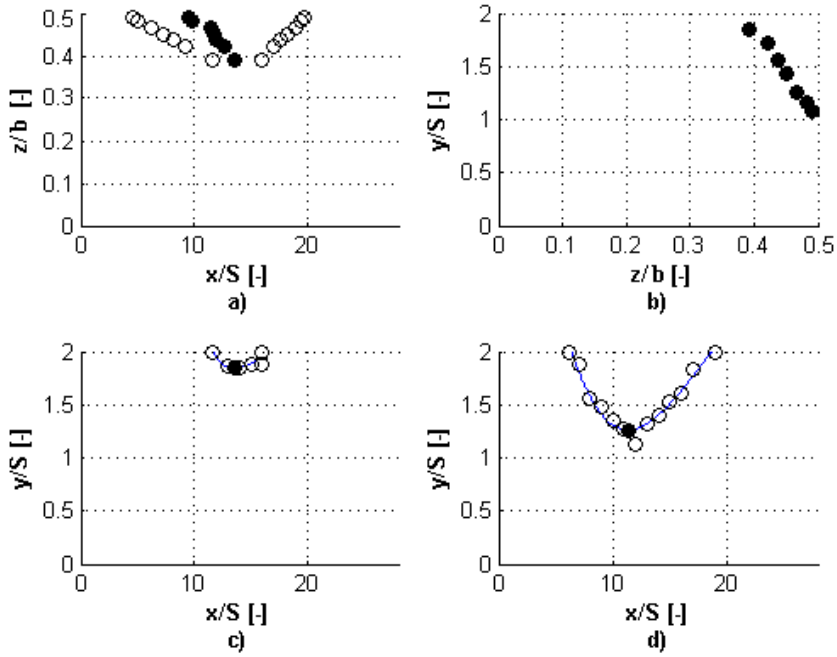

Figure 4.22. The secondary recirculation flow region adjacent to top wall $AR = 33.2$ and $Re = 679$. a) at top wall, b) streamwise view, c) 'xy'-plane $z/b = 0.3904$, d) 'xy'-plane $z/b = 0.4655$.

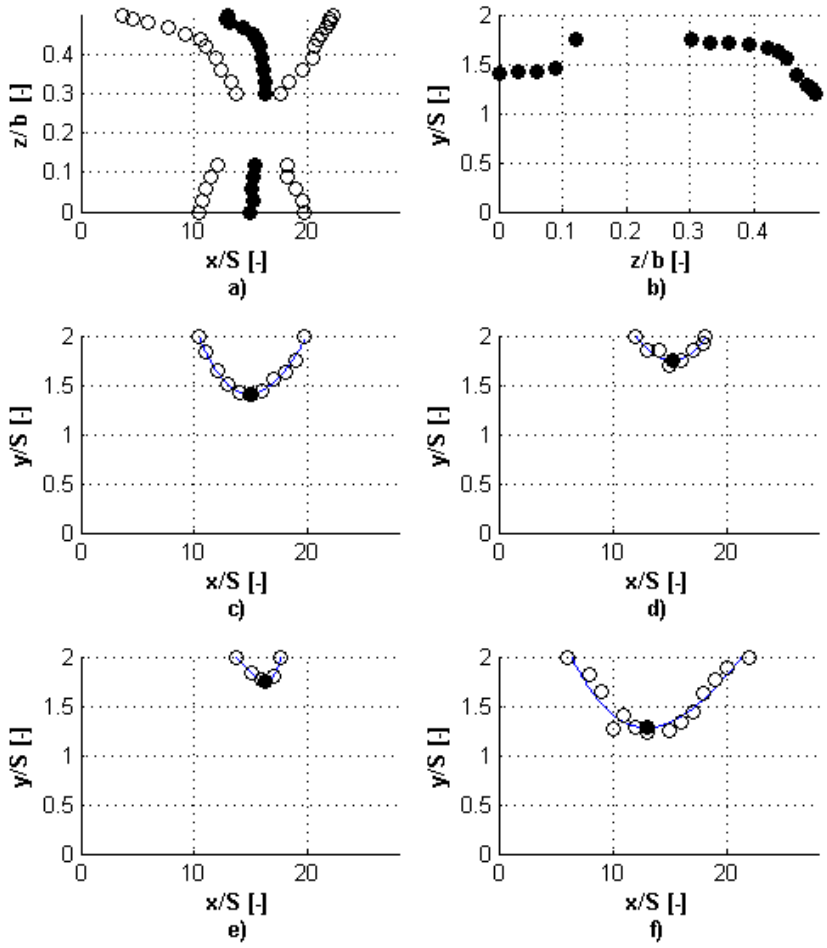

Figure 4.23. The secondary recirculation flow region adjacent to top wall $AR = 33.2$ and $Re = 1179$. a) at top wall, b) streamwise view, c) 'xy'-plane $z/b = 0$, d) 'xy'-plane $z/b = 0.1201$, e) 'xy'-plane $z/b = 0.3003$, f) 'xy'-plane $z/b = 0.4805$.

tions stepped every 1 S height from the step edge and a curve was fit through this points in every 'xy'-plane using Matlab polynomial of third or second order where more than three point were found or where exactly three points were found. The minimum vertical distance from the bottom wall, i.e., the maximum vertical dimension of the recirculation bubble was found and is marked by full circles. The recirculation bubble emanates approximately from the middle of the sidewall, e.g., $y/S \approx 1$ and rapidly shrinks its vertical size, however, it should be noticed that the exact vertical position of the bubble vertical origin at the sidewall is slightly doubtful as seen in Fig. 4.25 d) and 4.26 d), because the primary recirculation flow region and the secondary flow region merge in one recirculation flow region, forming

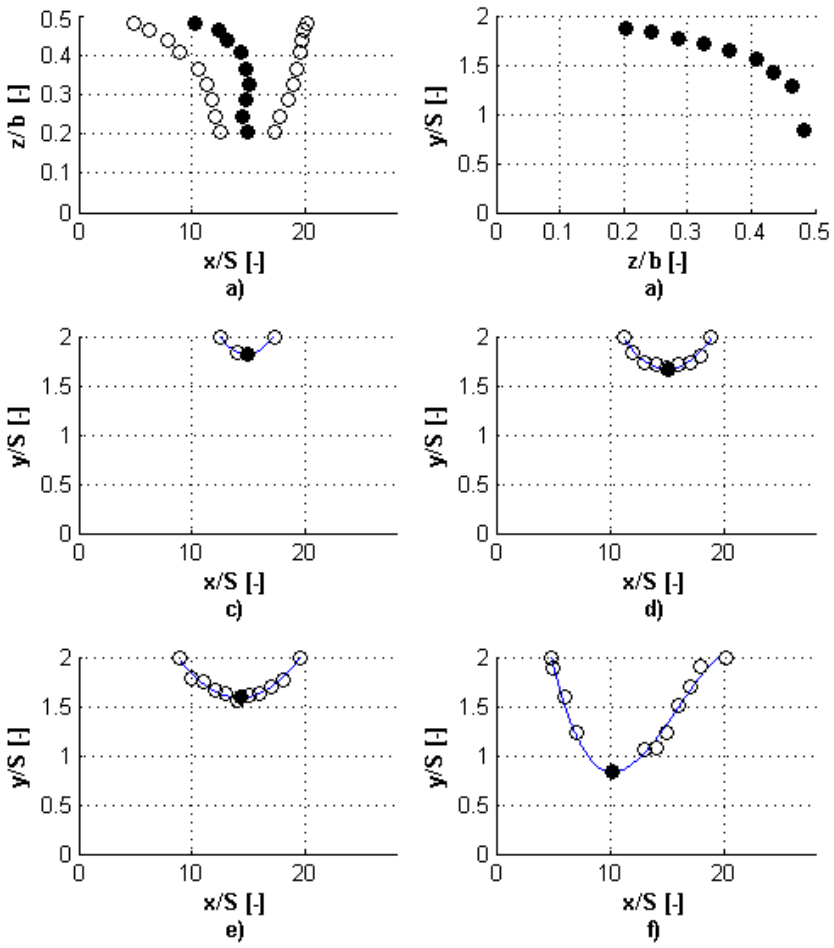

Figure 4.24. The secondary recirculation flow region adjacent to top wall $AR = 17.3$ and $Re = 905$. a) at top wall, b) streamwise view, c) 'xy'-plane $z/b = 0.2023$, d) 'xy'-plane $z/b = 0.3237$, e) 'xy'-plane $z/b = 0.4046$, f) 'xy'-plane $z/b = 0.4798$.

'X' shape area adjacent to sidewall. The streamwise position of maximum vertical size of the bubble is slightly shorter than the center axis of the bubble shape at the top plane when close to sidewall and thereafter it moves in streamwise direction and approximately coincides with the center axis of the bubble shape at the top plane. At high Reynolds numbers, the bubble top slowly extends towards the symmetry plane and has approximately the same vertical size between $z/b = 0.4$ and 0.3 (see Fig. 4.23), than entirely disappears to again appear around $z/b = 0.125$, where it forms recirculation bubble at the symmetry plane that has almost constant vertical size, extending approximately up to $y/S \approx 1.4$. It is questionable

if there is also some recirculation flow between $z/b = 0.3$ and 0.125 because the size of itegoration area was $32x16\ px^2$, i.e., $1.232x0.616\ mm^2$, thereby, if the recirculation region was thinner then the bubble size could lie under the current resolution. Similarly, in the case of $AR = 17.3$ at $Re = 905$, the recirculation flow bubble is relatively thin in the middle of the channel and rises towards the sidewall where it is almost thicker than the half of the channel height and thus strongly effects the flow there.

Figures 4.25 and 4.26 demonstrates flow situation adjacent to the wall. Streamlines starting from nine points at the upstream section at $x/S = -1$ with vertical resolution $y/S = 0.1$, and from nineteen points at the 'xz'-plane at $y/S = 0.05$ with streamwise resolution $x/S = 1$ illustrate complex flow that develops behind the step. Contours of streamwise velocity component emphasize weakening strength of the bulk flow as the observed plane moves towards the sidewall; the zero streamwise velocity contour is distinguished by empty circles.

a) When the 'xy' plane is far enough from the sidewall $z/b = 0.4655$ (see Fig. 4.25 a) and 4.26 a)), the entire fluid coming from the inlet section is pushed by the secondary recirculation flow region adjacent to the top plane towards the bottom plane but continues in the streamwise direction where it expands in the downstream section. No fluid particles coming from the inlet section are entrained neither inside the secondary flow region nor inside the primary recirculation region. The streamlines that undergo the circular motion inside the primary recirculation region originate from the points lying within the recirculation region and not beyond the reattachment point. The velocity contours show weakening character of the bulk flow in the streamwise direction even when considering the thickness of the secondary recirculation bubble adjacent to the top wall that acts as an obstacle and thus the relative cross-section area seems to be same. Thus it seems that the fluid has to flow in the spanwise direction, what is not recorded using simple two-dimensional PIV.

b) Fluid coming from $1.7 < y/S < 2$ at the inlet section partially supplies the secondary flow region where it undergoes circular motion around the middle of the channel and in section $z/b = 0.4895$, Fig. 4.25 b) and 4.26 b). The other part of the incoming fluid turns downstream inside the primary recirculation flow region and moves to the center of the primary recirculation flow region. It seems that no incoming fluid particles flow in the stream-

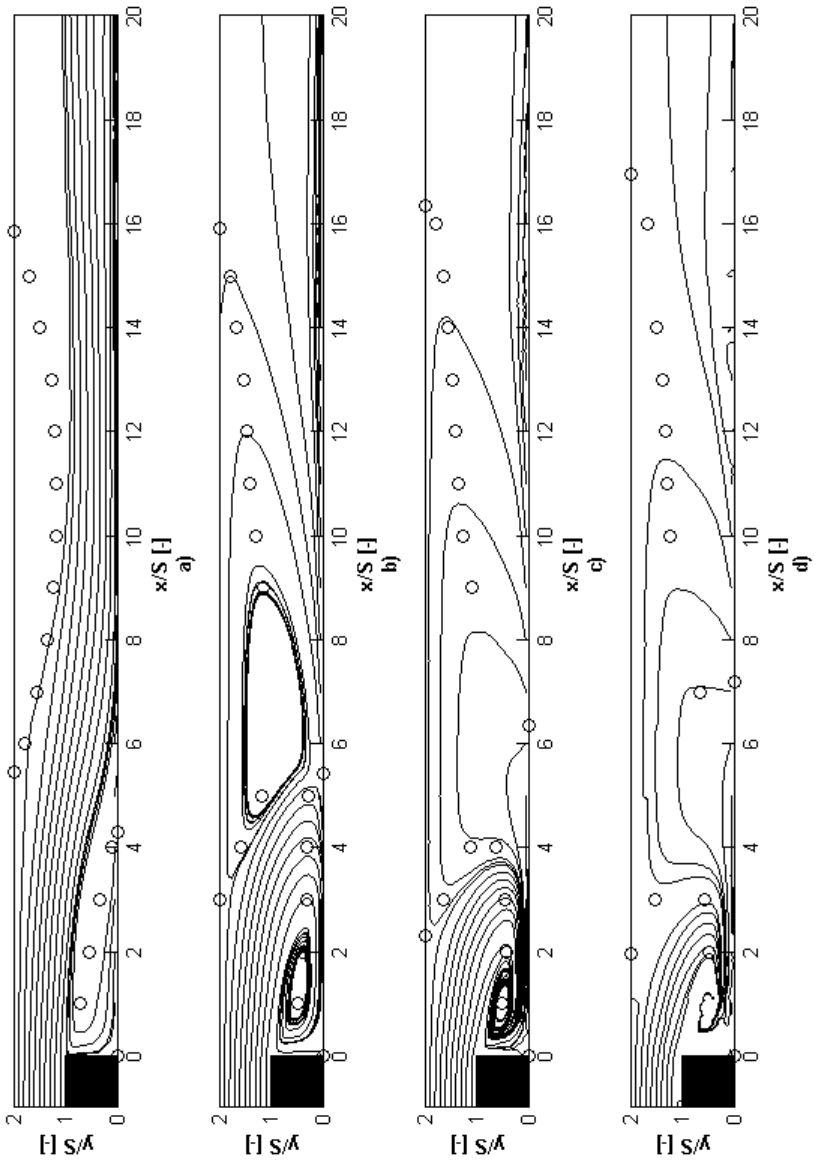

Figure 4.25. The 'xy'-plane streamlines (black dashed lines) and contours of streamwise velocity demonstrating the sidewall effect $AR = 33.2$ and $Re = 476$. Circles mark position in chosen distances from step edge where streamwise velocity is zero. a) 'xy'-plane $z/b = 0.4655$, b) 'xy'-plane $z/b = 0.4895$, c) 'xy'-plane $z/b = 0.4955$, d) 'xy'-plane $z/b = 0.4985$.

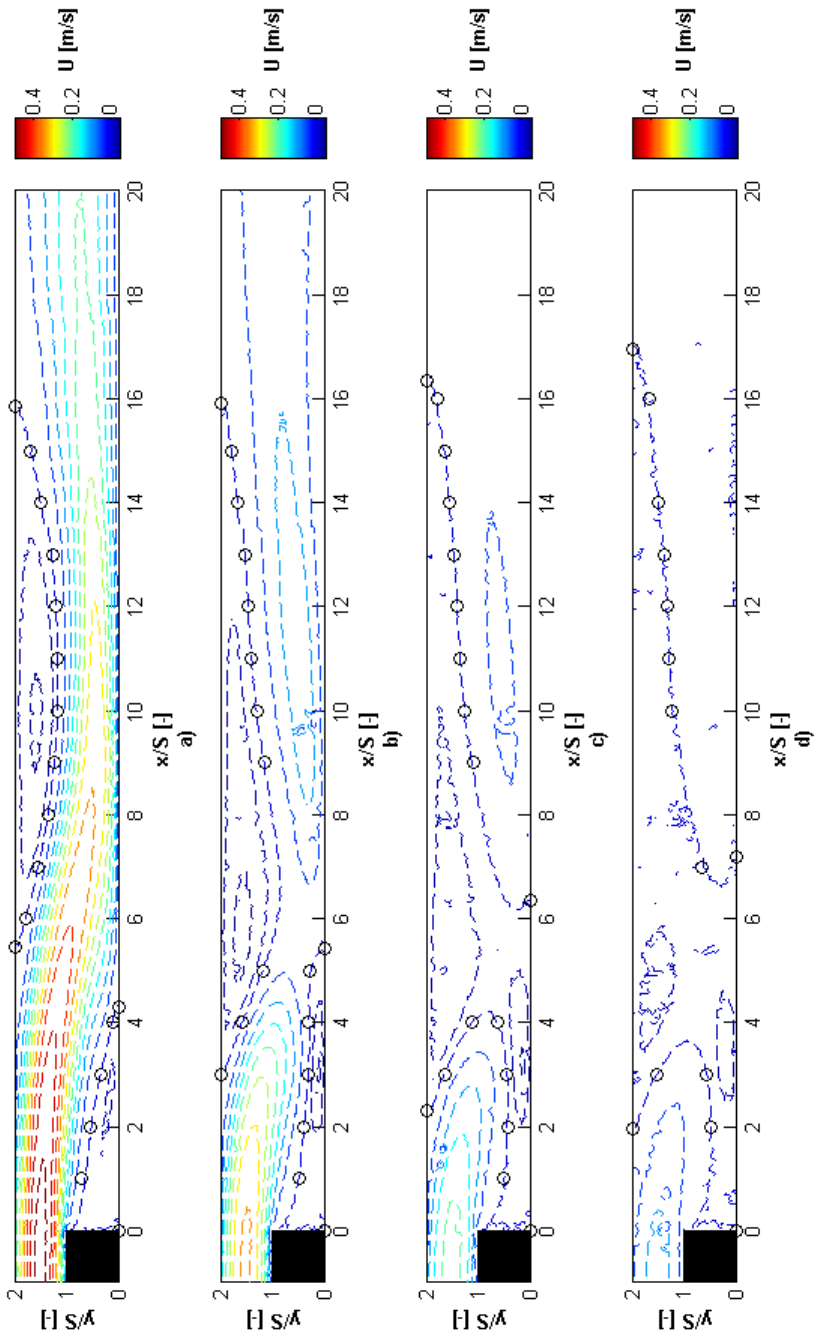

Figure 4.26. The 'xy'-plane contours of streamwise velocity demonstrating the sidewall effect AR = 33.2 and Re = 506. Circles mark position in chosen distances from step edge where streamwise velocity is zero. a) 'xy'-plane z/b = 0.4655 δ_{sw}/S = 1.15, b) 'xy'-plane z/b = 0.4895 δ_{sw}/S = 0.35, c) 'xy'-plane z/b = 0.4955 δ_{sw}/S = 0.15, d) 'xy'-plane z/b = 0.4985 δ_{sw}/S = 0.05.

wise direction towards the exit section. The streamlines between step edge and the reattachment point follow the spiral motion inside the primary recirculation flow region. The streamlines originating between reattachment point and $x/S \approx 7.1$ flow in the streamwise direction and simultaneously bend toward the upper wall where they sharply bend in the upstream direction, flow along the upper wall and supply the secondary recirculation flow region. The streamlines originating from the point further downstream flow downstream towards the exit section.

c) The incoming flow from the section $z/b = 0.4955$ bends downwards the bottom plane with a vortex motion inside the primary recirculation flow region Fig. 4.25 c) and 4.26 c). The stream particles originating between reattachment point and $x/S \approx 9$ move sharply towards the top wall where it bends back in the upstream direction and flows along the top wall up to zero streamwise velocity contour that represents separation point at the top wall where it bends downwards the bottom wall, ending in a spiral vortex motion inside the primary recirculation flow region. The other streamlines continue in the downstream direction.

d) The flow situation is very similar to the case ad c) in the section adjacent to the sidewall $z/b = 0.4985$ as depicted in Fig. 4.25 d) and 4.26 d), where the upward motion of the fluid after the reattachment point proceeds faster and thus the fluid moves closer to the top wall after $x/S > 14$.

In all presented cases no information about the spanwise velocity component was obtained because the simple two-dimensional PIV was utilized. Comparing the presented images it is obvious that the flow is not simply two-dimensional but there must be strong spanwise motion transporting the fluid from sections far from sidewall towards the sidewall in positions after the reattachment point. This fluid then moves rapidly towards the upper recirculation flow region where it turns in the upstream direction and than downwards to supply the primary recirculation flow region between step and the reattachment point. Because no evidence that the incoming flow from the inlet section continues downstream towards the exit section in 'xy' planes adjacent to sidewall, but moves spirally inside the primary recirculation flow region, it seems apparent that the flow inside the primary recirculation flow region has to flow from sidewalls towards the symmetry plane.

4.5. Streamwise variation of reattachment length

The reattachment is highly dynamical process, i.e., the previously described reattachment lines only represent the average location of the reattachment point. An investigation of the minimum and maximum distance from the step edge, where the reattachment takes place, was performed. Here the forward-flow-fraction was calculated; the minimum and the maximum reattachment length was detected as points where $\gamma_p = 0$ and $\gamma_p = 1$, respectively. Fig. 4.27 through 4.29 show spanwise distributions of the reattachment length at the bottom plane. The time average reattachment length is depicted as full circles (●), minimum reattachment point distance (▷) and maximum reattachment point distance (◁). Fig. 4.30 through 4.32 show length of the reattachment zone.

It appears that the length of reattachment zone grows as the Reynolds number is increased, however, the maximum occurs approximatelly around $Re \approx 920$ (see Fig. 4.32) and

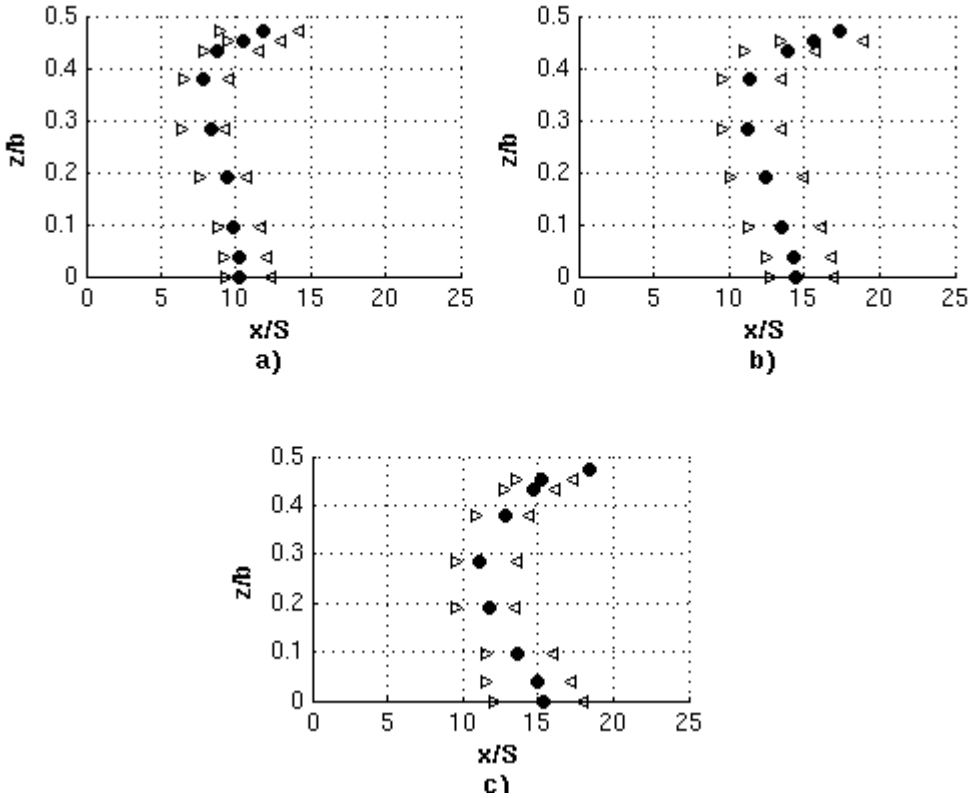

Figure 4.27. Spanwise distributions of time average reattachment point (●), minimum reattachment length distribution (▷) and maximum reattachment length distribution (◁) in channel with $AR = 5.3$ adjacent to the bottom plane $y/S = 0.3081$. a) $Re = 437$, b) $Re = 874$, c) $Re = 1084$.

then it decreases. In the case of small aspect ratio $AR = 5.3$, the length of the reattachment zone is almost constant over the entire span except in the vicinity of the sidewall, where it rises (see Fig. 4.30). The length of the reattachment zone is higher near the symmetry plane than in the vicinity of the sidewall, when the aspect ration is $AR = 17.3$ and $AR = 33.2$ (Fig. 4.31 and 4.32). However, in the case of aspect ratio $AR = 33.2$, the length of the reattachment zone has its maxima in the zone, where the time average reattachment length reaches maximum length (see Fig. 4.29).

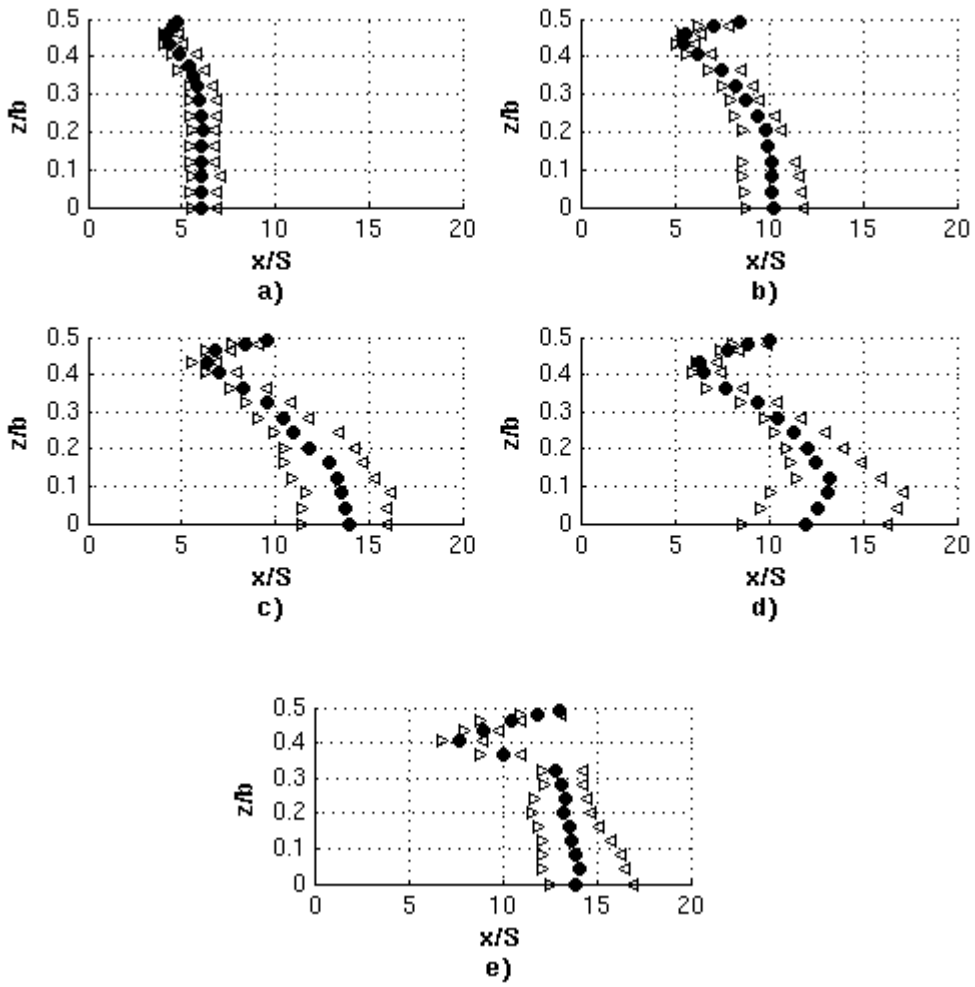

Figure 4.28. Spanwise distributions of time average reattachment point (●), minimum reattachment length distribution (▷) and maximum reattachment length distribution (◁) in channel with $AR = 17.3$ adjacent to the bottom plane $y/S = 0.3081$. a) $Re = 256$, b) $Re = 476$, c) $Re = 681$, d) $Re = 905$, e) $Re = 1165$.

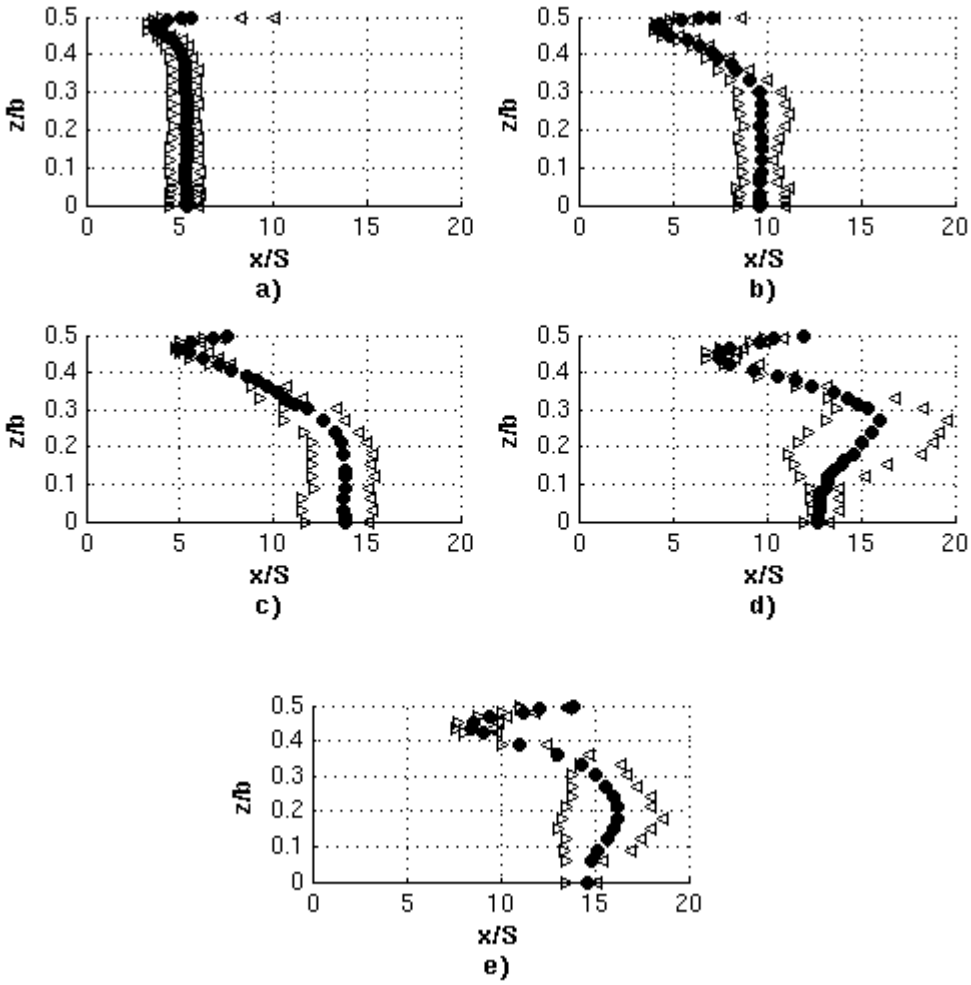

Figure 4.29. Spanwise distributions of time average reattachment point (●), minimum reattachment length distribution (▷) and maximum reattachment length distribution (◁) in channel with $AR = 33.2$ adjacent to the bottom plane $y/S = 0.3081$. a) $Re = 218$, b) $Re = 465$, c) $Re = 679$, d) $Re = 905$, e) $Re = 1179$.

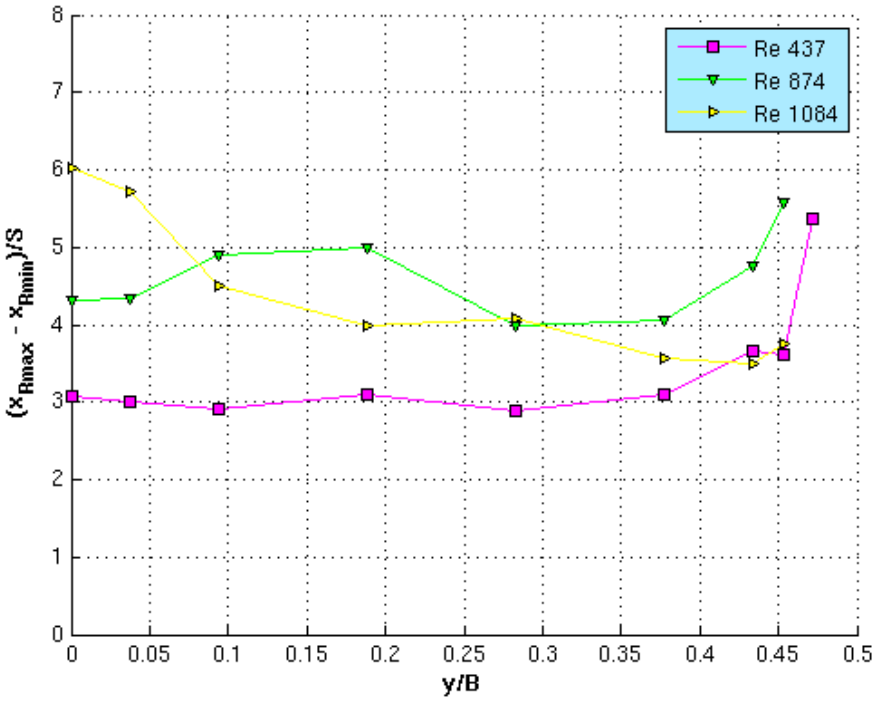

Figure 4.30. Length of the reattachment zone, aspect ratio $AR = 5.2$.

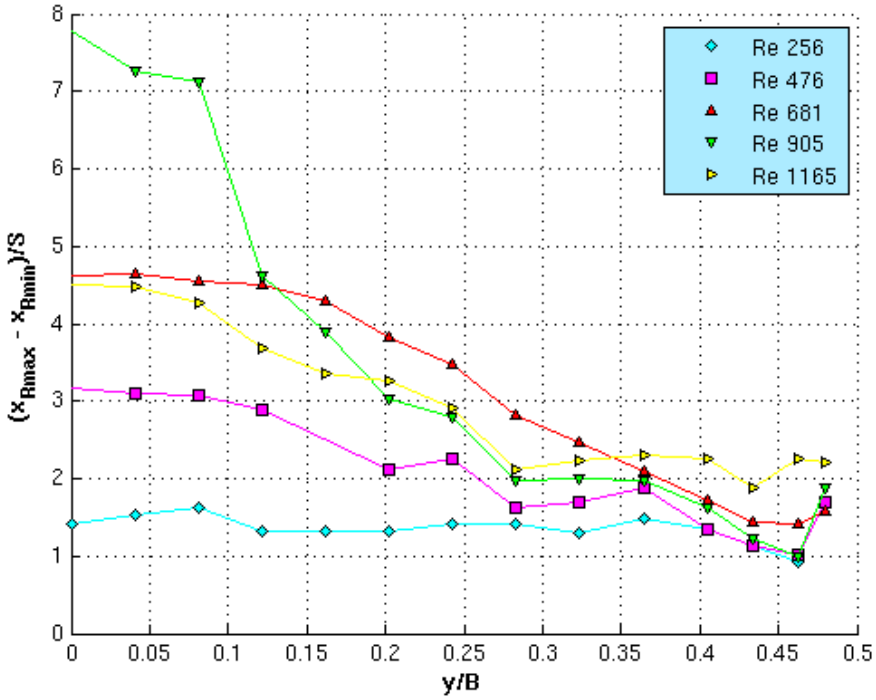

Figure 4.31. Length of the reattachment zone, aspect ratio $AR = 17.2$.

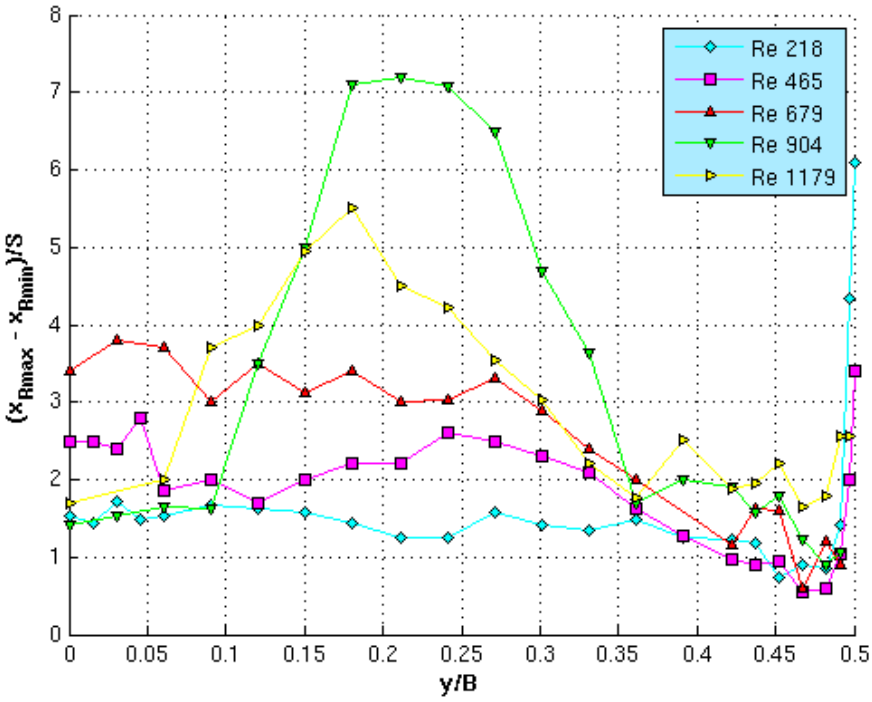

Figure 4.32. Length of the reattachment zone, aspect ratio $AR = 33.2$.

4.6. Numerical solution

Figure 4.33 presents velocity profiles at the symmetry plane $z/b = 0$ and at upstream distance $x/S = -1$. Comparison shows good compliance for all Reynolds numbers. Spanwise velocity profiles in the horizontal middle plane $y/S = 1.5$ and at the upstream distance $x/S = -1$ are depicted in Figure 4.34. They are in good conformity with experimental data for Reynolds numbers below 680; for higher Reynolds numbers they show higher values near the sidewalls, however, they remain symmetric for all simulated Reynolds numbers. For results of other aspect ratios see Appendix A

Numerical simulation slightly over predicts the reattachment length for Reynolds numbers lower $Re < 700$; the higher the Reynolds number the higher the over prediction (see Fig. 4.35, 4.37 and 4.39). The over prediction is approximately one step height long near the symmetry plane and higher near the sidewalls when $Re \approx 460$. However, the shape of the reattachment line shows good resemblance with the experimental data for all aspect ratios and no asymmetry is observed. In the case of aspect ratio $AR = 33.2$, the predicted reattachment length is slightly longer near the ends of the "two dimensional zone" near the symmetry plane than the experimental results (Fig. 4.39).

The over prediction of the reattachment length at the symmetry plane about six step heights for aspect ratio $AR = 5.3$ when $Re = 874$ (Fig. 4.35). In the case of aspect ratio $AR = 17.3$, the shape of the reattachment line does not correspond with the experimental data, since the numerical simulation predicts longest reattachment length near the symmetry plane (except the vicinity of sidewalls) while the experiment indicates longest reattachment length approximately around $z/b \approx 0.1$ (Fig. 4.37). Both numerical and experimental results indicate longest reattachment length at the ends of "the two dimensional zone" when the aspect ratio is $AR = 33.2$ (Fig. 4.39), however, the difference between the local minimum at the symmetry plane and the maximum is almost two step heights for experimental data while approximately half of the step height for numerical simulation. Also the spanwise location of the maximum reattachment length differs, since the numerical simulation predicts the maximum closer to the symmetry plane.

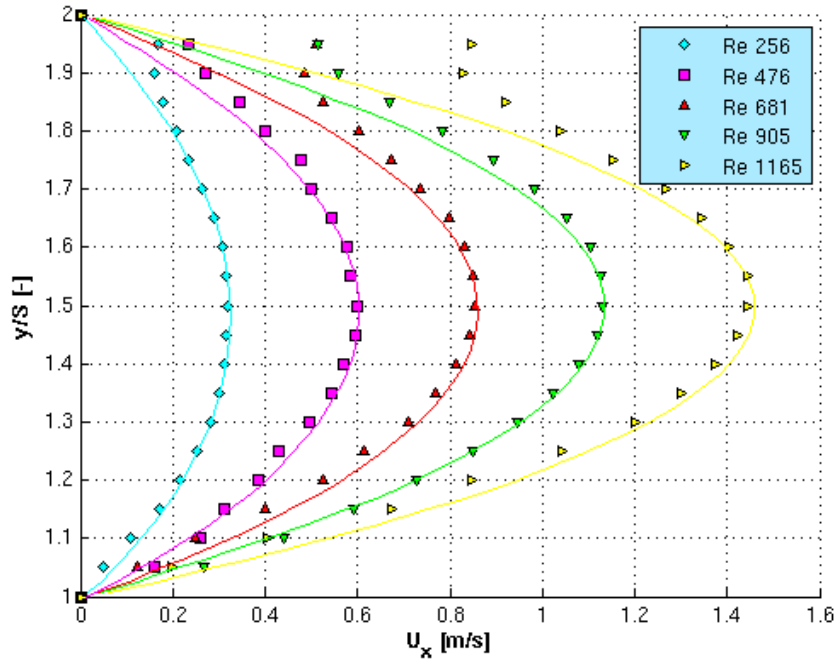

Figure 4.33. Velocity profiles at the symmetry plane $z/b = 0$, at upstream distance $x/S = -1$, aspect ratio $AR = 17.3$. Symbols stay for experimental data, full lines for corresponding numerical simulation.

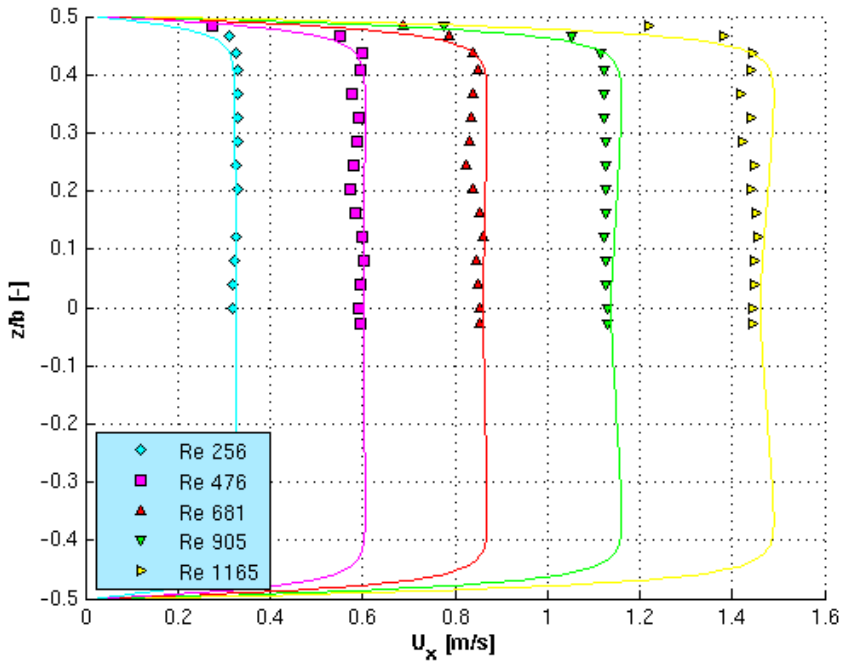

Figure 4.34. Spanwise velocity profiles in the horizontal middle plane $y/S = 1.5$, at upstream distance $x/S = -1$, aspect ratio $AR = 17.3$. Symbols stay for experimental data, full lines for corresponding numerical simulation.

Further increase of the Reynolds number results in a drop of the reattachment length and in the loss of the symmetry of the reattachment profile in channels with aspect ratio $AR = 5.3$ and 17.3, (see Fig. 4.35 and 4.37).

Numerical simulation well predicts location of separation points of the secondary recirculation flow region adjacent to the top wall (see Fig. 4.36, 4.38 and 4.40). Larger secondary recirculation flow region is predicted for Reynolds number around $Re \approx 220$ for aspect ratios $AR = 5.3$ and 17.3. Location of reattachment of the secondary recirculation flow region is well predicted for Reynolds number around $Re \sim 450$ for all aspect ratios. When the Reynolds number is higher than 650, the reattachment line of the secondary recirculation flow region is located further in the downstream direction than indicates the experiment, except the case of the highest simulated Reynolds number in channel with aspect ratio $AR = 5.3$ (Fig. 4.36). The maximum width of the secondary recirculation flow region that extends from the sidewall towards the symmetry plane is larger than the experimental when $Re \sim 670$ and 900 except the results in channel with aspect ratio $AR = 17.3$ (Fig. 4.38).

Secondary recirculation flow region near the symmetry plane is already predicted for $Re = 679$ when aspect ratio $AR = 33.2$ (Fig. 4.40), what is in a contrary to the experimental results, where the secondary recirculation flow region firstly appears for Reynolds numbers higher than $RE > 900$. It is still separated from the recirculation flow regions adjacent to the sidewalls, however, single secondary recirculation flow region is predicted when the Reynolds number is $Re = 904$. No secondary recirculation flow region near the symmetry plane was predicted in channels with aspect ratios $AR = 5.3$ and 17.3 at any simulated Reynolds number.

Visualisation of vortices in channel with aspect ratio $AR = 5.3$ reveals pair of streamwise vortices adjacent to the sidewalls and top wall, that starts in the vertical middle of the inlet section, approximately at the step edge and continues downstream up to the location with shortest distance of reattachment point, where the vortical structure expands in vertical direction (Fig. 4.41). Another pair of streamwise vortices forms near the point of shortest distance of reattachment point and continues near the bottom wall in the downstream direction. When the Reynolds number is higher than $Re > 850$, small vortical structures

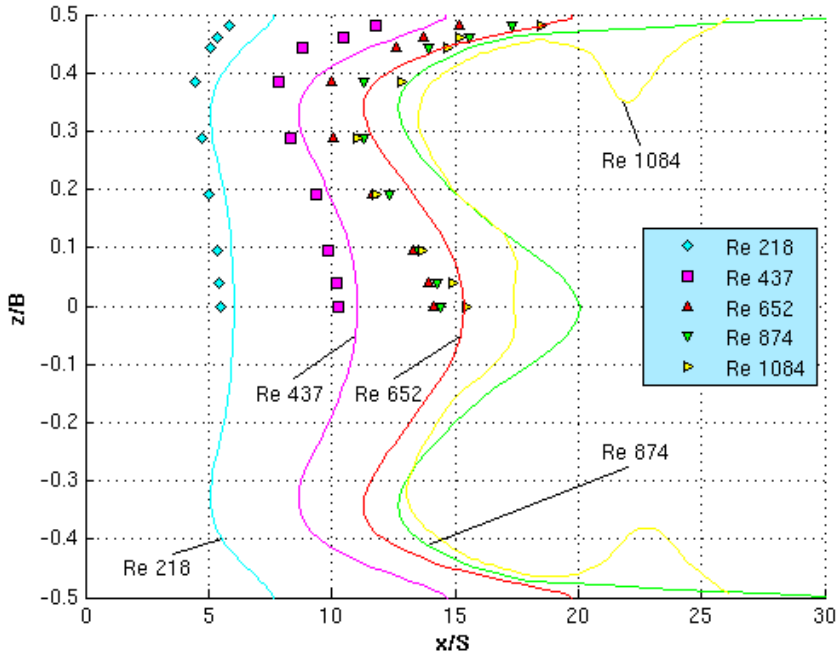

Figure 4.35. Experimental (symbols) locations of reattachment line at the bottom plane compared with numerical solution (full lines), aspect ratio $AR = 5.3$.

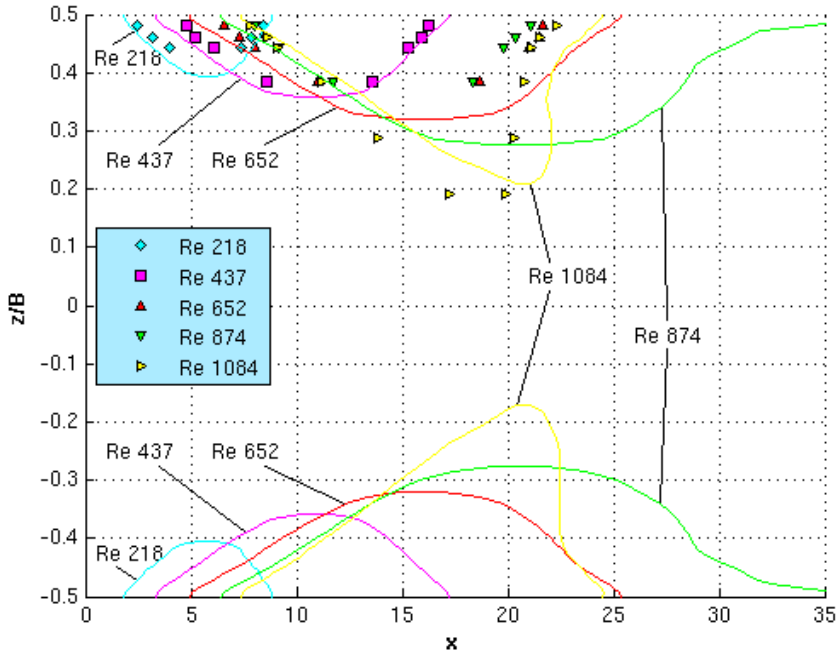

Figure 4.36. Experimental (symbols) locations of secondary recirculation flow region at the top plane compared with numerical solution (full lines), aspect ratio $AR = 5.3$.

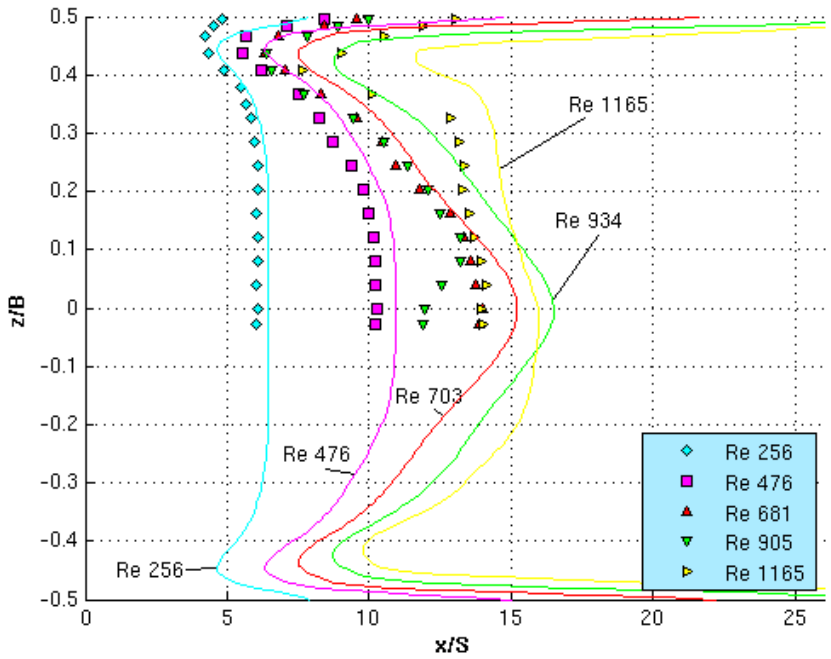

Figure 4.37. Experimental (symbols) locations of reattachment line at the bottom plane compared with numerical solution (full lines), aspect ratio $AR = 17.3$.

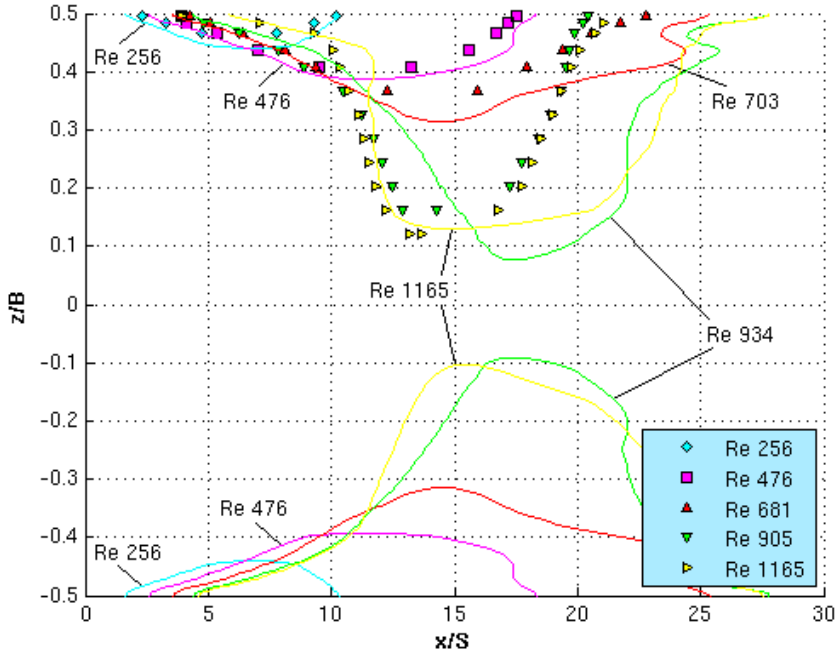

Figure 4.38. Experimental (symbols) locations of secondary recirculation flow region at the top plane compared with numerical solution (full lines), aspect ratio $AR = 17.3$.

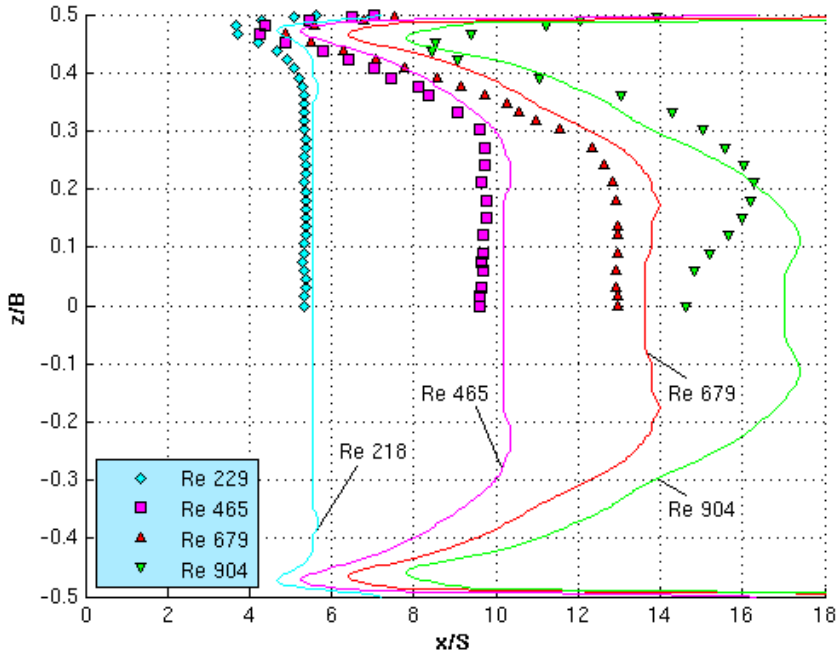

Figure 4.39. Experimental (symbols) locations of reattachment line at the bottom plane compared with numerical solution (full lines), aspect ratio $AR = 33.2$.

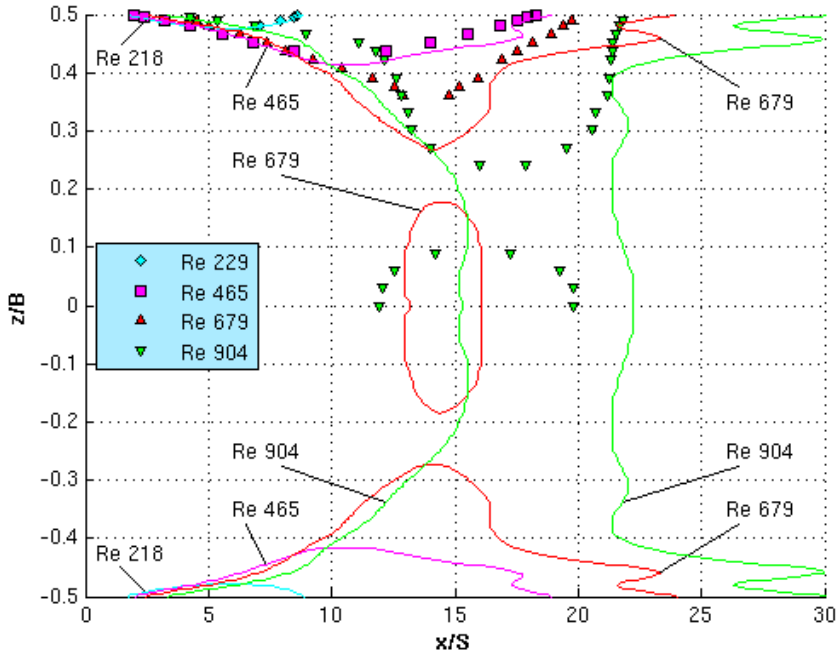

Figure 4.40. Experimental (symbols) locations of secondary recirculation flow region at the top plane compared with numerical solution (full lines), aspect ratio $AR = 33.2$.

form at streamwise distance $x/S \approx 30$; approximately near the location of the downstream end of the secondary flow region and fill the whole flow domain (Fig. 4.42).

Similar situation appears in channel with aspect ratio $AR = 17.3$, however the vortical structure near the reattachment of primary recirculation flow region is more complex and expands further towards the channel symmetry plane[1]. These large vortical structures adjacent to the sidewalls break down into small structures approximately at downstream distance $x/S \approx 20$ and continue in the downstream direction near the sidewalls up to $x/S \approx 40$ (Fig. 4.43), when the Reynolds number is increased up to $Re = 905$. At the same Reynolds number, third zone of small vortical structures forms in the middle of the channel slightly upstream the location of the largest distance of reattachment point. These vortices then expand in the spanwise direction as they continue in the streamwise direction (Fig. 4.43). When the Reynolds number is further increased up to $Re = 1165$, the symmetry is lost and the zone of small vortical sturcutres that forms "near" the symmetry plane joins the vortical structures near the sidewalls, while it almost dissappear near the symmetry plane (Fig. 4.44).

Large vortical structure near the secondary recirculation flow region adjacent to the top plane was observed in the channel with aspect ratio $AR = 33.2$ (Fig. 4.45). Similar to previous cases, pair of streamwise vortices starts in the vertical middle of the inlet section, approximately at the step edge and continues downstream; this pair later transforms into more complex vortical structure near the shortes distance of reattachment point. Unlike from previous cases, only very short zone of small vortical structures forms after the break down of these larger structures.

[1]It should be noted, that the size of visualized λ_2 isosurfaces depends on the value of λ_2 that was chosen for visualisation of the vortical structures.

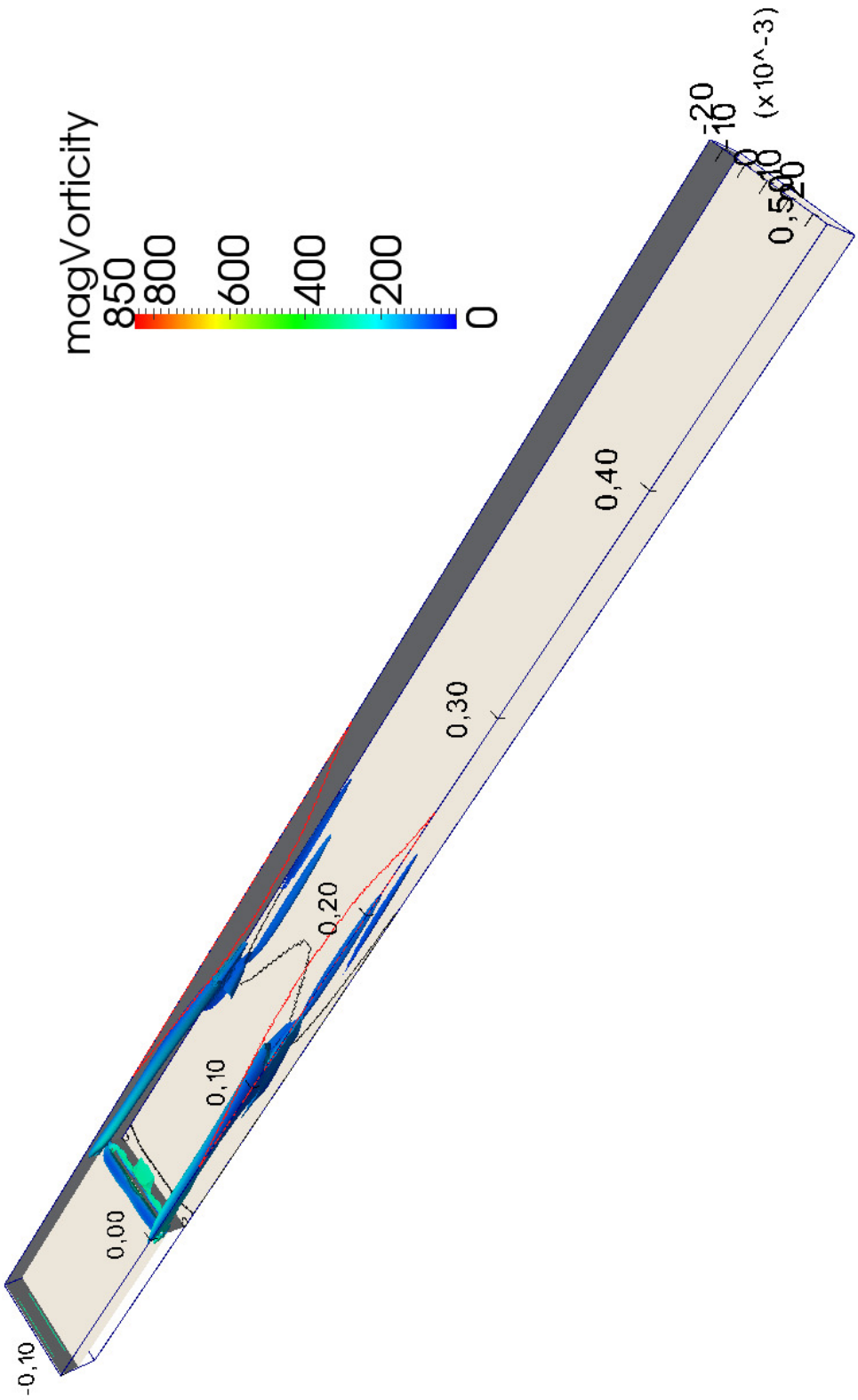

Figure 4.41. Visualization of vortices - isosurfaces at $\lambda_2 = -100$. Colors by vorticity magnitude; aspect ratio $AR = 5.3$, $Re = 652$. Black line denotes reattachment line of the primary recirculation flow region; red line ilustrates secondary flow region projected on the upper wall.

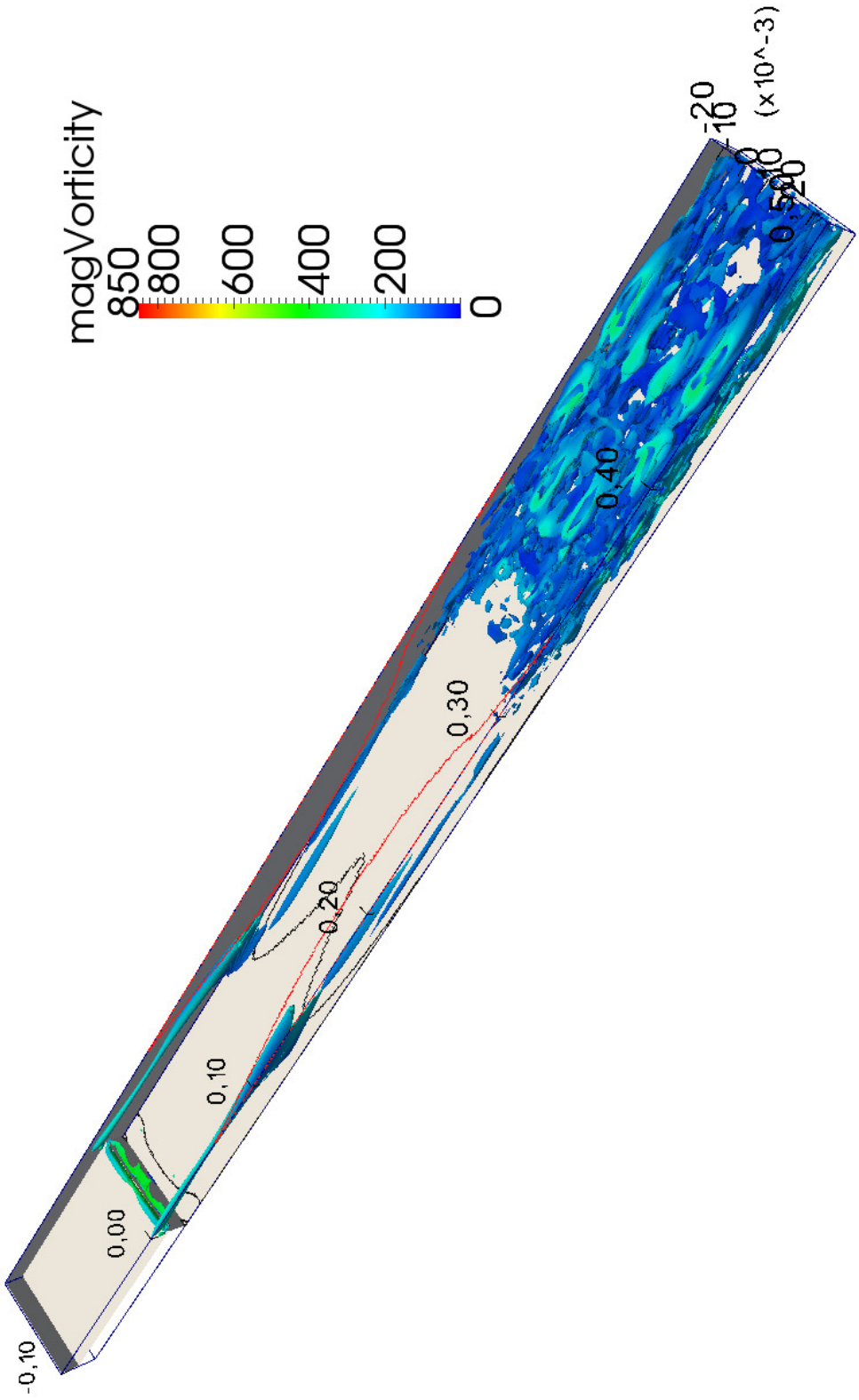

Figure 4.42. Visualization of vortices - isosurfaces at $\lambda_2 = -300$. Colors by vorticity magnitude; aspect ratio $AR = 5.3$, $Re = 874$. Black line denotes reattachment line of the primary recirculation flow region; red line ilustrates secondary flow region projected on the upper wall.

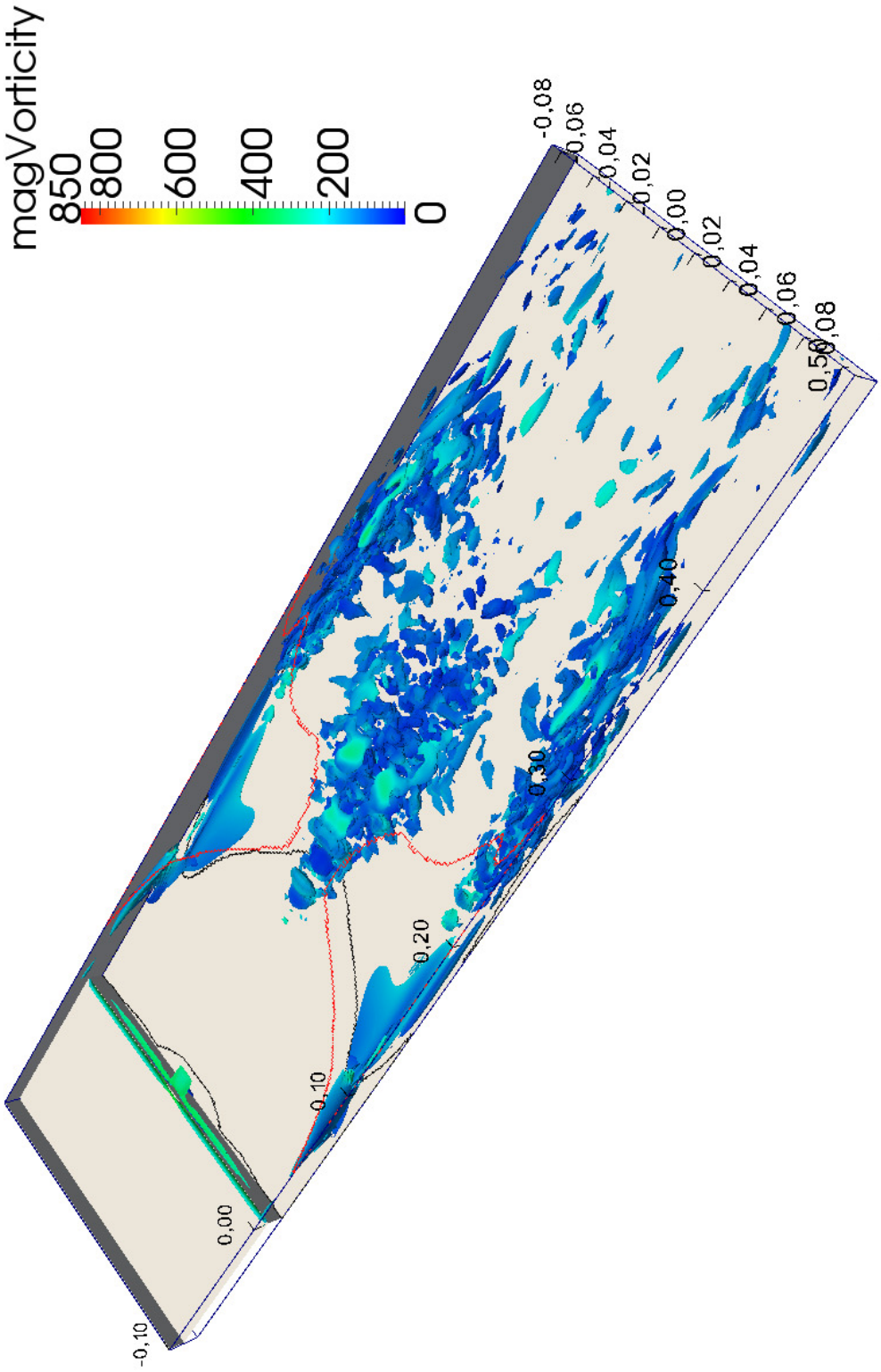

Figure 4.43. Visualization of vortices - isosurfaces at $\lambda_2 = -400$. Colors by vorticity magnitude; aspect ratio $AR = 17.3$, $Re = 905$. Black line denotes reattachment line of the primary recirculation flow region; red line ilustrates secondary flow region projected on the upper wall.

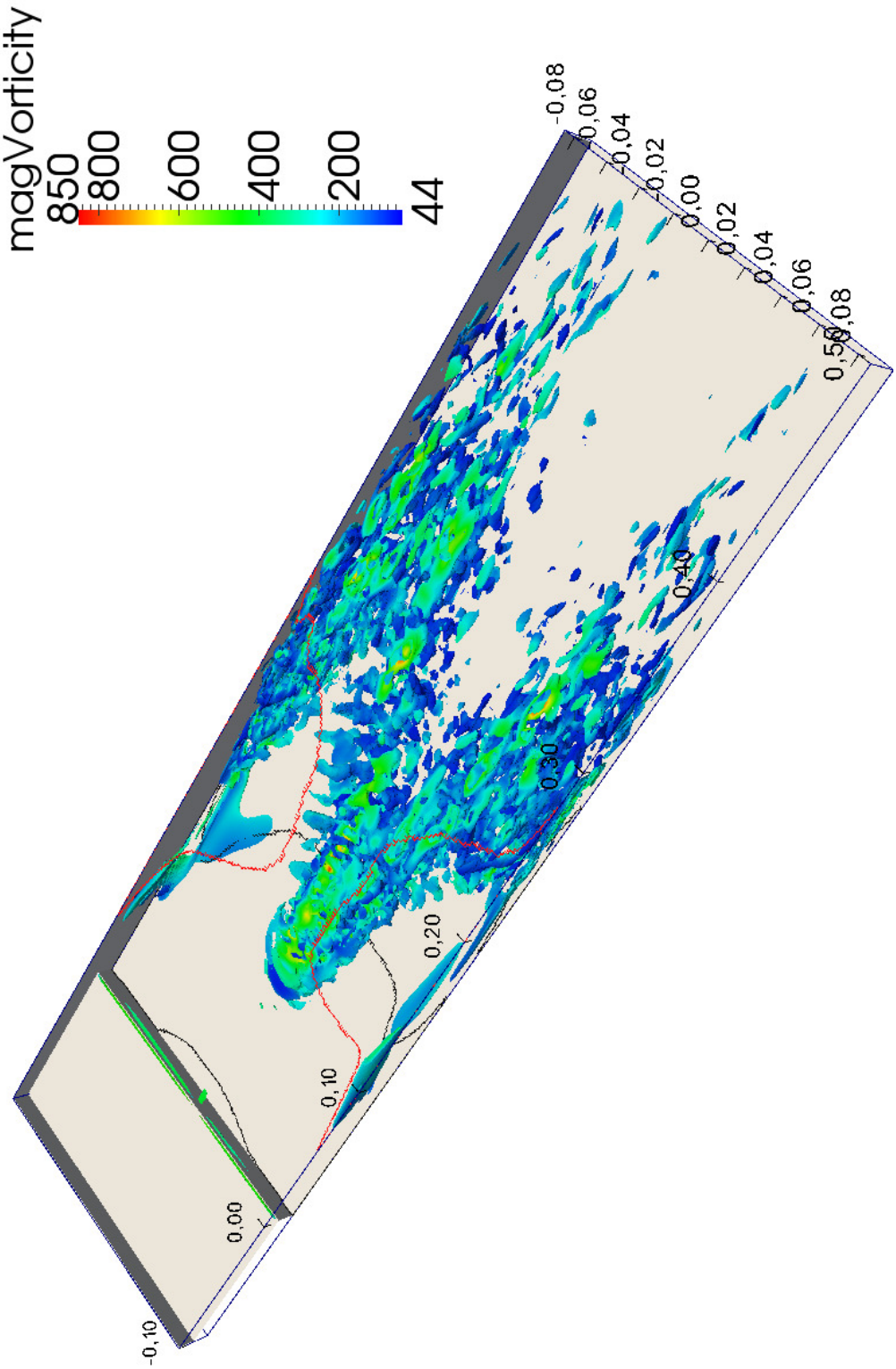

Figure 4.44. Visualization of vortices - isosurfaces at $\lambda_2 = -1000$. Colors by vorticity magnitude; aspect ratio $AR = 17.3$, $Re = 1165$. Black line denotes reattachment line of the primary recirculation flow region; red line ilustrates secondary flow region projected on the upper wall.

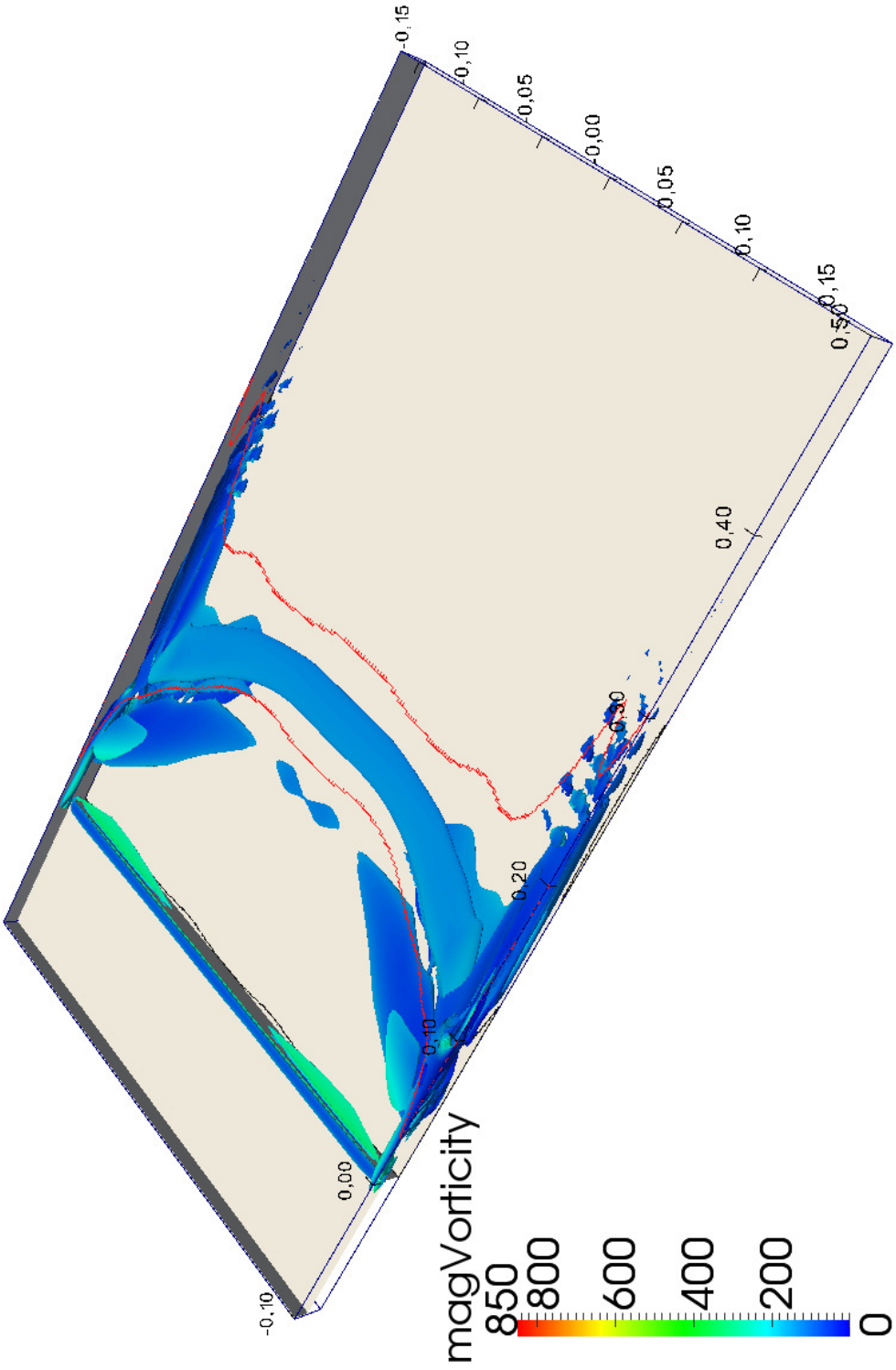

Figure 4.45. Visualization of vortices - isosurfaces at $\lambda_2 = -100$. Colors by vorticity magnitude; aspect ratio $AR = 33.2$, $Re = 904$. Black line denotes reattachment line of the primary recirculation flow region; red line ilustrates secondary flow region projected on the upper wall.

Chapter 5. Conclusion

Measurements in four channels of different aspect ratios $AR = 5.3$; 8; 17.3 and 33.2 were performed using the Particle Image Velocimetry method (PIV). Reattachment length at the symmetry plane was measured for Reynolds numbers from 50 up to 2500. Half of the channel was scanned at several Reynolds numbers in order to obtain information about the development of the flow past the backward-facing step with increasing Reynolds number.

The reattachment length at the symmetry plane steadily increases in the initial phase in all channels (Fig. 4.11). The trend of the reattachment length curve in the widest channel with aspect ratio $AR = 33.2$ remains almost constant up to the maximum reattachment length $x_1/S = 18.2$ at $Re = 1183$; after this point the reattachment length suddenly drops and remains constant within the measured range of Reynolds numbers. The same is not true for narrow channels with aspect ratio $AR = 5.3$; 8 and 17.3. The trend of the reattachment length curve is steeper up to Reynolds number $Re \approx 681$ for $AR = 5.3$ and up to $Re = 561$ for $AR = 8$ than in channel with aspect ratio $AR = 33.2$; here the transitional regime probably begins and the reattachment length increases less steeply til the maximum rettachment length is reached at $x_1/S = 16.7$ and 16.5 with corresponding Reynolds numbers 1837 and 1444 for $AR = 5.3$ and 8, respectively. After the maximum reattachment length is reached, the reattachment length begins to drop as the Reynolds number is further increased. It seems, that the narrower the channel the higher the Reynolds number at which the maximum reattachment length at the symmetry occurs.

On the contrary to all other results, the reattachment length for $AR = 17.3$ drops around $Re \approx 681$ (see Fig. 4.12); decreases its length from $x_1/S = 14.5$ back to value ≈ 12 at $Re \sim 905$ and then again rises less steeply up to maximum reattachment length $x_1/S = 16$ at $Re = 1399$. Similar as in channels with $AR = 5.3$ and 8 no sudden drop after the maximum reattachment length was observed, but the reattachment length was slowly falling.

Spanwise distribution of reattachment length indicates minimum reattachment length near the sidewalls with distance from the sidewall varying between 0.7 S to 1.8 S; the max-

imum is in most cases located at the symmetry plane. The maximum reattachment length is located approximately at $z/b = 0.1$ in the case of $AR = 17.3$ and $Re = 905$ (see Fig. 4.15), however it is unclear if this is shift of the maximum reattachment length towards the sidewall, away from the symmetry plane or if it also occurs in second half of the channel symmetric with the symmetry plane. In the case of channel with $AR = 33.2$ and for higher Reynolds numbers 904 and 1173 (see Fig. 4.16), the maximum reattachment length is located approximately at $z/b = 0.25$; at the same spanwise location no secondary recirculation flow region is observed on the top plane.

No observation of "two-dimensional zone" near the symmetry plane (based on the constant spanwise distribution of reattachment length) was made for channels with $AR = 5.3$ (Fig. 4.13) and 8 (Fig. 4.14). This "two-dimensional zone" was observed in channels with $AR = 17.3$ and 33.2 for Reynolds numbers smaller than 476 and 679, respectively. However, based on current measurements it cannot be concluded what is the highest Reynolds numbers at which this "two-dimensional zone" can be observed.

A secondary recirculation flow region was detected adjacent to the corner between top wall and sidewalls (Figures 4.17 through 4.19). It has a lencitcular shape on the top wall for Reynolds numbers below approximately $Re < 680$ and all measured aspect ratios; spanwise and streamwise dimension of this recirculation bubble increases as the Reynolds number is increased and its streamwise location moves downstream from the step edge so, that the maximum spanwise dimension is approximately at the same distance as the location of reattachment point of the primary recirculation flow region at the symmetry plane. The secondary recirculation flow region emanates approximately from the middle of the sidewall, e.g., $y/S = 1$ and rapidly shrinks its vertical size.

At higher Reynolds numbers, the secondary recirculation flow region abruptly expands in the spanwise direction, however its vertical size in this expanded zone remains almost constant, approximately only quarter of the vertical size in the initial, lenticular region. No prove of secondary recirculation flow region near the symmetry plane was observed for channels with aspect ratio $AR = 5.3$; 8 and 17.3 (see Figures 4.17 through 4.18). On the contrary, in the channel with aspect ratio $AR = 33.2$ and for Reynolds numbers 905 and 1179 (see Fig. 4.19) two separated secondary recirculation flow regions were ob-

served (counting both secondary recirculation flow regions on both sides as the first zone). One was the initial zone adjacent to the sidewall, which was interrupted approximately at $z/b = 0.3$, and the second one, that forms in the vicinity of the symmetry plane. Maximum of the reattachment length of the primary recirculation flow region was observed in the gap between these two secondary recirculation flow regions. However, it remains unclear if there is recirculation zone also between these two zones, since this zone could be smaller than the resolution of interrogation window used.

Since the location of reattachment was not constant, a streamwise variation of the reattachment point, i.e., the difference between maximum and minimum reattachment length, was observed (see Fig. 4.27 through 4.29). It is constant over whole span for very small Reynolds numbers and all aspect ratios (Figures 4.30 through 4.32). Constant value was also observed at higher Reynolds number approximately in the zone, where the flow was like two-dimensional, i.e., near the symmetry plane; here the streamwise variation was slightly higher than in the rest of the channel span. Minimum is observed in the zone where the minimum of reattachment length was measured. The streamwise variation of reattachment length in channels of aspect ratio $AR = 17.3$ and 33.2 and at high Reynolds numbers showed extremely high values in zone where the maximum of reattachment length was observed, almost two to three times higher than in the rest of the channel (Fig. 4.31 and 4.32).

Numerical simulation slightly over predicts the reattachment length for Reynolds numbers below $Re < 700$ (see Fig. 4.35, 4.37 and 4.39); the over prediction is about one step height near the symmetry plane at $Re = 460$ and higher near the sidewalls, but increases with Reynolds number. The shape of the predicted reattachment line is in good resemblance with experimental results for all aspect ratio without any asymmetry. Slightly longer reattachment length was observed near the ends of the "two dimensional zone" in numerical simulation in channel with aspect ratio $AR = 33.2$.

The over prediction is higher for higher Reynolds numbers; about six step heights in the channel with aspect ratio $AR = 5.3$ and at Reynolds number $Re = 874$ (Fig. 4.35). The shape of the predicted reattachment line does not correspond with the experimental data in the case of aspect ratio $AR = 17.3$ for higher Reynolds number, since the numerical

simulation predicts longest reattachment length at the symmetry plane while experiment indicates longest reattachment length near $z/b = 0.1$ (see Fig. 4.37). Both experimental and numerical results indicate longer reattachment length near the ends of the "two dimensional zone" near the symmetry plane in channel with aspect ratio $AR = 33.2$ (Fig. 4.39), however the numerical simulation predicts the maximum closer to the symmetry plane and smaller "burst" than the experimental results.

Secondary recirculation flow region adjacent to the top wall is well predicted for Reynolds numbers below $Re < 480$ (see Fig. 4.36, 4.38 and 4.40). Separation line of the secondary recirculation flow region is also well predicted for higher Reynolds numbers. The reattachment line is predicted further downstream than indicates the experiment. Secondary recirculation flow region near the symmetry plane separated from the main recirculation zones, that are adjacent to the sidewalls, was already predicted for $Re = 679$ in channel with aspect ratio $AR = 33.2$ (Fig. 4.40), contrary to the experimental results (Fig. 4.19). Single secondary recirculation flow region over the whole spanwise is predicted for $Re = 904$. No secondary recirculation flow region near the symmetry plane was predicted for channels with aspect ratio $AR = 5.3$ and 17.3 (Figures 4.36 and 4.38).

Visualisation of vortices revealed pair of vortical structures that start in the vertical middle of the inlet section, approximately at the step edge, and continue to the location of reattachment of the primary recirculation flow region, where the vortical structure expands in the vertical direction (Fig. 4.41). Another vortical structure forms near the side walls, after the reattachment point and continues downstream the channel; it later breaks down when Reynolds number is higher than $Re > 850$ and whole cross section is filled with small vorticesi (Fig. 4.42). Strong vortical structures were detected near the sidewalls and near the symmetry plane for higher Reynolds numbers in channel with aspect ratio $AR = 17.3$ (Fig. 4.44). Weak vortical structures past the reattachment of the primary recirculation flow region, were observed near sidewalls in channel with aspect ratio $AR = 33.2$ (see Fig. 4.45). Compact vortex near the secondary recirculation flow region adjacent to the top wall was observed in channel with aspect ratio $AR = 33.2$ at Reynolds number $Re = 904$.

Generally it can be concluded, that the flow situation past the step is for low Reynolds numbers similar in all examined channels, since the maximum reattachment length is

observed at the symmetry plane. Moreover, in channels with high aspect ratio $AR = 17.3$ and 33.2 constant reattachment length near the symmetry plane was observed, suggesting "two dimensional zone" in this region. The resemblance between narrow and wide channels is lost for higher Reynolds numbers, where the effect of sidewalls in narrow channels ($AR = 5.3$ and 8) does not dramatically change the shape of reattachment lines as well as the shape of the secondary recirculation flow region remain similar, yet it only becomes larger. The sidewall effect in wide channels ($AR = 17.3$ and 33.2) results in a loss of the "two dimensionality" of the flow near the symmetry plane; the wider the channel, the later the loss of the symmetry occurs. However, it is unclear if the flow in sufficiently wide channel would remain "two dimensional" near the symmetry plane even for higher Reynolds numbers, since the projection of the maximum width of the "two dimensional flow zone" suggest, that the loss of the "two dimensionality" should take place at higher Reynolds number than it in fact occurs in the widest examined channel with aspect ratio $AR = 33.2$. Also the flow situation in channel with aspect ratio $AR = 17.3$ around Reynolds number 905 can not be fully elucidated just based on measurements conducted only in half of the channel, since it is unclear if the flow is still symmetric or if the bulk flow is slightly deflected towards one of the sidewalls resulting in shorter reattachment length at the symmetry plane.

The information about the third velocity component can play important if not fundamental role in full elucidation of the loss of the "two dimensionality" of the flow near the symmetry plane. This factor together with measurements in whole span of the channel is the territory on which a future experiments can focus and where modern volumetric measurements methods like tomography PIV can be applied.

Appendix A. Inlet velocity profiles

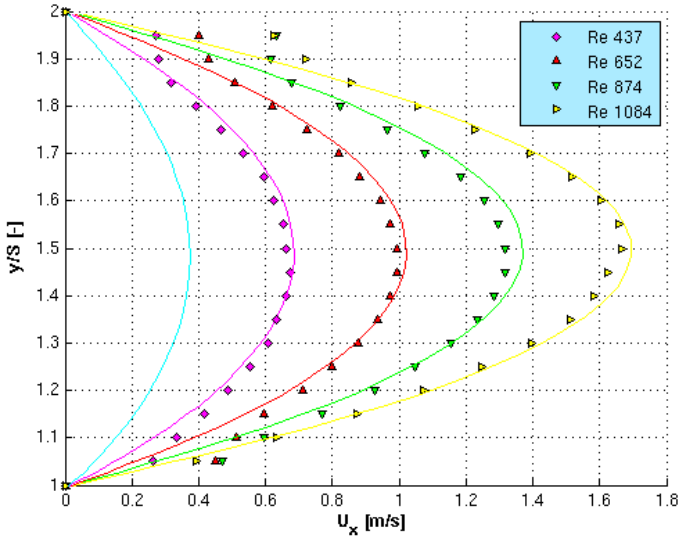

Figure A.1. Velocity profiles at the symmetry plane $z/b = 0$, at upstream distance $x/S = -1$, aspect ratio $AR = 5.3$. Symbols stay for experimental data, full lines for corresponding numerical simulation.

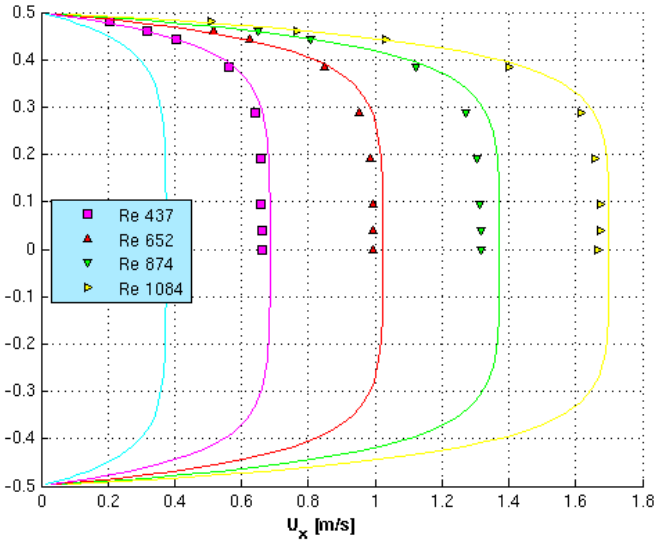

Figure A.2. Spanwise velocity profiles in the horizontal middleplane $y/S = 1.5$, at upstream distance $x/S = -1$, aspect ratio $AR = 5.3$. Symbols stay for experimental data, full lines for corresponding numerical simulation.

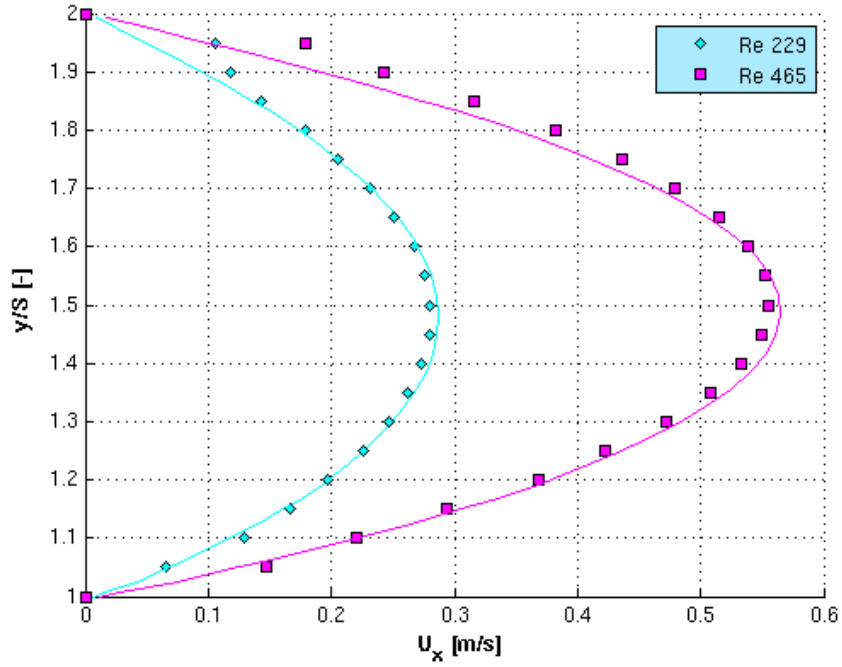

Figure A.3. Velocity profiles at the symmetry plane $z/b = 0$, at upstream distance $x/S = -1$, aspect ratio $AR = 33.2$. Symbols stay for experimental data, full lines for corresponding numerical simulation.

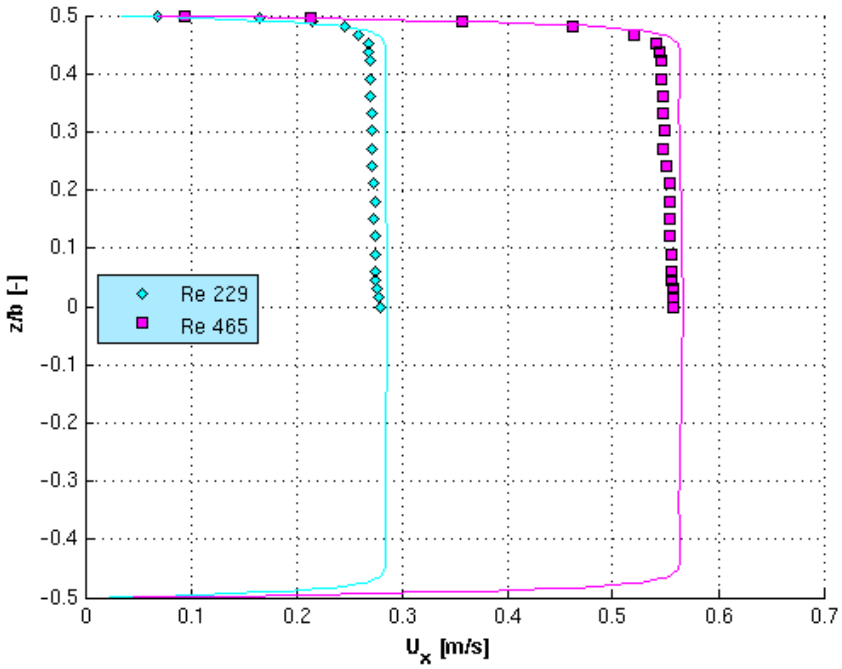

Figure A.4. Spanwise velocity profiles in the horizontal middleplane $y/S = 1.5$, at upstream distance $x/S = -1$, aspect ratio $AR = 33.2$. Symbols stay for experimental data, full lines for corresponding numerical simulation.

Appendix B. Visualisations of vortices

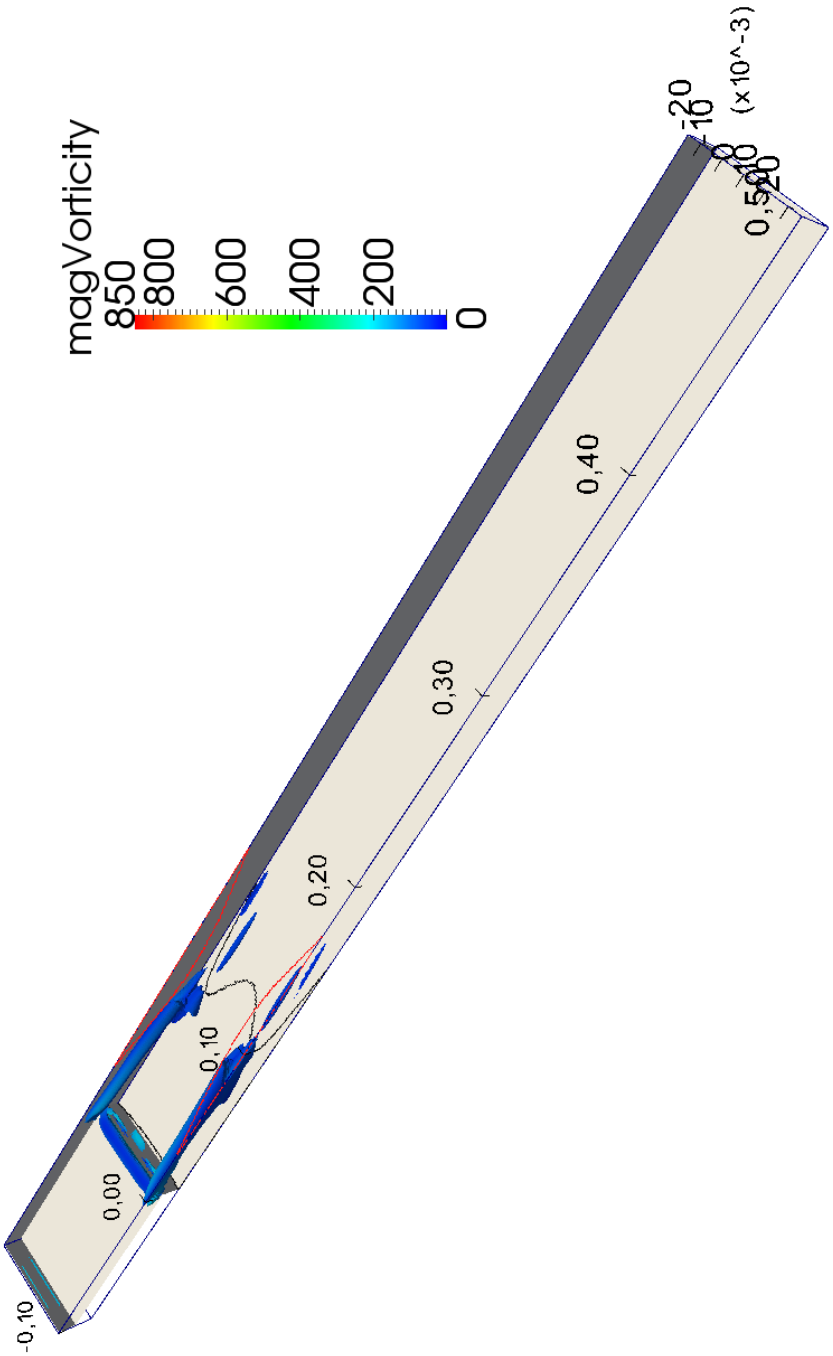

Figure B.1. Visualization of vortices - isosurfaces at $\lambda_2 = -50$. Colors by vorticity magnitude; aspect ratio $AR = 5.3$, $Re = 437$. Black line denotes reattachment line of the primary recirculation flow region; red line ilustrates secondary flow region projected on the upper wall.

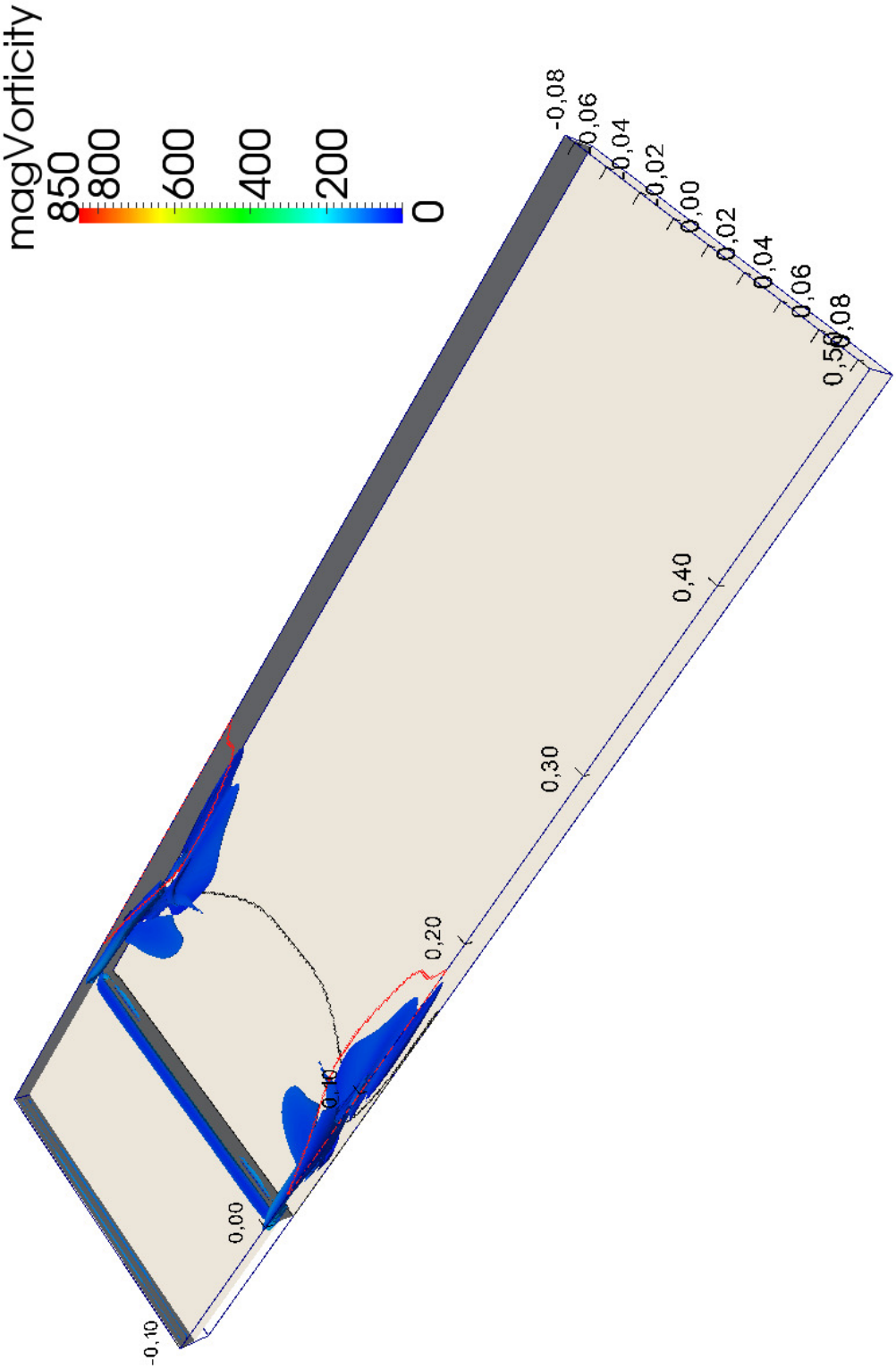

Figure B.2. Visualization of vortices - isosurfaces at $\lambda_2 = -50$. Colors by vorticity magnitude; aspect ratio $AR = 17.3$, $Re = 476$. Black line denotes reattachment line of the primary recirculation flow region; red line ilustrates secondary flow region projected on the upper wall.

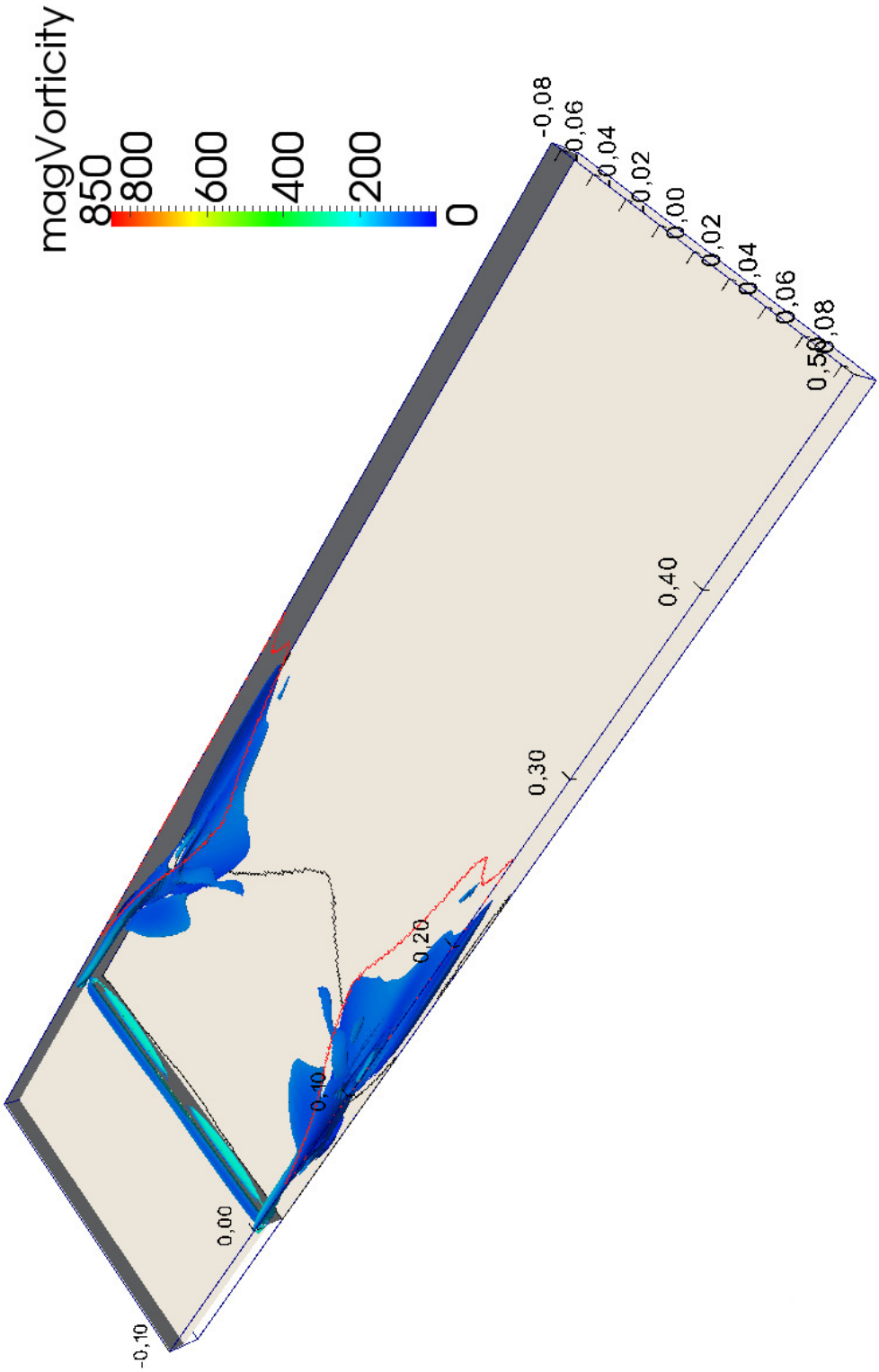

Figure B.3. Visualization of vortices - isosurfaces at $\lambda_2 = -100$. Colors by vorticity magnitude; aspect ratio $AR = 17.3$, $Re = 703$. Black line denotes reattachment line of the primary recirculation flow region; red line ilustrates secondary flow region projected on the upper wall.

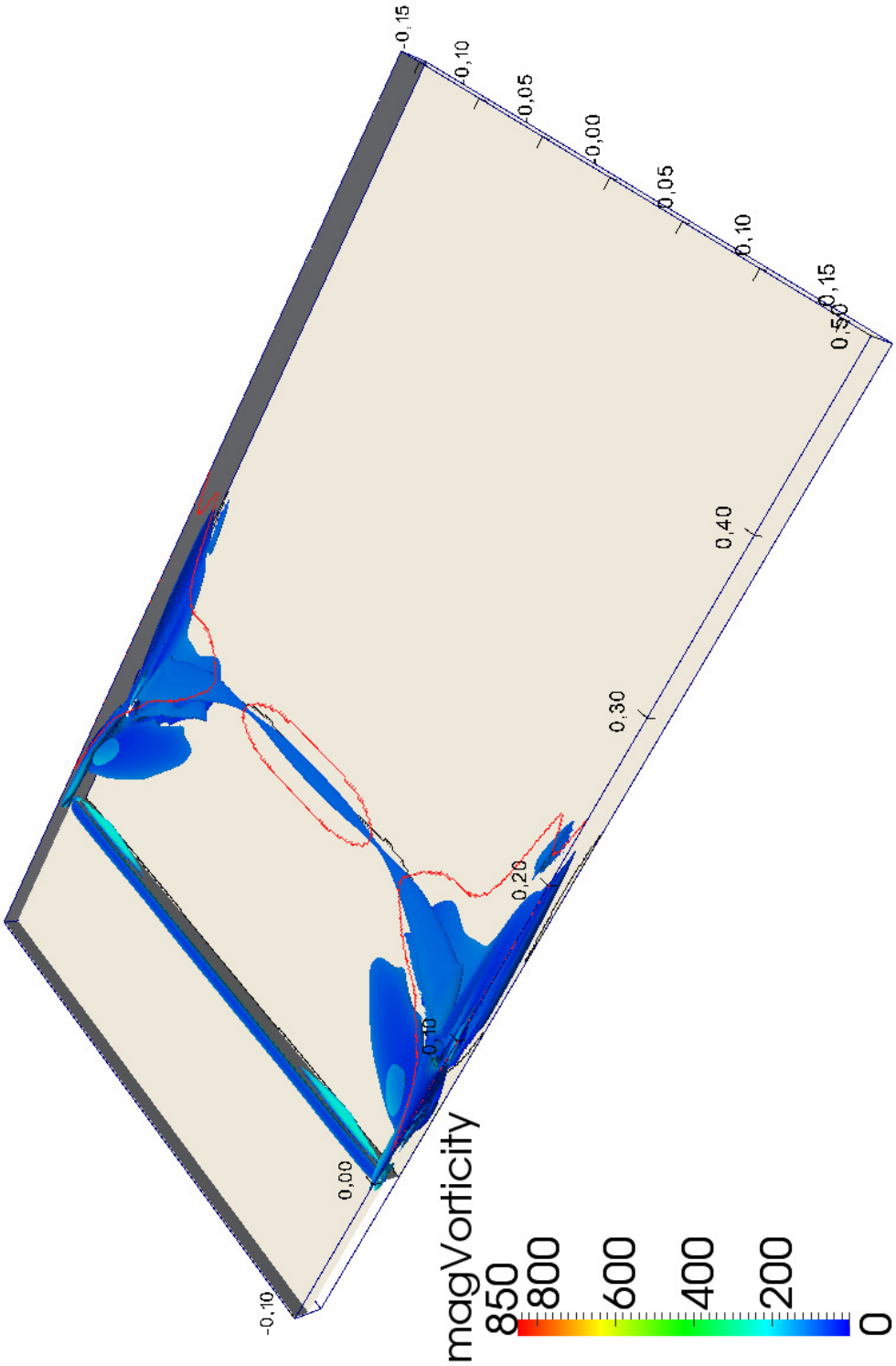

Figure B.4. Visualization of vortices - isosurfaces at $\lambda_2 = -75$. Colors by vorticity magnitude; aspect ratio $AR = 33.2$, $Re = 679$. Black line denotes reattachment line of the primary recirculation flow region; red line ilustrates secondary flow region projected on the upper wall.

References

[1] Adams E. W., Eaton J. K.: An LDA Study of the Backward-Facing Step Flow, Including the Effects of Velocity Bias. *Journal of Fluids Engineering* **110**, 275-282 (September 1988).

[2] Adrian R. J.: Dynamic ranges of velocity and spatial resolution of particle image velocimetry. *Measurement Science and Technology* **8**, 1393-1398 (1997).

[3] Albrecht H. E., Borys M., Damaschke N., Tropea C.: *Laser Doppler and Phase Doppler Measurement Techniques.* Springer, 2003.

[4] Albrecht D.: On PIV Measurements in Rectangular Duct. *Experimental Fluid Mechanics 2006*, Technical University Liberec, Liberec (2006).

[5] Armaly B. F., Durst F., Pereira J. C. F., Schönung B.: Experimental and theoretical investigation of backward-facing step flow. *Journal of Fluid Mechanics* **127**, 473-496 (1983).

[6] Armaly B. F., Li A., Nie J. H.: Three-dimensional forced convection flow adjacent to backward-facing Step. *Journal of Thermophysics and Heat Transfer* **16** (2), 222-227 (April-June 2002).

[7] Armaly B. F., Li A., Nie J. H.: Measurements in three-dimensional laminar separated flow. *International Journal of Heat and Mass Transfer* **46**, 3573-3582 (2003).

[8] Badran O. O., Bruun H. H.: The effect of inlet conditions on flow over backward facing step. *Journal of Wind Engineering and Industrial Aerodynamics* **74-76**, 495-509 (1998).

[9] Barkley D., Gomes M. G. M., Henderson R. D.: Three-dimensional instability in flow over a backward-facing step. *Journal of Fluid Mechanics* **473**, 167-190 (2002).

[10] Biswas G., Breuer M., Durst F.: Backward-facing step flows for various expansion ratios at low and moderate reynolds numbers. *Journal of Fluids Engineering* **126**, 362-374 (May 2004).

[11] Bonneau G.-P.; Ertl T.; Nielson G. M.: *Scientific Visualization: The Visual Extraction of Knowledge from Data*. Springer, 2006.

[12] Bradshaw P., Wong F. Y. F.: The reattachment and relaxation of a trubulent shear layer. *Journal of Fluid Mechanics* **52** (part 1), 113-135 (1972).

[13] Bruun H. H.: *Hot-Wire Anemometry - Principles and Signal Analysis*. Oxford University Press, 1995.

[14] Chapman D. R.: Computational Aerodynamics Development and Outlook. *AIAA Journal* **17**, 1293-1313 (1979).

[15] Chiang T. P., Sheu Tony W. H.: Vortical flow over a 3-D backward-facing step. *Numerical Heat Transfer* **31, Part A**, 167-192 (1997).

[16] Chiang T. P., Sheu Tony W. H.: A numerical revisit of backward-facing step flow problem. *Physics of Fluid* **11** (4), 862-874 (April 1999).

[17] Clauser F. H.: The turbulent boundary layer. *Advances in applied mechanics* **4**, 1-51 (1956).

[18] Dantec Dynamics: *LS-10e liquid seeding generator - users manual*.

[19] DeVilliers E.: *The Potential of Large Eddy Simulation for Modelling Wall Bounded Flows*. Ph.D. thesis, Imperial College of Science, Department of Mechanical Engineering, 2006.

[20] Eaton J. K.: *Turbulent flow reattachment: an experimental study of the flow and structure behind a backward-facing step.*. Doctoral Thesis, Stanford University, 1980.

[21] Elsinga G. E., Scarano F., Wieneke B., van Oudheusden B. W.: Tomographic particle image velocimetry. *Experiments in Fluids* **41**, 933-947 (December 2006).

[22] Furuichi N., Hachiga T., Kumada M.: An experimental investigation of a large-scale structure of a two-dimensional backward-facing step by using advanced multi-point LDV. *Experiments in Fluids* **36**, 274-281 (2004).

[23] Garnier E., Adams N., Sagaut P.: *Large Eddy Simulation for Compressible Flows*. Springer, 2009.

[24] Germano M., Piomelli U., Moin P., Cabot W. H.: A dynamic subgrid-scale eddy viscosity model. *Physics of Fluids A* **3** (7), 1760-1765 (1991).

[25] Germano M.: Turbulence: the filtering approach. *Journal of Fluid Mechanics* **238**, 325-336 (1992).

[26] Ghosal S., Lund T. S., Moin P., Aksevoll K.: A dynamic localization model for large-eddy simulation of turbulent flows. *Journal of Fluid Mechanics* **286**, 229-255 (1995).

[27] Hall S. D., Behnia M., Fletcher C. A. J., Morrison G. L.: Investigation of the secondary corner vortex in a benchmark turbulent backward-facing step using cross-correlation particle imaging velocimetry. *Experiments in Fluids* **35**, 139-151 (2003).

[28] Hanjalić K., Launder B. E.: Second order closure turbulence models, their achievements and limitations. *Journal of Fluid Mechanics* **52**, 438-609 (1976).

[29] Jeong J., Hussain F.: On the identification of a vortex. *Journal of Fluid Mechanics* **285**, 69-94 (1995).

[30] Isomoto K., Honami S.: The Effect of Inlet Turbulence Intensity on the Reattachment Process Over a Backward-Facing Step. *Journal of Fluids Engineering* **111**, 87-92 (March 1989).

[31] Iwai H., Nakabe K., Suzuki K.: Flow and heat transfer characteristics of backward-facing step laminar flow in a rectangular duct. *International Journal of Heat and Mass Transfer* **43**, 457-471 (2000).

[32] Jiang M., Machiraju R., Thompson D.: *Detection and visualisation of vortices.* Academic Press, 2004.

[33] Jonáš P.: O turbulenci. *Inženýrská mechanika* **5** (2), 89-106 (1998).

[34] Kaiktsis L., Karniadakis G. M., Orszag S. A.: Onset of three-dimensionality, equilibria, and early transition in flow over a backward-facing step. *Journal of Fluid Mechanics* **231**, 501-528 (1991).

[35] Kaiktsis L., Karniadakis G. M., Orszag S. A.: Unsteadiness and convective instabilities in two-dimensional flow over a backward-facing step. *Journal of Fluid Mechanics* **321**, 157-187 (1996).

[36] Keane R. D., Adrian R. J.: Optimization of particle image velocimetrs. Part I: Double pulsed systems. *Measurement Science and Technology* **1**, 1202-1215 (1990).

[37] Kitoh A., Suguwara K., Yoshikawa H., Ota T.: Expansion Ratio Effects on Three-Dimensional Separated Flow and Heat Transfer Around Backward-Facing Steps. *Journal of Heat Transfer* **129**, 1141-1155 (September 2007).

[38] Kolmogorov A. N.: The local structure of turbulence in incompressible viscous fluid for very large Reynolds numbers. *Proceeding Royal Society London A* **434**, 9-13 (1991).

[39] Kostas J., Soria J., Chong M. S.: Particle image velocimetry measurements of a backward-facing step flow. *Experiments in Fluids* **33**, 838-853 (2002).

[40] Launder B. E., Spalding D. B.: The numerical computations of turbulent flows. *Computer methods in applied mechanics and engineering* **3**, 269-289 (1974).

[41] Le H., Moin P., Kim J.: Direct numerical simulation of turbulent flow over a backward-facing step. *Journal of Fluid Mechanics* **330**, 349-374 (1997).

[42] Lee I., Sung H. J.: Characteristics of wall preassure fluctuations in separated and reattaching flows over a backward-facing step: Part I. Time-mean statistics and cross-spectral analyses. *Experiments in Fluids* **30**, 262-272 (2001).

[43] Lee I., Sung H. J.: Characteristics of wall preassure fluctuations in separated flows over a backward-facing step: Part II. Unsteady wavelet analysis. *Experiments in Fluids* **30**, 273-282 (2001).

[44] Leonard A.: Energy cascade in large-eddy simulations of turbulent flows. *Advances in Geophysics* **A 18**, 237-248 (1974).

[45] Lilly D. K.: A proposed modification of the Germano subgrid-scale closure method. *Physics of Fluids A* **4** (3), 633-635 (1992).

[46] Moffat H. K.: Viscous and resistive eddies near a sharp corner. *Journal of Fluid Mechanics* **18**, 1-18 (1964).

[47] Neumann J., Wengle H.: DNS and LES Passively Controlled Turbulent Backward-Facing Step Flow. *Flow, Turbulence and Combustion* **71**, 297-310 (2003).

[48] Nie J. H., Armaly B. F.: Three-dimensional convective flow adjacent to backward-facing step - effects of step . *International Journal of Heat and Mass Transfer* **45**, 2431-2438 (2002).

[49] Nie J. H., Armaly B. F.: Reattachment of Three-Dimensional Flow Adjacent to Backward-Facing Step. *Journal of Heat Transfer* **125**, 422-428 (June 2003).

[50] Nie J. H., Armaly B. F.: Reverse flow regions in three-dimensional backward-facing step flow. *International Journal of Heat and Mass Transfer* **47**, 4713-4720 (July 2004).

[51] Nikon: *AF-S Micro NIKKOR 60mm f*/2.8*D G ED*.

[52] Ötügen M. V.: Expansion ratio effects on the sepparated shear layer and reattachment downstream of a backward-facing step. *Experiments in Fluids* **10**, 273-280 (1991).

[53] Piirto M., Saarenrinne P., Eloranta H., Karvinen R.: Measuring turbulence energy with PIV in a backward-facing step flow. *Experiments in Fluids* **35** (3), 219-236 (February 2004).

[54] Piirto M., Ahlstedt H., Saarenrinne P., Karvinen R.: PIV measurements in a square backward facing step. *15th Australasian Fluid Mechanics Conference* (December 2004).

[55] Piomelli U., Liu J.: Large eddy simulation of rotating channel flows using localized dynamic model. *Physics of Fluids* **7** (4), 839-848 (1995).

[56] Plíva Z., Drábková J.: *Metodika zpracování diplomových, bakalářských a vědeckých prací na FM TUL.* Technická universita v Liberci, 2009.

[57] Prandtl L.: Uber ein neues Formelsystem fur die ausgebildete Turbulenz. *Technical report, Akademy of Sciences* (1945).

[58] Raffel M., Willert C., Wereley S., Kompenhans J.: *Particle Image Velocimetry - A Practical Guide.* Springer. Second, 2007.

[59] Reynolds O.: On the dynamical theory of incompressible viscous fluids and the determination of the criterion. *Philosophical Transactions of the Royal Society of London* **186**, 123-161 (1895).

[60] Sagaut P.: *Large Eddy Simulation for Incompressible Flows.* Springer, 2004.

[61] Sakuraba K., Fukuzava K. Sano M.: Control of Turbulent Channel Flow over a Backward-Facing Step by Suction or Injection. *Heat Transfer - Asian Research* **33** (8), 490-503 (2004).

[62] Smagorinsky J.: General circulation experiments with the primitive equations. *Month. Weather Rev.* **91**, 99-164 (1966).

[63] Tihon J., Legrand J., Legentilhomme P.: Near-wall investigation of backward-facing step flows. *Experiments in Fluids* **31**, 484-493 (2001).

[64] Tůma J.: *Zpracování signálů získaných z mechanických systémů metodou FFT*. Sdělovací technika, Praha, 1997.

[65] Tylli N., Kaiktsis L., Ineichen B.: Sidewall effects in flow over a backward-facing step: Experiments and numerical simulations. *Physics of Fluids* **14** (11), 3835-3845 (November 2002).

[66] Uruba V., Mazur O., Jonáš P.: Study on reversing flow in reattachment region. *Colloquium Fluid Dynamics 2005*, 171-174 (October 2005).

[67] Williams P. T., Baker A. J.: Numerical simulation of laminar flow over a 3d backward-facing step. *International Journal for Numerical Methods in Fluids* **24**, 1159-1183 (1997).

[68] Yoshizawa A., Horiuti K.: A Statistically-Derived Subgrid-Scale Kinetic Energy Model for the Large-Eddy Simulation of Turbulent Flows. *J. Phys. Soc. Japan* **54**, 2834-2839 (1985).